

Chapter 7

THERMODYNAMIC CALCULATIONS AND THEIR IMPLICATIONS

7.1 Introduction

Weld metal microstructures are in general, far from equilibrium. In duplex stainless steel weld metals, as a consequence of the thermal history and the high cooling rates involved, it is expected that a nonequilibrium mixture of austenite and δ -ferrite will always be obtained in the as-deposited region of the weld metal, although the microstructure in the reheated zones of the multirun welds is likely to be nearer to equilibrium, as is evident from the larger measured volume fractions of austenite to be found in the reheated zones of the weld. In this chapter, an attempt is made to test the agreement between theoretical calculations of the equilibrium volume fractions of austenite and δ -ferrite and some experimental determinations, and to examine the effect of alloying additions on the overall volume fraction of austenite. Clearly, calculations based on thermodynamic equilibrium are not justifiably compared with weld microstructures, but the aim was to predict general trends and to emphasize quantitatively, the role of alloy chemistry.

The microstructural constituents of duplex stainless steel weld metals are essentially δ and γ , and it is believed that the cooling period $\Delta t_{1200-800^\circ\text{C}}$ is the most crucial factor in determining the microstructure of the duplex stainless steel welds. The calculations presented below assume a two phase equilibrium mixture of δ and γ . It is realised that on occasions, sigma phase can also precipitate, but this is in general rare. The computer program used in the calculations is the "Thermocalc" system (Royal Institute of Technology, Sweden). This system is well established and is used here without any modification. The volume fractions of the phases are obtained by minimizing the Gibbs free energy of the multicomponent system and the model takes account of almost all the alloying elements involved as will become clear from the data tabulated later on in the text.

7.2 The Calculated and Measured Volume Fractions of Austenite

In this section, the calculated equilibrium volume fractions of austenite as a function of temperature (Table 7.1), are compared against corresponding metallographic

observations. The chemical compositions of the alloys investigated are shown in Table 7.2.

Table 7.1: The calculated equilibrium volume fractions of austenite as a function of temperature for most of the welded and wrought alloys investigated in this project. The delta ferrite volume fraction can be obtained by the difference from unity.

Alloy	Austenite volume fraction						
	873	973	1073	1173	1273	1373	1473 K
SH	0.25	0.53	0.47	0.4	0.29	0.15	0.01
SHP	0.15	0.34	0.4	0.36	0.25	0.08	0.00
WR2	0.76	0.85	0.91	0.88	0.82	0.72	0.72
R2P	0.45	0.73	0.71	0.66	0.58	0.45	0.26
R2PP	0.58	0.79	0.83	0.83	0.79	0.70	0.55
WR4	0.69	0.78	0.86	0.83	0.77	0.67	0.53
R4P	0.40	0.72	0.69	0.64	0.55	0.42	0.22
SP1	0.47	0.63	0.73	0.69	0.60	0.46	0.46
M22	0.77	0.86	0.91	0.89	0.83	0.73	0.58
BW	0.65	0.74	0.77	0.70	0.64	0.55	0.42
MELT3	0.06	0.28	0.41	0.40	0.29	0.09	0.00
MELT4	0.45	0.98	1.00	1.00	1.00	1.00	1.00
MELT5	0.16	0.53	0.80	0.84	0.78	0.62	0.35
IC373	0.46	0.66	0.55	0.48	0.37	0.24	0.06
IC378	0.45	0.71	0.78	0.76	0.69	0.55	0.36
IC381	0.51	0.74	0.78	0.75	0.67	0.54	0.40

Wrought alloy SH

Samples of this alloy, were aged using a tube furnace, beginning with the as swaged condition for eight days, at 900, 1000, and 1160 °C, while sealed in a quartz capsule under a partial pressure of argon. After completion of the ageing treatment, they were quenched in iced brine. The austenite volume fraction measurements were carried out on metallographically prepared specimens as described in Chapter 4, using an image analysis method. The calculated and measured volume fractions of austenite, versus

Table 7.2: Chemical composition (wt.%) of the wrought and welded duplex stainless steel alloys investigated. The nitrogen and oxygen concentrations are stated in parts per million by weight.

Material	C	Si	Mn	P	S	Cr	Ni	Mo	V	Nb	Ti	Al	Cu	N	O
SH	0.03	0.46	0.83	0.02	0.01	25.5	4.80	1.40	0.001	-	0.001	0.027	0.09	630	-
SHP	0.01	<0.01	<0.01	0.002	0.006	25.63	4.64	2.31	-	-	-	-	-	160	1700
W111	0.074	1.63	0.92	0.014	0.007	26.0	5.26	1.62	0.085	0.034	0.012	0.016	0.06	890	1120
WR2	0.02	0.43	1.52	0.013	0.003	22.76	7.8	2.87	0.03	0.003	0.003	0.023	0.06	1480	483
R2P	<0.02	0.35	1.32	-	-	23.4	7.5	3.5	-	-	-	-	-	-	-
R2PP	0.006	<0.01	<0.01	0.002	0.006	23.65	9.11	2.83	-	-	-	-	-	145	1600
WR4	0.02	0.48	1.11	0.024	0.014	23.10	8.79	2.98	0.09	0.008	0.003	0.027	0.01	786	1160
R4P	<0.02	0.47	1.03	-	-	22.8	7.1	3.0	-	-	-	-	-	-	-
SP1	0.023	0.44	1.31	0.029	0.009	22.2	5.4	2.69	0.04	<0.01	<.01	-	0.24	1020	140
SP2	0.021	0.43	1.30	0.029	0.009	22.0	5.4	2.69	0.04	<0.01	<.01	-	0.24	1040	140
BW	0.026	1.01	0.82	0.018	0.018	22.69	8.75	3.14	0.075	0.02	0.01	0.01	0.07	876	881
M22	0.021	0.49	1.64	0.019	-	22.50	7.9	2.92	0.05	<0.01	<0.01	-	0.06	1480	100
IC373	0.015	0.50	0.67	0.022	0.008	25.9	5.1	3.68	0.05	0.03	<0.01	-	1.83	1420	30
IC378	0.026	0.39	1.38	0.026	0.005	21.8	5.5	3.03	0.07	<0.01	<0.01	-	0.18	1400	60
IC381	0.025	0.48	1.92	0.026	0.006	22.1	5.8	3.17	0.13	<0.01	<0.01	-	0.07	1420	70
MELT 3	0.005	<0.01	<0.01	0.002	0.006	23.15	4.08	1.16	-	-	-	-	-	40	1800
MELT 4	0.006	<0.01	<0.01	0.002	0.006	18.34	7.7	0.01	-	-	-	-	-	52	618
MELT 5	0.01	<0.01	<0.01	0.002	0.006	18.32	4.6	2.38	-	-	-	-	-	70	953

temperature data are shown in Fig 7.1. The graph shows good agreement between the measured and calculated values of the volume fractions for the investigated ageing temperatures indicating that the ageing time used is adequate for the samples to approach equilibrium, although there are signs of discrepancies at the lower temperatures. The microstructures of the aged SH specimens are shown in (Fig. 7.2). At 1160°C the equilibrium microstructure consists of equiaxed δ -ferrite and austenite grains. At 900°C however, a three phase equilibrium microstructure consisting of δ -ferrite, austenite and σ phase was observed. The austenite grain structure is equiaxed, believed to have developed by recrystallisation and grain growth. The measured volume fraction of sigma phase at 900°C was found to be 0.2. The intervention of σ phase seems to be re-

sponsible for causing a decrease in the measured volume fraction of austenite at 900°C ageing temperature. This is believed to be the result of deviation in the sigma phase composition from the expected (calculated) δ -ferrite composition Table 7.3. At 800°C ageing temperature, the differences between the measured sigma phase composition and that expected for δ -ferrite is narrowing which may explain the better correlation in the measured and calculated austenite volume fraction at this temperature. Evidence for the formation of the sigma phase is provided by the recorded diffraction pattern obtained on a Phillips diffractometer by bombarding the specimen with CuK_α radiation (Fig. 7.3).

Table 7.3: The experimentally measured compositions of Sigma, δ -ferrite and austenite phases in wrought alloy SH (wt%) after ageing treatment determined by EDX analysis unit attached to “S4” scanning electron microscope and the respective calculated equilibrium compositions corrected for the interstitial elements carbon and nitrogen since the experimental data ignore the presence of any carbon and nitrogen in the analysed phases.

$T_{\text{ageing}} \text{ } ^\circ\text{C}$	Phase	Fe	Cr	Ni	Mo	Mn	Si
800	σ	58.6 ± 0.5	34.1 ± 0.4	3.2 ± 0.2	2.7 ± 0.2	0.6 ± 0.2	0.7 ± 0.05
800	$\gamma_{\text{exp.}}$	67.5 ± 0.5	22.2 ± 0.4	7.2 ± 0.2	1.3 ± 0.2	1.3 ± 0.2	0.4 ± 0.05
900	σ	57.8 ± 0.5	34.8 ± 0.4	3.1 ± 0.2	3.0 ± 0.2	0.6 ± 0.2	0.7 ± 0.05
800	$\delta_{\text{calc.}}$	63.93	30.47	2.75	1.543	0.8	0.43
900	$\delta_{\text{calc.}}$	65.18	28.7	3.22	1.49	0.82	0.49
900	$\gamma_{\text{exp.}}$	67.9 ± 0.5	20.9 ± 0.4	7.8 ± 0.2	1.13 ± 0.2	1.13 ± 0.2	0.3 ± 0.05
900	$\delta_{\text{exp.}}$	64.8 ± 0.5	28.9 ± 0.4	3.3 ± 0.2	1.7 ± 0.2	0.5 ± 0.2	0.5 ± 0.05

Wrought alloy SHP

Specimens were solution treated before prolonged ageing treatments for 48 hours at 1150°C. Samples were then aged at 800, 900, and 1100°C for 8 days, followed by

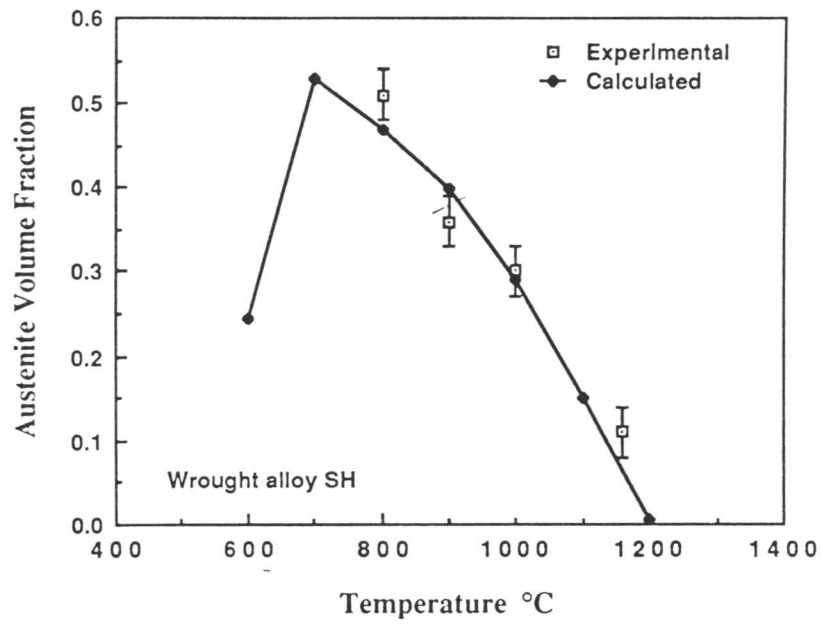


Fig. 7.1: Calculated and experimentally measured volume fractions of austenite as a function of ageing temperature for wrought alloy SH.

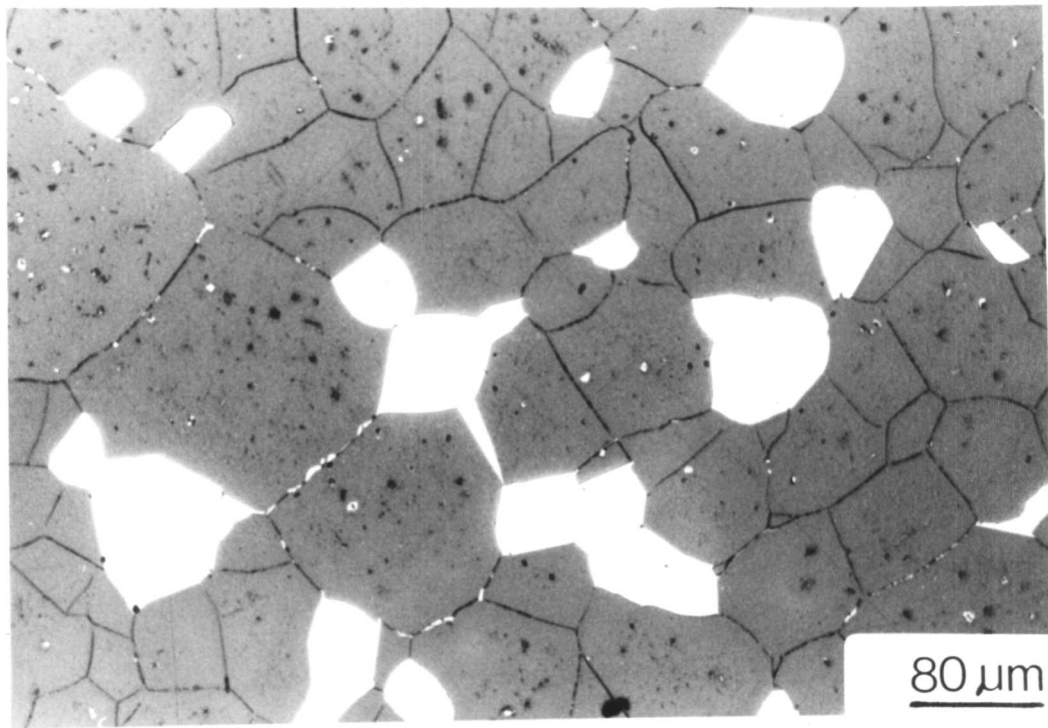


Fig. 7.2.a: Microstructure of wrought alloy SH aged for eight days at 1160°C. The white phase is austenite and the black dots in the interior of the δ -ferrite grains are very fine austenite particles formed during quenching after the ageing treatment. The measured hardness of the specimen is (VHN 259)

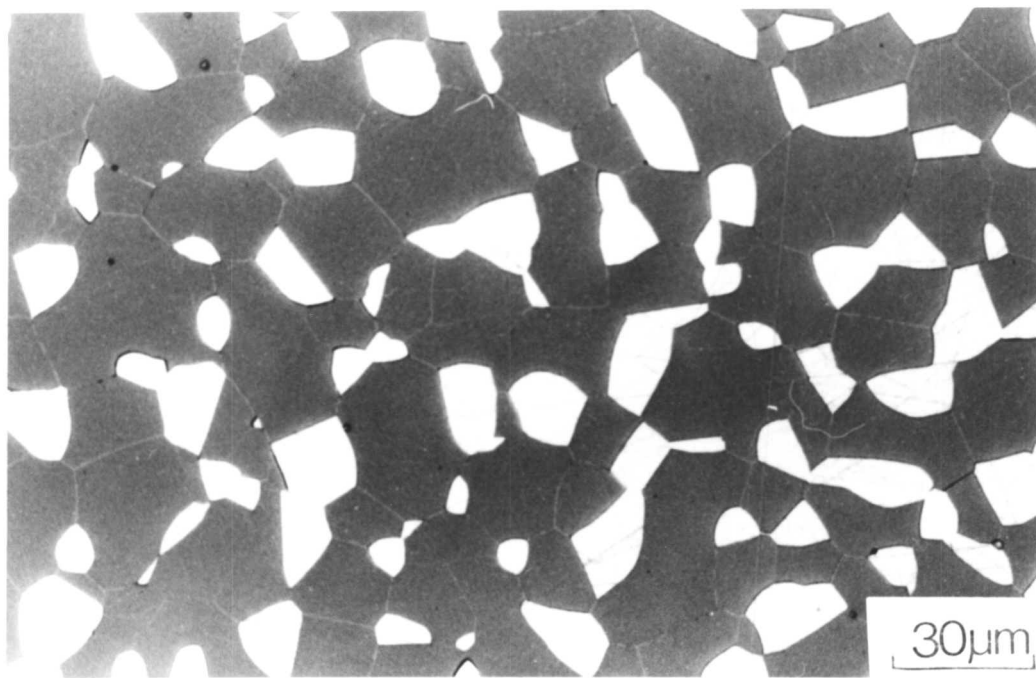


Fig. 7.2.b: Microstructure of wrought alloy SH aged for eight days at 1000°C. The white phase is austenite. The measured hardness of the specimens is (VHN 214).

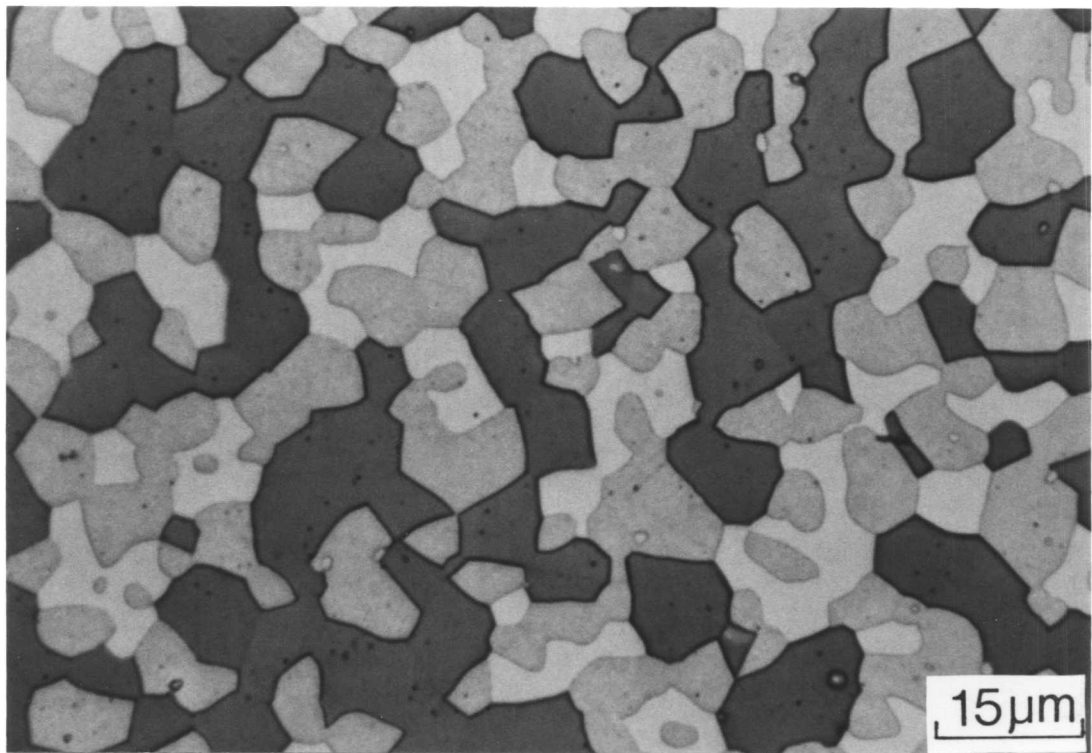


Fig. 7.2.c: Colour micrograph showing the microstructure of wrought alloy SH aged at 900°C for eight days. The specimen was etched with Beraha's colour etchant which reacts heavily with δ -ferrite (brown), slightly with the austenite (dirty white), while it leaves the sigma phase (white) unattacked. The measured hardness of the specimen was (HVN 281).

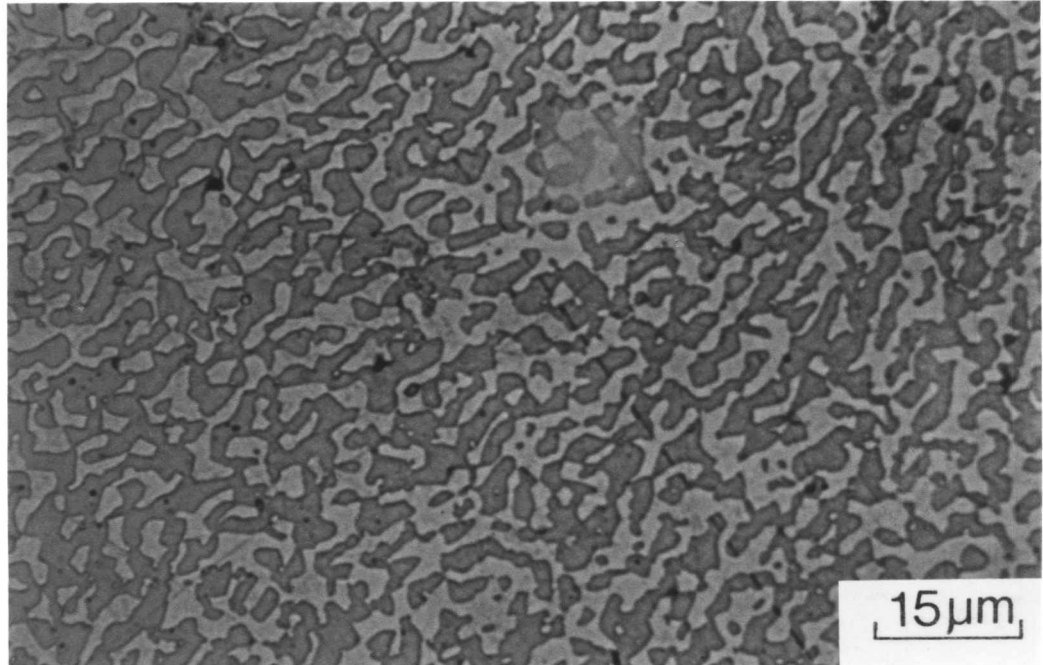


Fig. 7.2.d: Colour micrograph of wrought alloy SH aged at 800°C for eight days showing a duplex microstructure of $\gamma + \sigma$. The scratch appearing in the micrograph is discontinuous at the sigma phase which demonstrate its very high hardness. The measured hardness number of the specimen is (VHN 536).

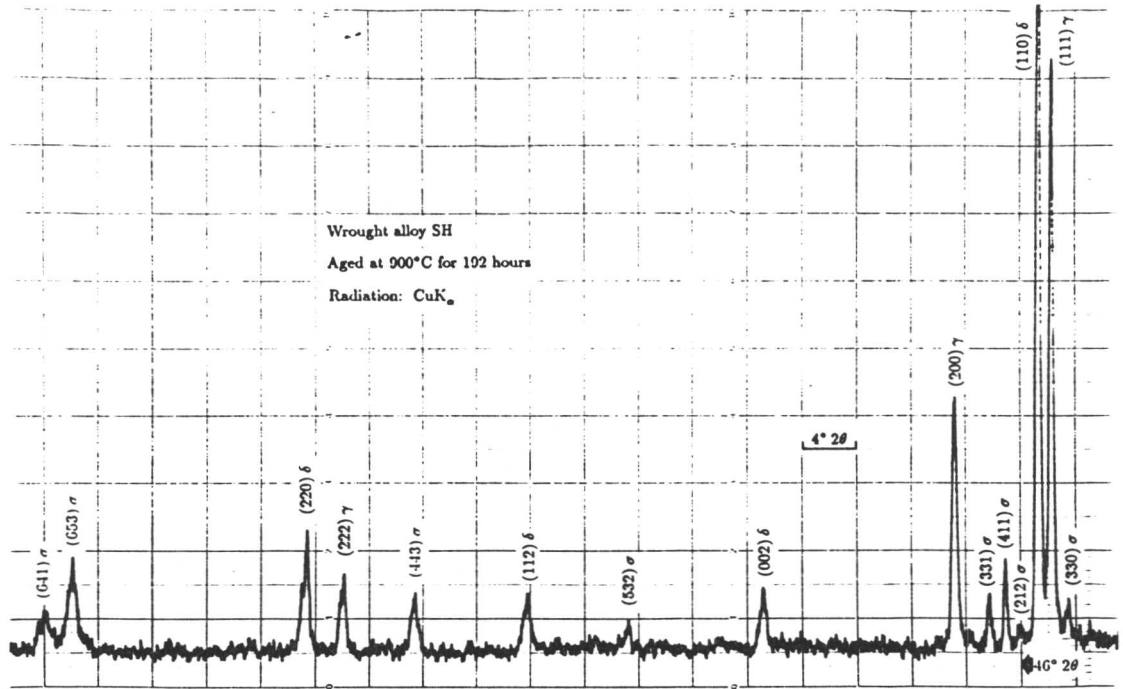


Fig. 7.3.a: X-ray diffraction pattern of specimen SH aged at 900°C for eight days obtained by bombarding the specimen with Cu K_α radiation in a Phillips diffractometer.

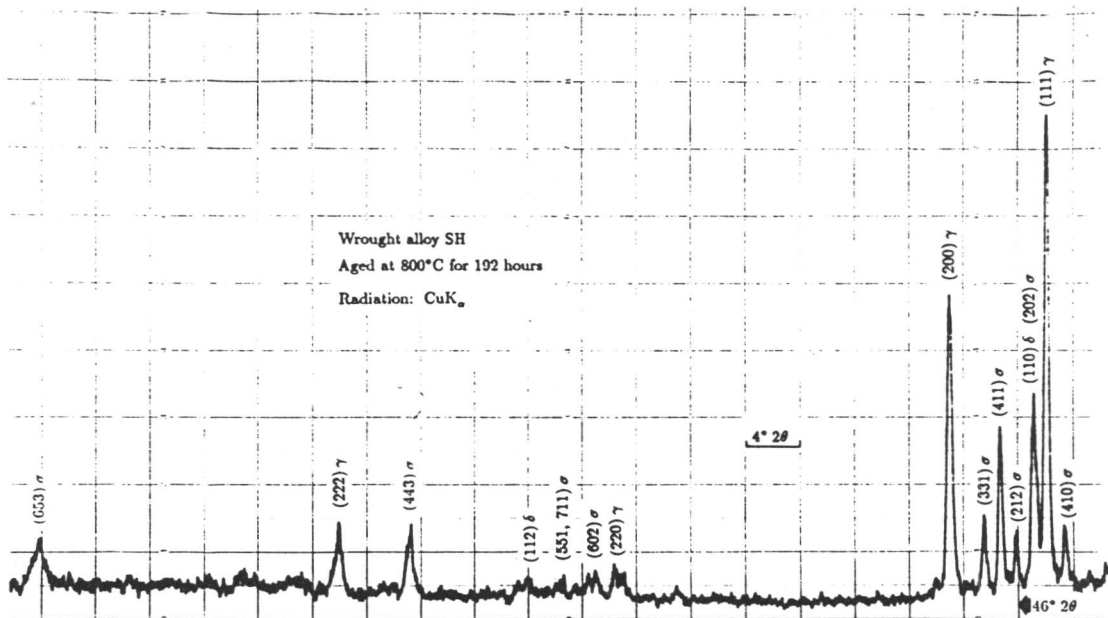


Fig. 7.3.b: X-ray diffraction pattern of specimen SH aged at 800°C for eight days obtained by bombarding the specimen with Cu K_α radiation in a Phillips diffractometer.

quenching in iced brine. The volume fraction of austenite was measured as described for alloy SH. The results are illustrated in Fig. 7.4.

Since specimens were ferritised prior to the ageing treatment, their δ grain size, as revealed in Fig. 7.5, was much coarser than that of the SH specimens, owing to the fact that all of the austenite is believed to have dissolved at the ferritising temperature. As a consequence, the morphologies of the austenite grains that formed subsequently were influenced by the coarse δ grain structure. On ageing at 1100°C the austenite was observed to be in the form of thick, allotriomorphic layers at the original δ/δ grain boundaries Fig. 7.5.c. The calculated and measured chemical compositions of both phases after ageing at 1100°C are shown in Table 7.4. The relatively good agreement between the calculated and experimentally measured compositions of both phases explains the good correlation in the measured and calculated volume fractions of austenite at 1100°C ageing temperature Fig. 7.4.

Table 7.4: Chemical composition of δ and γ in samples of wrought alloy SHP aged at 1100°C in (wt.%). The experimental values were obtained by EDX analysis using an "S4" SEM. The expected calculated equilibrium compositions were corrected for the interstitials C & N since the experimental data ignore their presence.

phase	Fe	Cr	Ni	Mo	Mn	Si
δ exp.	64.5 ± 0.5	27.4 ± 0.4	5.0 ± 0.2	2.9 ± 0.2	0.1 ± 0.2	0.2 ± 0.05
δ calc.	67.19	26.05	4.43	2.34	0.01	0.01
γ exp.	66.9 ± 0.5	22.0 ± 0.4	8.0 ± 0.2	2.9 ± 0.2	0.1 ± 0.2	0.0
γ calc.	69.99	19.98	7.86	2.19	0.01	0.007

In samples aged at 1000°C the austenite was also observed as allotriomorphic layers at the δ/δ boundaries but acicular austenite particles were also found within the interior of the δ grains, some precipitation^{of σ was} also observed within the allotriomorphic layer of austenite. The microstructure of samples aged at 800°C was similar to the 1000°C aged specimens, but with the major difference that substantial sigma phase formation had occurred after the growth of austenite. The morphology of the sigma phase indicates

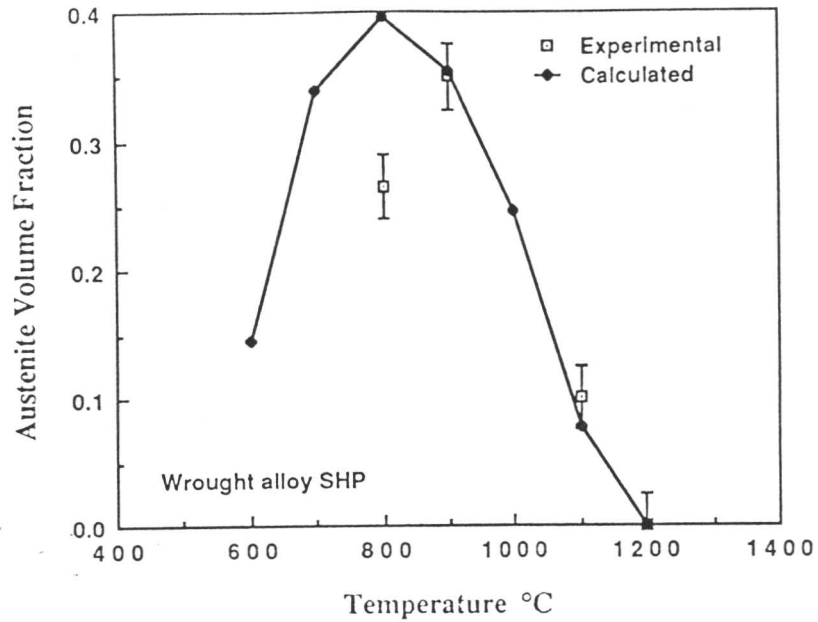


Fig. 7.4: Calculated and experimentally measured volume fractions of austenite as a function of ageing temperature in wrought alloy SHP.

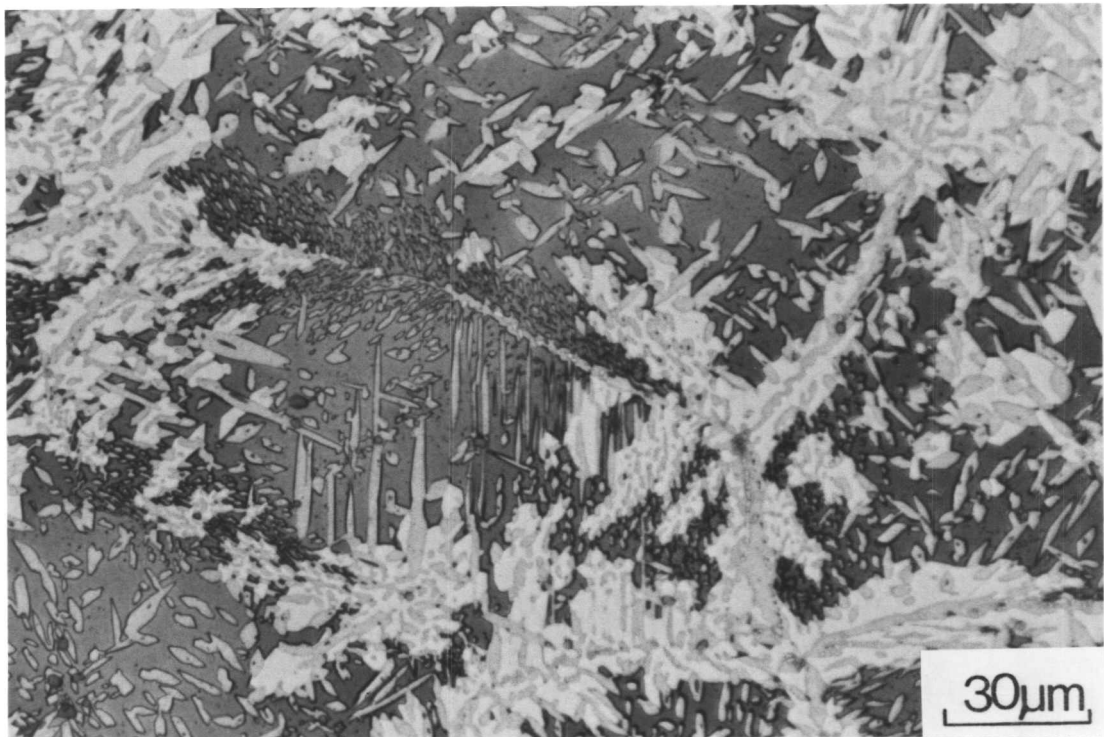


Fig. 7.5.a: Colour micrograph showing the microstructure of wrought alloy SHP aged for eight days at 800°C. The specimen was etched by Beraha's colour etchant. The dark etched phase (brown) is δ -ferrite, the slightly etched phase (cream) is austenite and sigma phase appears white as its not affected by the etchant. The measured hardness of the specimens (VHN 223).

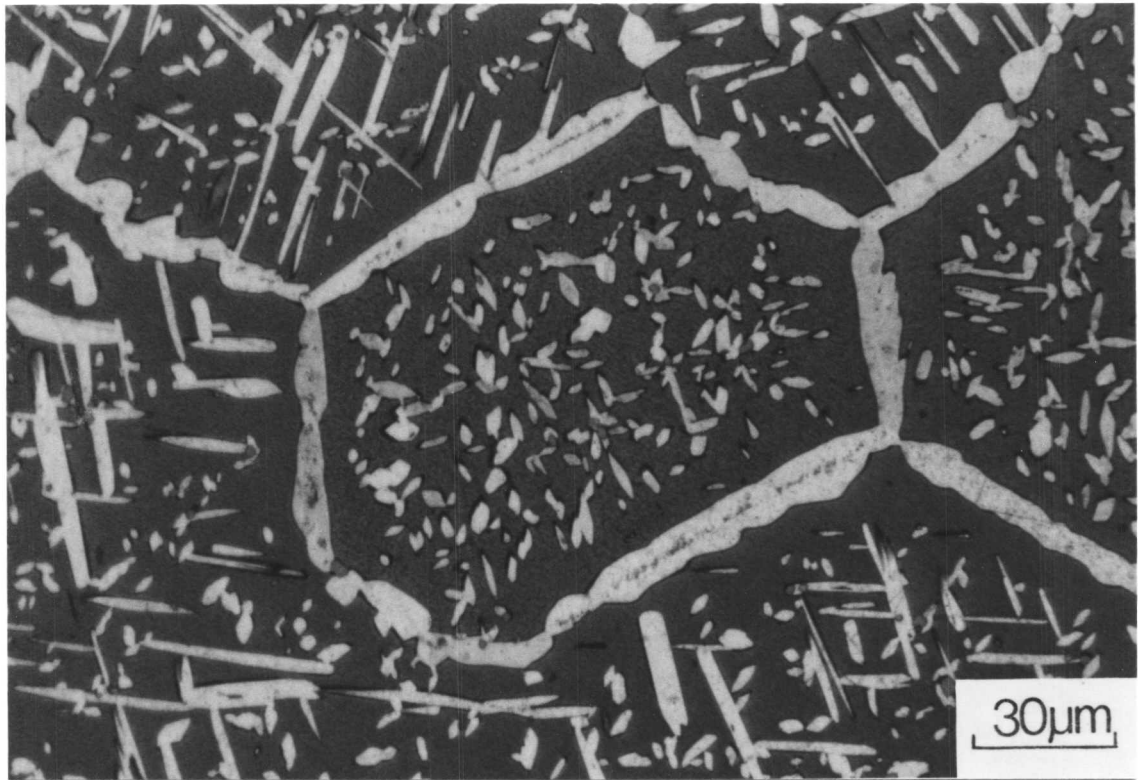


Fig. 7.5.b: Microstructure of wrought alloy SHP aged for eight days at 900°C. The light etching phase is austenite and the blue phase is δ -ferrite. The precipitates appearing in the middle of the austenite allotriomorphs are possibly χ or σ phase. The measured hardness of the specimen is (VHN 210).

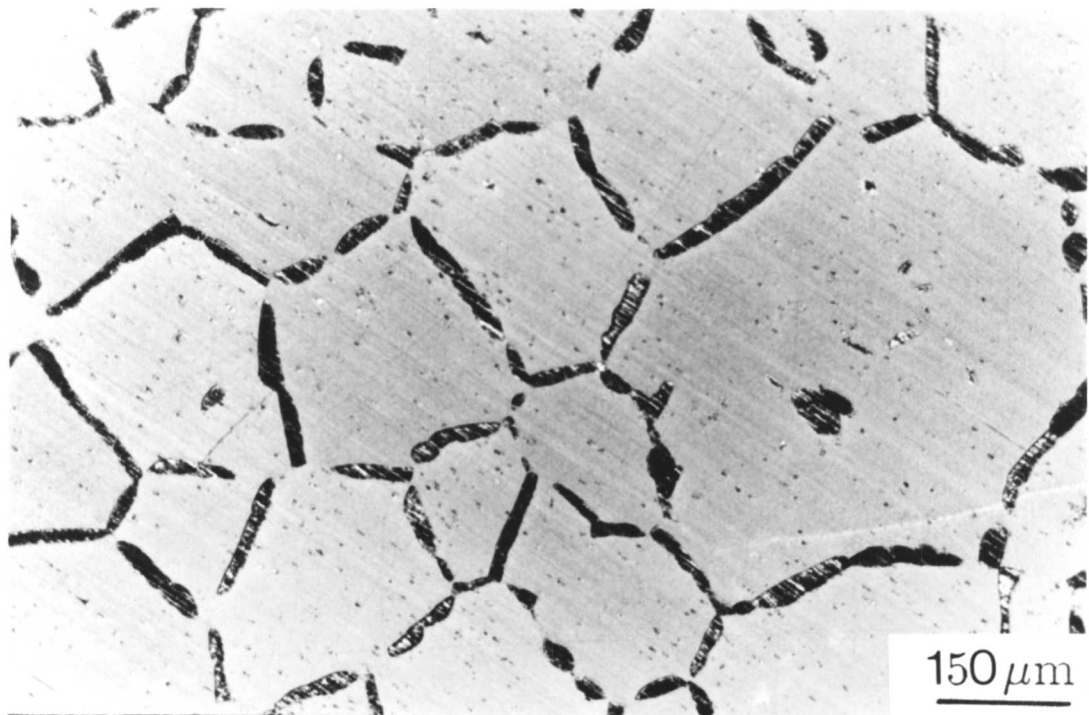


Fig. 7.5.c: The microstructure of wrought alloy SHP after ageing at 1100°C for eight days. The dark phase is allotriomorphic austenite and the light phase is δ -ferrite. The measured hardness of the specimen is (VHN 223).

that it nucleates at the δ/γ interfaces; this is expected, partly because those regions will be enriched in elements like chromium which are rejected into the δ -ferrite by the growing austenite. Furthermore, much of the σ phase seems to have nucleated at the allotropic austenite/ δ -ferrite boundaries, rather than the acicular austenite/ δ -ferrite boundaries (Fig. 7.5). This could be because the degree of partitioning associated with the allotropic austenite is larger.

Welded alloy WR4

Samples of WR4 were aged from the as-received, welded condition at 800, 900, and 1120°C for 8 days as for alloy SH. The volume fraction of austenite versus temperature relationship for the calculated and measured values are shown in Fig. 7.6. The graph again shows good agreement between the calculated and measured volume fractions of austenite as a function of temperature. The microstructures of the aged specimens are shown in Fig 7.7. At 1120°C ageing temperature, the austenite particles within the δ grains have grown with the ageing time and coalesce towards equiaxed grain structure. The allotropic layers thickened, but the original columnar δ grains feature were retained. This is believed to be a consequence of the presence of the austenite along the δ/δ boundaries which has the effect of pinning down the movement of the δ boundaries during ageing. At both 800 and 900°C, a duplex microstructure of austenite and sigma phase was obtained. Although thickening of the acicular and Widmanstätten austenite plates was observed the original columnar welding features were still recognisable due to the effect of the thickened allotropic layers of austenite at the grain boundary.

Evidence for the formation of a duplex σ and γ is provided by the recorded diffraction pattern obtained on a Phillips diffractometer by bombarding the specimen of welded alloy WR4, aged at 900°C for 192 hours, with Cu K_α radiation, as no reflections of δ -ferrite were observed (Fig. 7.8). A comparison between the measured compositions of sigma, using EDX analysis on a scanning electron microscope, and the expected calculated equilibrium composition of δ -ferrite corrected for the interstitials carbon and nitrogen, since the EDX analysis ignores the presence of any interstitials, shows good agreement (Fig. 7.25), which explains the good correlation between the measured volume fractions of austenite and the equilibrium calculated ones as a function of temperature, although the calculations were based on a two phase equilibrium. It seems

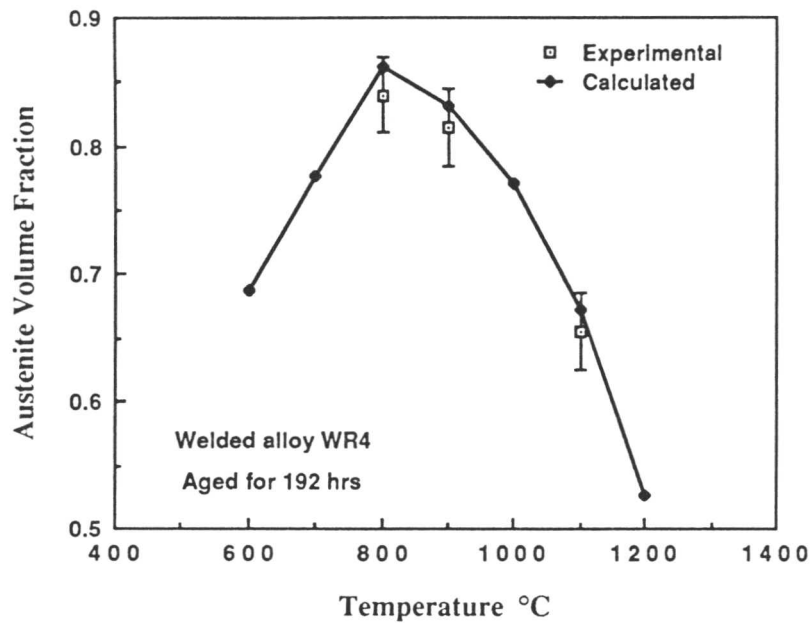


Fig. 7.6: Calculated and experimentally measured volume fractions of austenite as a function of ageing temperature.

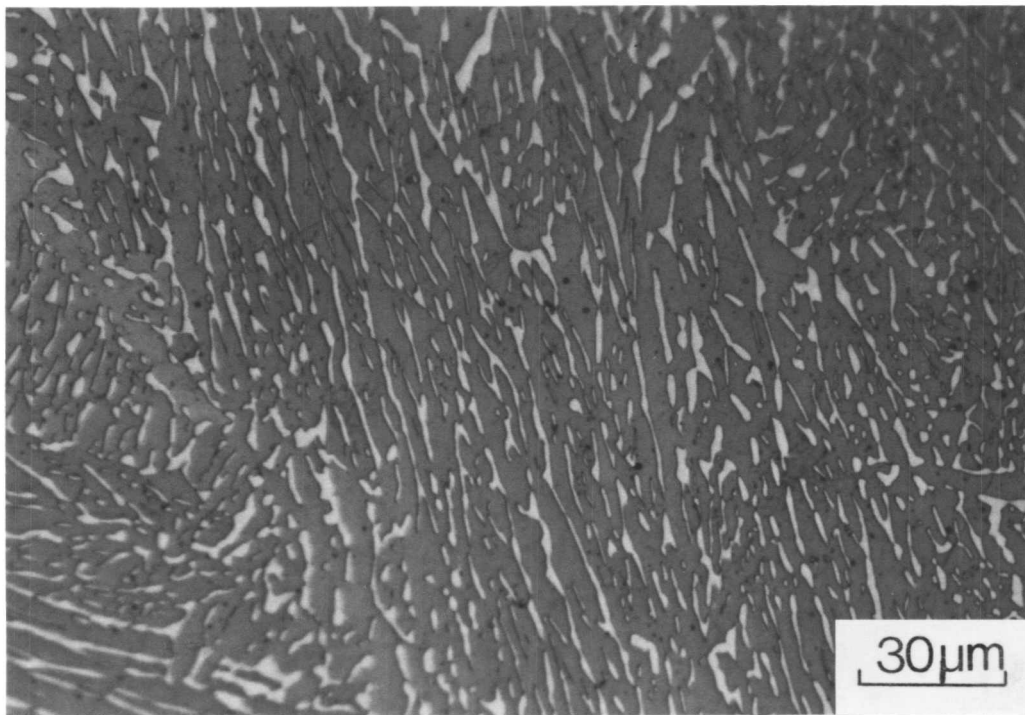


Fig. 7.7.a: Colour micrograph showing the microstructure of welded alloy WR4 aged for eight days at 900°C. The specimen was etched by Beraha's colour etchant. The dark etched phase (brown) is austenite and the unetched phase (white) is sigma phase. The measured hardness of the specimen is (VHN 302).

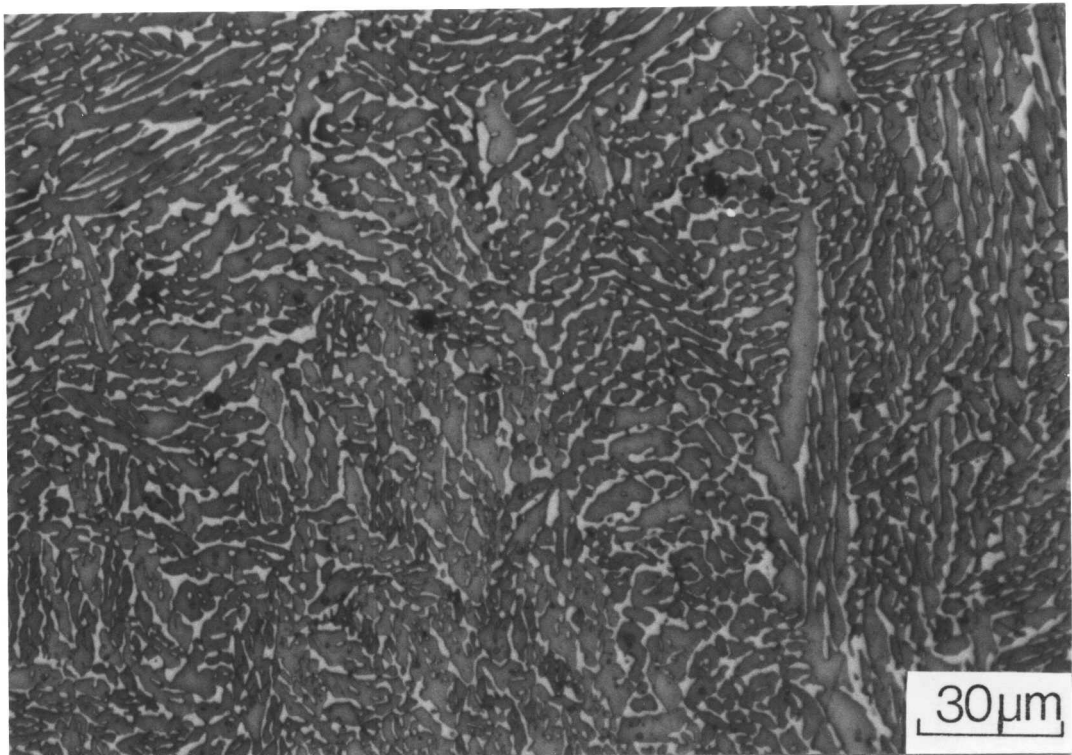


Fig. 7.7.b: Microstructure of welded alloy WR4 aged for eight days at 800°C. The dark etching phase (brown) is austenite and the unetched phase is sigma. The measured hardness of the specimen is (VHN 384).



Fig. 7.7.c: Microstructure of welded alloy WR4 after ageing at 1120°C for eight days. The dark etching phase is austenite and the measured hardness of the specimen is (VHN 223).

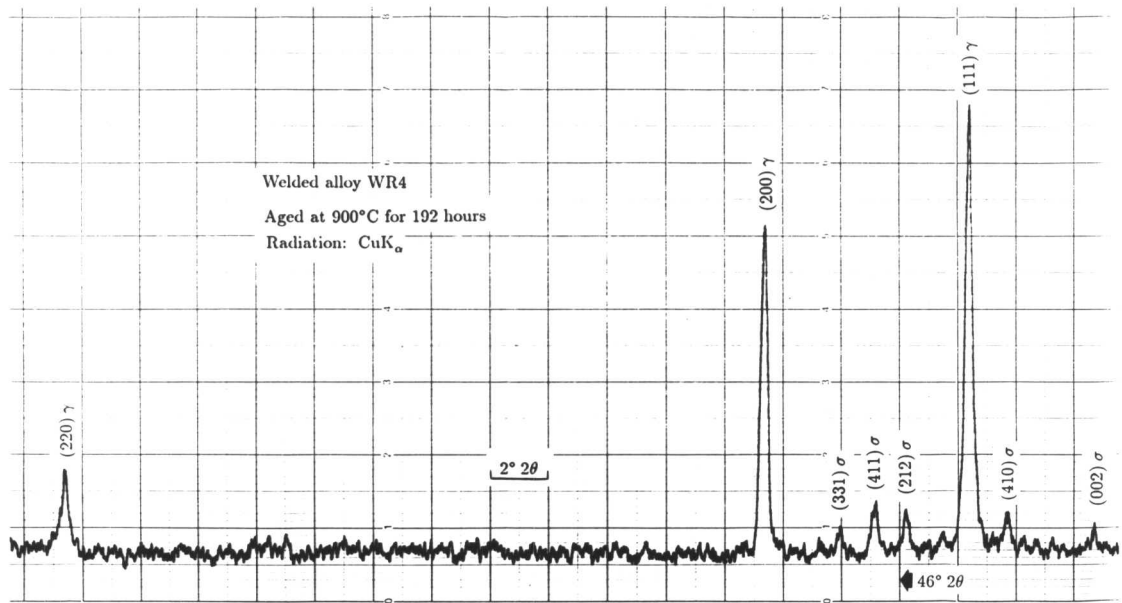


Fig. 7.8: X-ray diffraction pattern of specimen WR4 aged at 900°C for 192 hours obtained by bombarding the specimen with Cu k_α radiation in a Phillips diffractometer.

that the higher volume fractions of austenite and the larger area of δ/γ boundaries available in welded alloy WR4 led to the accelerated formation of a duplex ($\sigma + \gamma$) duplex microstructure.

Wrought alloys IC373, IC378 and IC381

IC373, IC378, and IC381 wrought alloys were aged from the as-rolled condition for 48 hours at 650, 790, 980, 1120, and 1200°C respectively. The calculated and measured austenite volume fraction versus temperature curves are shown in Fig 7.9. Fairly good agreement between the calculated and measured volume fraction of austenite was observed for IC378 and IC381 for the whole of the temperature range investigated. Alloy IC373 shows good agreement for ageing temperatures between 980 and 1200°C. For lower temperatures, the measured volume fractions of austenite were found to be much less than those calculated. This may be attributed to the precipitation of sigma phase. The X-ray diffraction pattern obtained by exposing IC373 specimen aged at 790°C to CuK_α proves the formation of sigma phase; In fact, no reflections of δ were observed Fig. 7.10. Disagreement between the measured and calculated austenite volume may also be attributed to insufficient time at 650°C to attain equilibrium, and could also be due to the difficulty in measuring the very fine austenite formed at this temperature accurately by optical means.

The microstructures of the aged IC373, IC378, and IC381 alloys are shown in Figs. 7.11 to 7.14. The specimens were all observed to retain the common elongated grains feature of the as received rolled microstructure, with this tendency increasing for the lower ageing temperatures. For samples aged at 1200°C, the microstructure of both IC378 and IC381 was observed to consist of elongated austenite grains in a δ -ferrite matrix, while that of IC373 was found to be completely ferritic Fig 7.11. This illustrates the effect of higher chromium content in IC373, in reducing the ferritisation temperature.

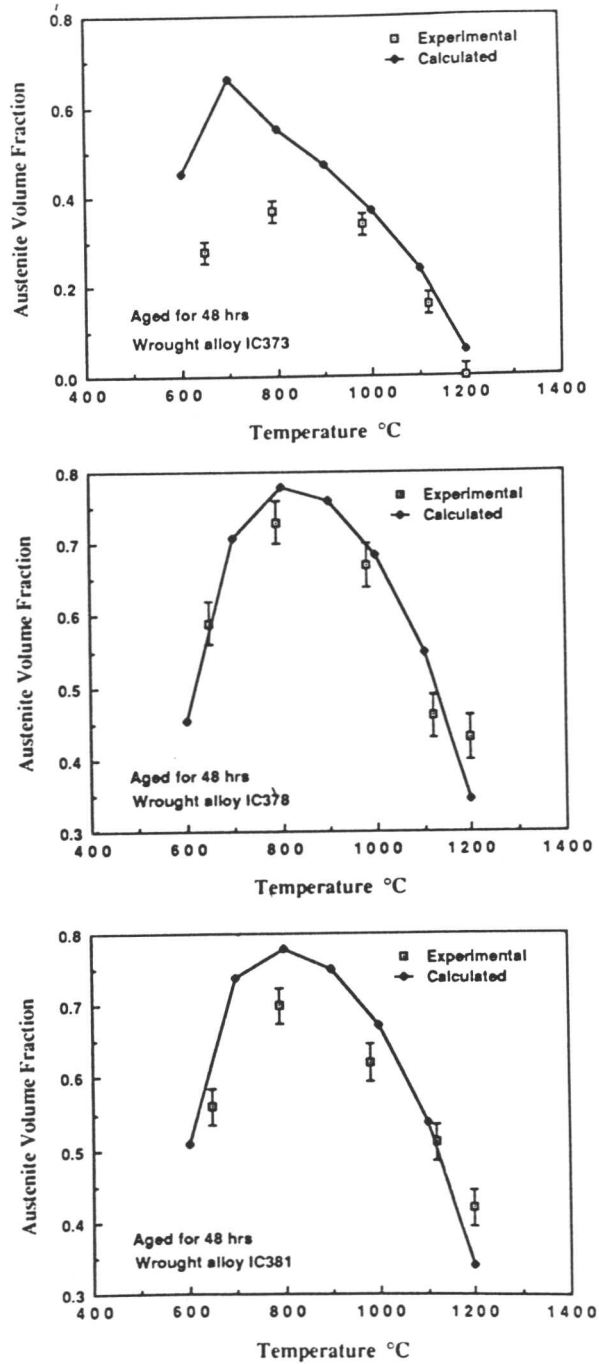


Fig. 7.9: Calculated and experimentally measured volume fractions of austenite as a function of ageing temperature in ICXXX wrought alloys. Experimentally measured austenite volume fraction is for an ageing time of 48 hours.

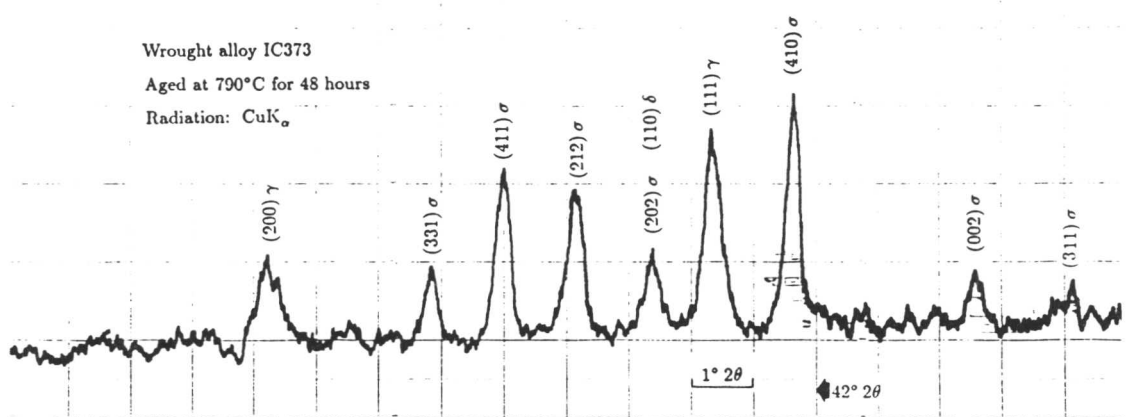


Fig. 7.10: X-ray diffraction pattern of specimen IC373 aged at 790°C for 48 hours obtained by bombarding the specimen with CuK_α radiation in a Phillips diffractometer.

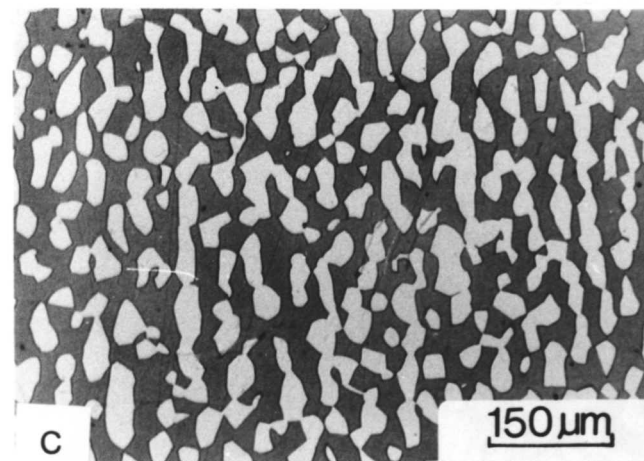
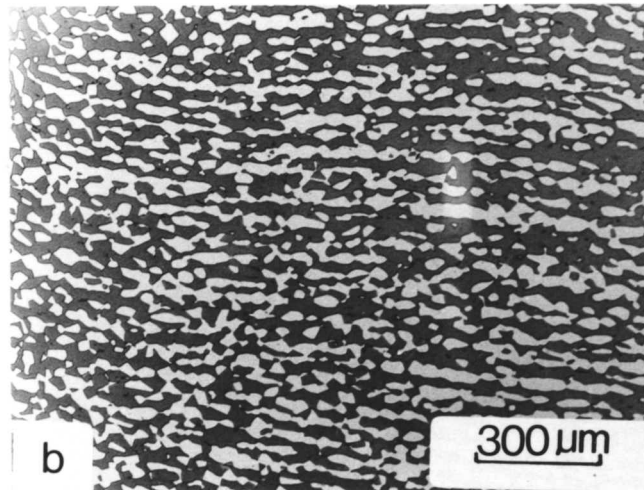
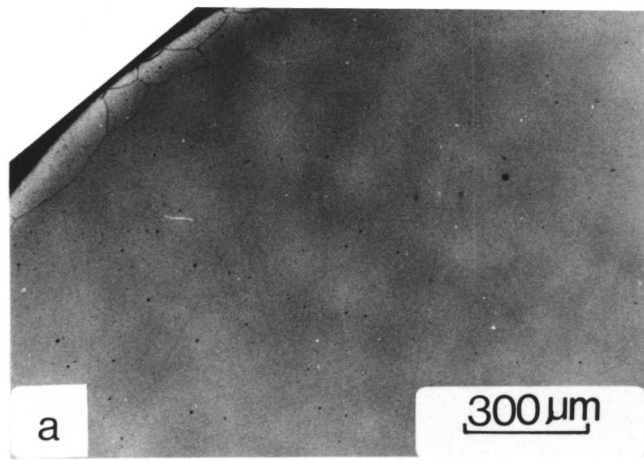


Fig. 7.11: The microstructure of ICXXX wrought alloys after ageing at 1200°C for 48 hours:

- (a) IC373, completely ferritic.
- (b) IC378, the white phase is austenite.
- (c) IC381, the white phase is austenite.

(a) shows that specimen IC373 has a lower ferritisation temperature than both IC378 and IC381 specimens because of its lower content of austenite formers and higher ferrite stabilizers. (b) and (c) shows that banding is still a feature of the microstructure of both IC378 and IC381 which implies the existence of segregation which in turn will have an effect on the concentration of the solute atoms in both phases.

The formation of sigma phase was found to be more intensive in IC373, compared with the other two alloys Figs. 7.12 & 7.13. This is due to the higher molybdenum and chromium contents in the former. The microstructural observations and hardness data suggest that the temperatures at which the occurrence of sigma phase is maximum in IC373 and both IC378 and IC381 are respectively about 790°C and 980° (Figs 7.13 & 7.14). The chemical compositions of the sigma and δ -ferrite phases as determined using EDX microanalysis unit attached to the “S4” scanning electron microscope are shown in Table 7.5 below:

Table 7.5: Sigma and δ -ferrite phase compositions at 980°C ageing temperature in wt.%. The calculated equilibrium composition of δ -ferrite was corrected for the interstitials carbon and nitrogen since they are not accounted for in the experimental data.

alloy	phase	Fe	Cr	Ni	Mo	Mn	Si	Cu
IC373	σ	53.6 ± 0.5	34.1 ± 0.4	2.96 ± 0.2	7.2 ± 0.2	0.79 ± 0.2	0.65 ± 0.2	0.52 ± 0.05
IC378	σ	57.3 ± 0.5	31.4 ± 0.4	2.56 ± 0.3	6.6 ± 0.25	2.03 ± 0.2	0.93 ± 0.2	0.11 ± 0.05
IC381	σ	56.6 ± 0.5	31.5 ± 0.35	2.94 ± 0.2	6.98 ± 0.3	1.8 ± 0.2	0.59 ± 0.2	0.14 ± 0.05
IC373	$\delta_{calc.}$	60.32	29.25	3.3	3.96	0.69	0.55	1.96
IC378	$\delta_{calc.}$	64.85	26.62	2.98	3.43	1.39	0.47	0.19
IC381	$\delta_{calc.}$	63.64	27.05	3.12	3.59	1.96	0.58	0.07
IC373	$\delta_{exp.}$	62.2 ± 0.5	28.6 ± 0.4	3.4 ± 0.2	2.44 ± 0.2	0.65 ± 0.2	0.47 ± 0.05	1.5 ± 0.2
IC378	$\delta_{exp.}$	65.8 ± 0.5	26.3 ± 0.4	2.5 ± 0.2	2.1 ± 0.2	1.7 ± 0.2	0.38 ± 0.05	0.09 ± 0.04

The large differences between the measured compositions and the calculated equilibrium composition of δ -ferrite at the temperatures where sigma phase was observed seem to explain the lower measured volume fractions of austenite compared with those calculated, such as the case with IC373 aged at 790°C.

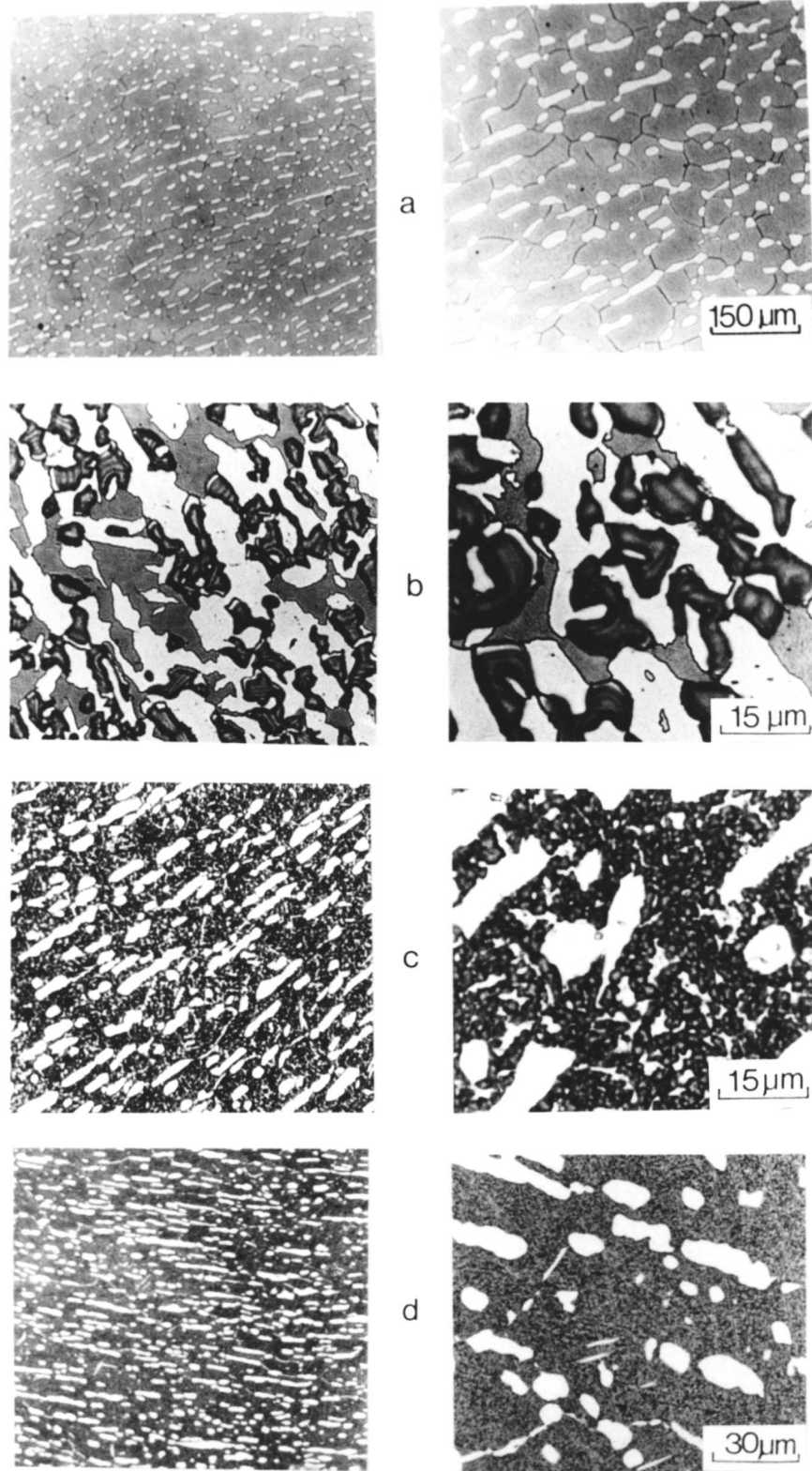


Fig. 7.12: Microstructure of samples of wrought duplex stainless steel IC373, after ageing for 48 hours at:

(a) 1120°C (b) 980°C (c) 790°C (d) 650°C

In a & d, the white phase is austenite and the dark phase is the δ -ferrite. In b & c, the white islands are austenite, the grey phase is δ -ferrite and the black phase is sigma. The micrographs also show the importance of segregation as banding is still observed all over the ageing temperature range.

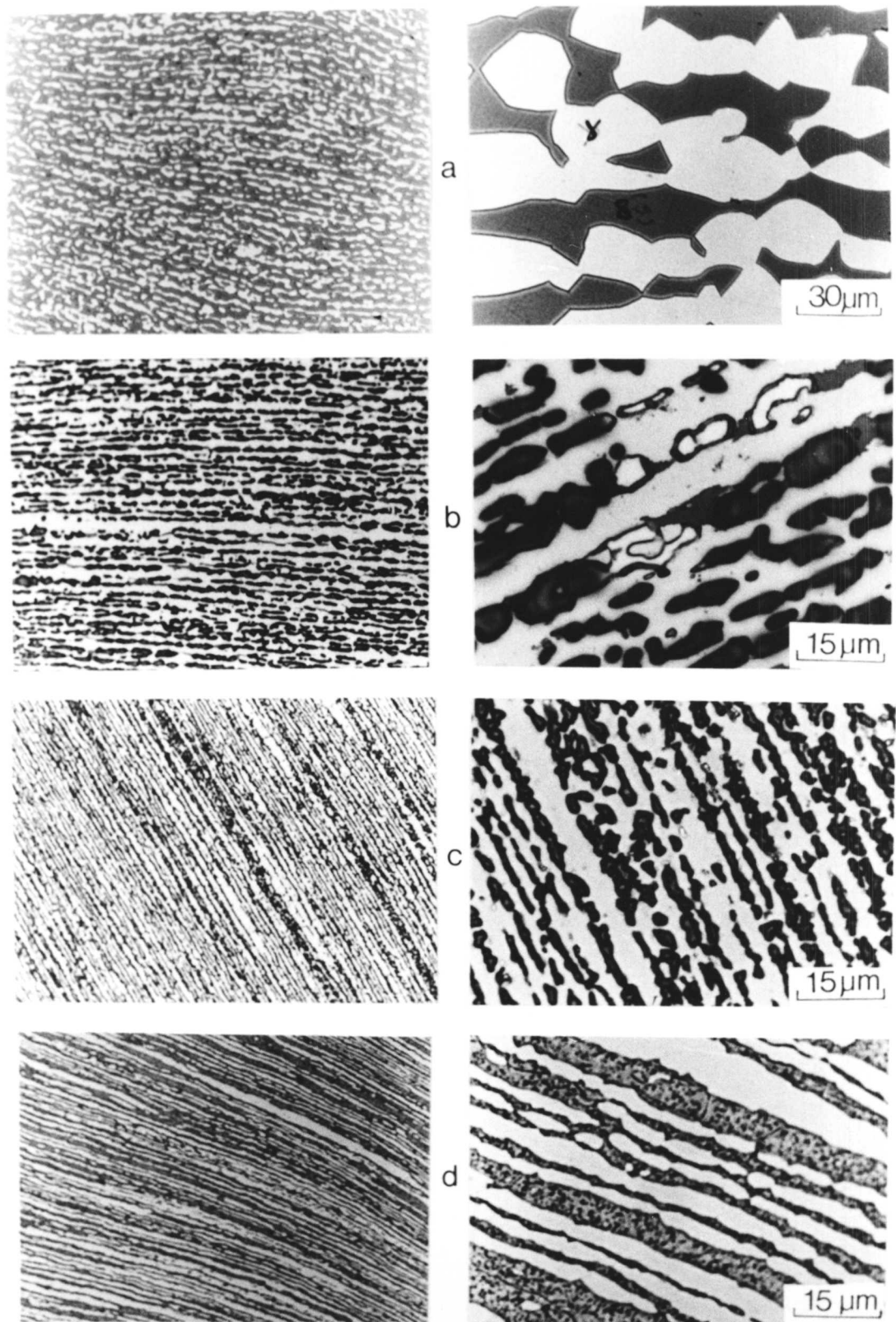


Fig. 7.13: Microstructure of samples of wrought duplex stainless steel IC378, after ageing for 48 hours at:

(a) 1120°C (b) 980°C (c) 790°C (d) 650°C

In a & d, the white phase is austenite and the dark phase is the δ -ferrite. In b & c, the white islands are austenite, the grey phase is δ -ferrite and the black phase is sigma. The micrographs also show the importance of segregation as banding is still observed all over the ageing temperature range.

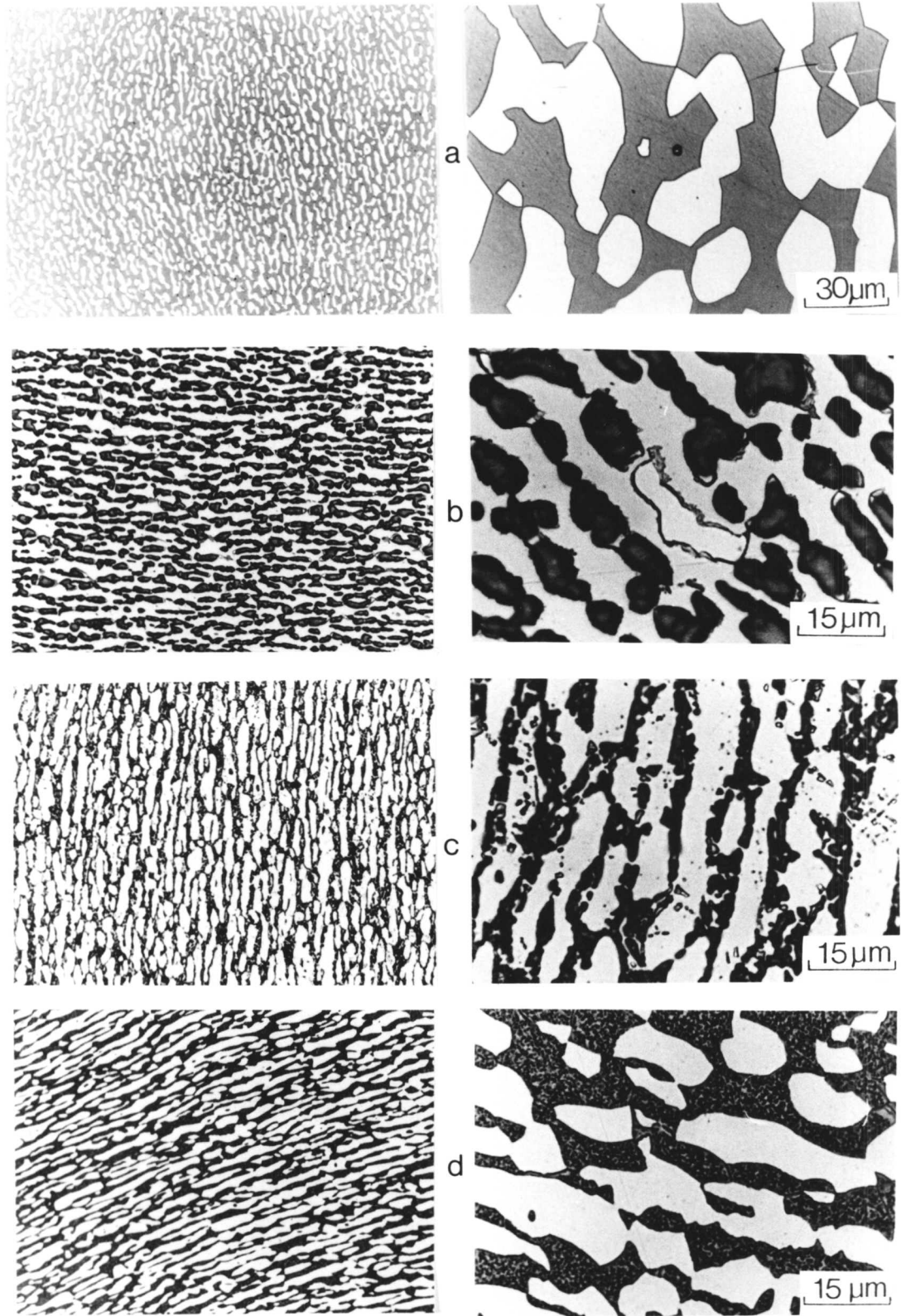


Fig. 7.14: Microstructure of samples of wrought duplex stainless steel IC381, after ageing for 48 hours at:

(a) 1120°C (b) 980°C (c) 790°C (d) 650°C

In a & d, the white phase is austenite and the dark phase is the δ -ferrite. In b & c, the white islands are austenite, the grey phase is δ -ferrite and the black phase is sigma. The micrographs also show the importance of segregation as banding is still observed all over the ageing temperature range.

7.3 Microstructure Hardness Relationship

Wrought alloys IC373, IC378 and IC381

The average of the measured Vickers hardness number (VHN5 kg) is plotted as a function of the ageing temperature in Fig. 7.15. The pattern observed is similar for the three alloys. The hardness was observed to increase between 700 and 790°C to a peak at 790°C. For higher temperatures, the hardness decreases to a minimum at 1120°. The observed peak in the hardness is due to sigma phase formation at the lower temperatures, the highest peak belongs to IC373 which contains a higher concentration of the sigma phase promoters chromium and molybdenum. The decrease in hardness as the ageing temperature increases between 800 and 1120°C is attributed to the increase in the austenite volume fraction. The increase of hardness at 1200°C compared with 1120° is consistent with the increase in δ volume fraction, which is harder than the austenite (Table 7.6).

Wrought alloys SH and SHP and welded alloy WR4

The measured Vickers hardness versus temperature curves obtained for SH, SHP and WR4 alloys, implies a similar trend to that observed with IC373, IC378 and IC381 (Fig. 7.16). The highest hardness number was obtained at 800°C, confirming the effect of sigma phase formation on the hardness. The increase in δ content at temperatures higher than 1100°C was associated with an increase in the measured hardness. A comparison between the curves of the three alloys reveals the effect of the starting condition before ageing on the overall hardness obtained after the ageing treatment. Wrought alloy SHP, which was solution treated in the single δ phase region prior to the ageing treatment, was found to possess the lowest overall hardness, which is believed to be the effect of the relatively coarser delta grain size, which in turn determines the morphologies of the austenite and other phases formed during the subsequent ageing. The volume fraction of the allotriomorphic austenite is comparatively high in the aged SHP specimens at all ageing temperature which explains the lowest hardness obtained for this alloy. The negative effect assumed by the allotriomorphic ferrite in the high strength low alloy steel (HSLA) welds in degrading the properties is analogous to the observed effect of allotriomorphic austenite in reducing the overall hardness in wrought alloy SHP. The highest hardness peak was observed for alloy SH at 800°C which is attributed to the combined effect of sigma phase precipitation and the relatively finer grain size, since the specimen was swaged prior to ageing, and subsequently to the

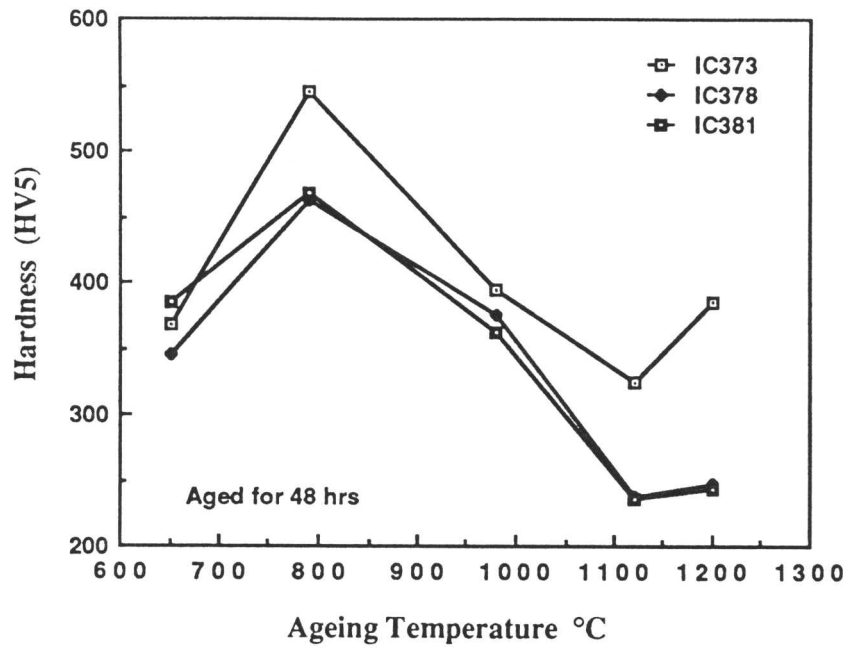


Fig. 7.15: Average Vickers hardness as a function of the ageing temperature of ICXXX wrought alloys aged for 48 hours.

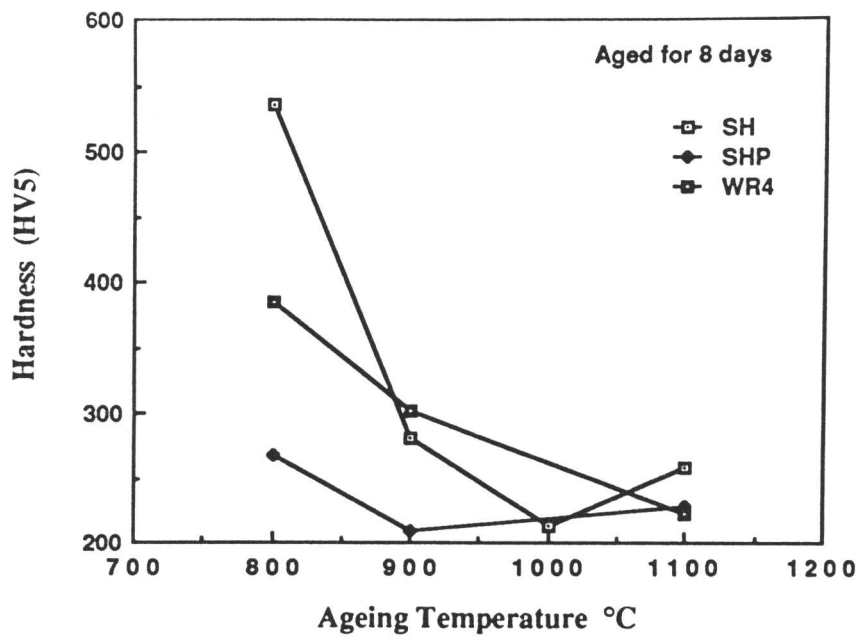


Fig. 7.16: Average Vickers hardness versus temperature for wrought alloys SH and SHP and weld metal WR4 aged for eight days.

occurrence of recrystallisation and to the limited grain growth at this temperature.

The lower chromium content and the higher nickel and nitrogen contents in WR4 are expected to delay the sigma phase formation, and to reduce its overall volume fraction. Consistent with this hypothesis the highest hardness observed at 800°C was much lower compared to that of SH alloy.

Law of Mixtures

In an attempt to account for the measured Vickers hardness on the basis of a law of mixtures, Vickers hardness was calculated from the available measured volume fractions of the phases present and their microhardness values (Table 7.6) as stated in equation below:

$$H_{\text{Total}} = H_{\delta}V_{\delta} + H_{\gamma}V_{\gamma} + H_{\sigma}V_{\sigma} \quad (7.1)$$

Where

H = calculated total hardness

H_{δ} , H_{γ} and H_{σ} are the measured microhardnesses of δ , γ and σ respectively

V = measured volume fraction

when more than one morphology of austenite was present the term for austenite was split into the number of morphologies ^{that occurred} if the hardness was measurable *i.e.* due to limitation of the microhardness testing device or to the size of the particles to be measured. The correlation between the measured (bulk) hardness and the [†]estimated on a law of mixture basis (Table 7.7) was 0.83 (Fig. 7.17). Although the calculations seem to overestimate the hardness at low hardness values, however, considering the accumulated margin of error in the measurements, the equation still provides a useful means of estimating the total hardness and suggests that a law of mixture [‡]do[‡] apply approximately. This approach is thought to be useful if extended to weld metals to predict possibly the strength via hardness measurement by knowing the microstructural constituents of the welded zone and after estimating a microstructural factor for the contribution of microstructure.

Table 7.6: The measured volume fractions and hardnesses of the phases present after ageing treatments in some of the wrought and welded alloys investigated in this project.

Alloy	T _{ageing} (°C)	t _{T_{ageing}} (hrs)	Volume Fraction			Micro-Hardness		
			γ	δ	σ	γ	δ	σ
SH	1160	192	0.11	0.89		271 ± 12	291 ± 7	
SH	1000	192	0.3	0.7		274 ± 9	289 ± 11	
SH	900	192	0.36	0.44	0.2	301 ± 8	327 ± 9	787 ± 164
SH	800	192	0.51		0.49			807 ± 179
SHP	1100	192	0.1	0.9		283 ± 8	296 ± 9	
SHP	900	192	0.35	0.65		230 ± 8	277 ± 12	261*
SHP	800	192	0.27					
WR4**	1100	192	0.66	0.35		235 ± 12	306 ± 13	267* ± 17
WR4	900	192	0.82		0.18	277 ± 22		579 ± 45
WR4	800	192	0.84		0.16	261 ± 23		574 ± 43
IC373	1200	48	0.00	1.0			422 ± 14	
IC373	1120	48	0.16	0.84		294 ± 4	428 ± 19	
IC373	980	48	0.34					
IC373	790	48	0.37					
IC373	650	48	0.28					
IC378	1200	48	0.43	0.57				
IC378	1120	48	0.46	0.54		267 ± 13	291 ± 9	
IC378	980	48	0.67					
IC378	790	48	0.73					
IC378	650	48	0.59					
IC381	1200	48	0.42	0.56		289 ± 10	360 ± 7	
IC381	1120	48	0.51	0.49		264 ± 10	287 ± 14	
IC381	980	48	0.62					600
IC381	790	48	0.7					
IC381	650	48	0.56					

where * is acicular austenite and the γ is allotriomorphic austenite.

** The measured hardness of Widmanstätten austenite is 287 ± 14.

The error in the measured volume fraction is around ±0.03.

Table 7.7: The measured Vickers hardness numbers of the aged wrought and welded alloys as compared to the calculated hardness obtained using equation 7.1:

Alloy	T_{ageing} (°C)	$t_{T_{\text{ageing}}}$ (hrs)	Hardness	
			Measured	Calculated
SH	1160	192	259	288
SH	1000	192	214	276
SH	900	192	281	362
SH	800	192	536	531
SHP	1100	192	223	294
SHP	900	192	210	265
WR4	1100	192	223	278
WR4	900	192	302	331
WR4	800	192	384	328
IC378	1120	48	237	280
IC381	1200	48	243	322
IC381	1120	48	235	284

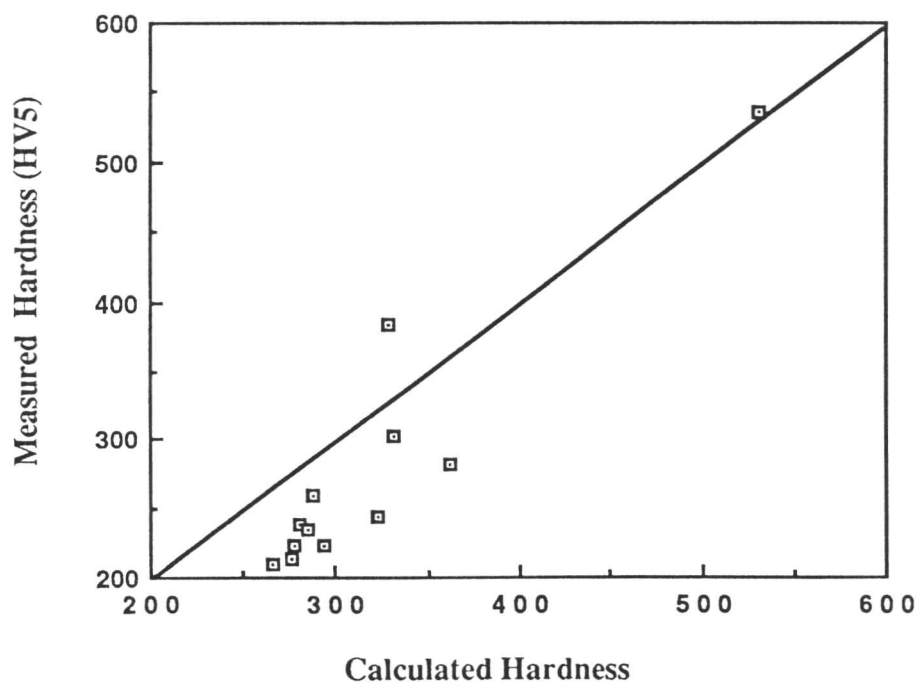


Fig. 7.17: Correlation between the measured Vickers hardness and the hardness calculated according to equation 7.1 for aged wrought and welded alloys.

7.4 Effect of Composition on the Calculated Equilibrium V_γ

As expected, the increase in carbon and nitrogen contents in alloy SH when compared with specimens of alloy SHP, led to an increase in the calculated volume fraction of austenite as a function of temperature as shown in Fig. 7.18. It led also to a slight increase in the ferritisation temperature of alloy SH compared with that of alloy SHP.

The effect of nickel as an austenite stabilizer is clear in Fig. 7.19. Alloy R2PP (9.11 wt% Ni) can be compared with R2P (7.5wt% Ni); there is a marked effect of nickel on the volume fraction of austenite as a function of temperature, particularly in the temperature range 700 to 1200°C, in spite of the fact that the manganese content of R2PP is 0.0 wt% while that of R2P is 1.32 wt%. This shows that although Mn is considered to be an austenite stabilizer, in duplex stainless steel its influence is less significant when compared with nickel. The effects of nitrogen and carbon are also illustrated in Fig. 7.19, when comparing WR2 with R2PP; the overall austenite contents at temperatures between 600 and 1000°C are increased with concentration, but again, there does not seem to be any profound effect on the ferritisation temperature, although WR2 has considerably higher Ni_{eq} value and approximately the same Cr_{eq} , calculated according to the empirical formulae discussed in chapter 2.

A comparison between the ICXXX wrought alloys (Fig. 7.20) shows clearly the effect of chromium as a ferrite former in reducing the calculated austenite volume fraction as a function of temperature in IC373 when compared with IC378 and IC381. Alloy IC387, at temperatures higher than 800°C was observed to have higher volume fractions of austenite compared with IC381, although its calculated Ni_{eq} and Cr_{eq} according to the empirical formulae (chapter 2) suggest that it should be lower. This may be attributed to the effect of cobalt, which is not accounted for in any of the empirical formulae, in acting as ferrite stabilizer in IC381.

The effect of chromium as a strong ferrite stabilizer is also shown in Fig. 7.21, when comparing the alloys designated MELT3 and MELT5. It reduces the austenite volume fraction by ≈ 0.12 for every 1 wt% increase in chromium content at 800 and 900°C. The increase in nickel content by 3 wt% in alloy MELT4 compared with MELT3 doubled the volume fraction of austenite. The effect of nickel is thought to be even larger on the

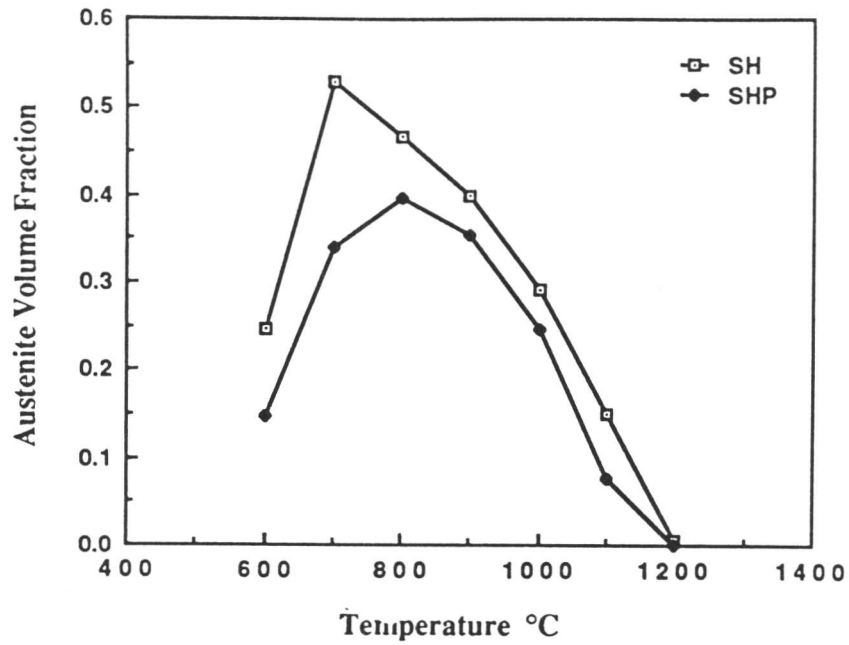


Fig. 7.18: Calculated equilibrium volume fractions of austenite as a function of temperature, for wrought alloys SH and SHP.

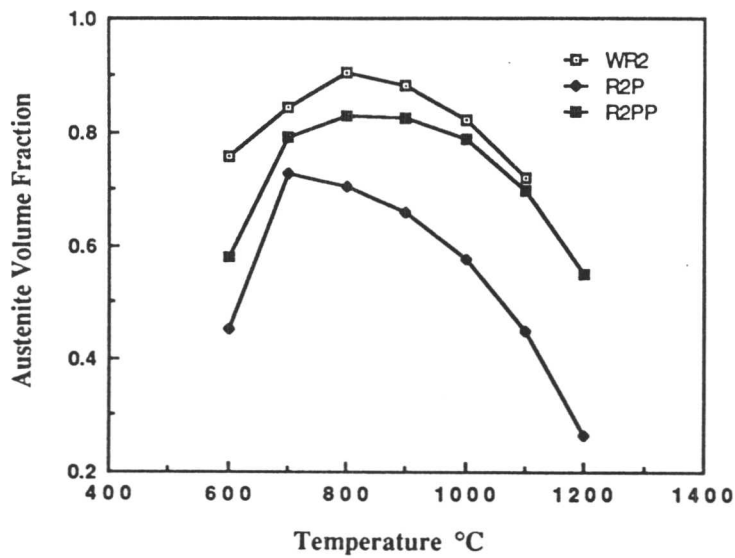


Fig. 7.19: Calculated equilibrium volume fractions of austenite as a function of temperature for welded alloy WR2, wrought alloys R2P and R2PP.

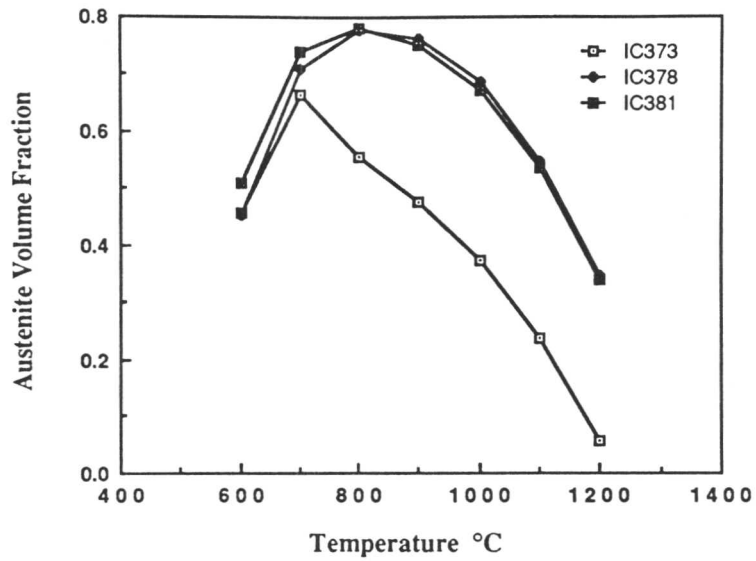


Fig. 7.20: Calculated equilibrium volume fractions of austenite as a function of temperature for wrought alloys IC373, IC378 and IC381.

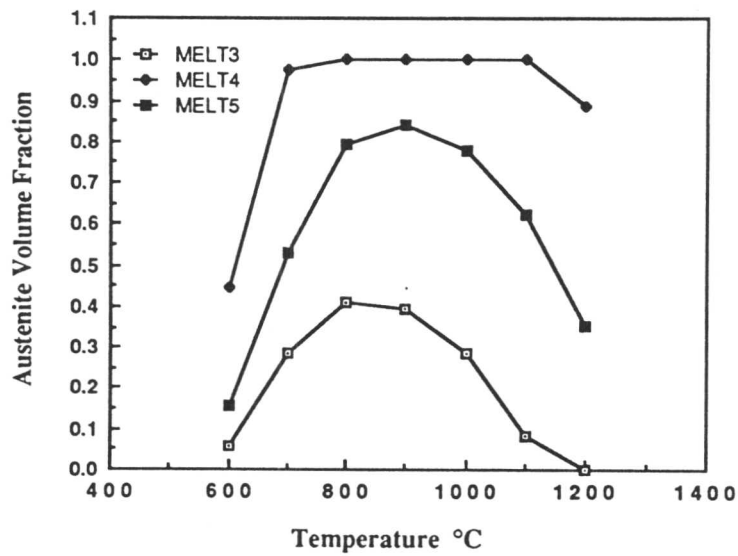


Fig. 7.21: Calculated equilibrium volume fractions of austenite as a function of temperature for model alloys MELT 3, 4 and 5.

austenite volume fraction since the molybdenum content of alloy MELT4 is about twice that of MELT3.

Carbon, nitrogen and nickel are also observed to increase the volume fraction of austenite in WR4 compared with R4P, as a function of temperature (Fig. 7.22).

7.5 The Partition Coefficient as a function of Temperature

To analyse the partitioning behaviour of the different alloying elements under equilibrium conditions, the calculated partition coefficient "K" is defined as C_γ/C_δ , where C_γ is the concentration of the element in austenite and C_δ is the corresponding concentration of the element in δ -ferrite. These data are listed in Appendix 2, Tables A.1, A.2 & A.3.

Wrought alloy SH

It was observed that $K(\text{Ni})$ decreases towards unity with increasing temperature from 600 to 1200°C Fig. 7.23. This means that as the transformation temperature increases, the partitioning of nickel into the austenite is reduced, consistent with the measured solubility of Ni in δ at the higher temperatures. The chromium partition coefficient was observed to decrease drastically from 600 to 700°C, away from unity, and then to increase with increasing temperatures up to 1200°C which also means that the difference of chromium between γ and δ decreases with increasing temperature. The maximum partitioning was observed at 700°C. The partitioning of Mo was observed to be nearly similar to Cr, but two differences were apparent: at 600°C, $K(\text{Mo})$ is > 1 , meaning that the concentration of Mo is higher in γ than in δ . As the temperature increases a sharp decrease in $K(\text{Mo})$ was observed to give a minimum at 700°C, after which any increase in temperature is associated with an increase in the $K(\text{Mo})$. $K(\text{Cu})$ was observed to decrease sharply from 2.3 at 600°C to 0.6 at 700°C leading to a drastic decrease of the copper concentration in austenite, and accordingly an increase of copper in the δ . Consequently $K(\text{Cu})$ increases with temperatures above 700°C to reach a value of 0.9 and to stay constant with further increases in temperature.

The behaviour of Mn was similar to that of Cu ^{between} the temperatures 600 and 700°C, as it was observed to decrease sharply from 2.0 to 1.1. For temperatures more than 700°C, it continued to decrease at a slower rate.

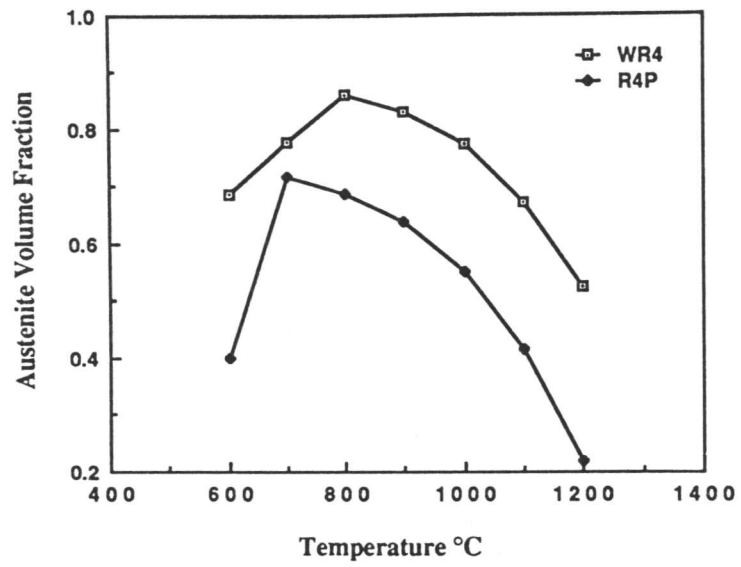


Fig. 7.22: Calculated equilibrium volume fractions of austenite of weld alloy WR4 and wrought alloys R4P as a function of temperature.

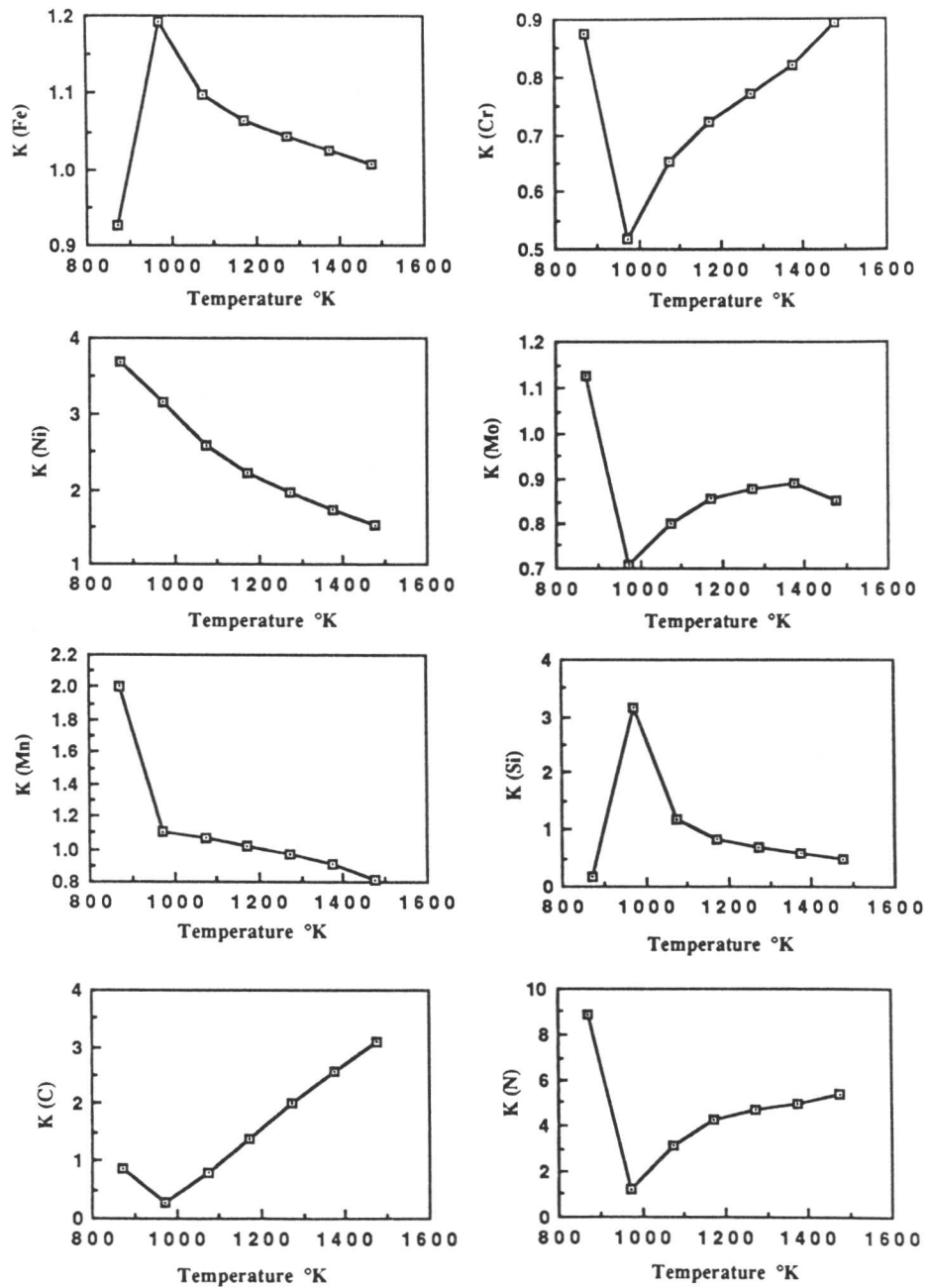


Fig. 7.23: The behaviour of the partition coefficient “K” defined as $C_{\gamma}(\text{wt}\%)/C_{\delta}(\text{wt}\%)$, calculated under two phase ($\delta + \gamma$) equilibrium conditions, as a function of temperature in wrought alloy SH.

(continued overleaf.)

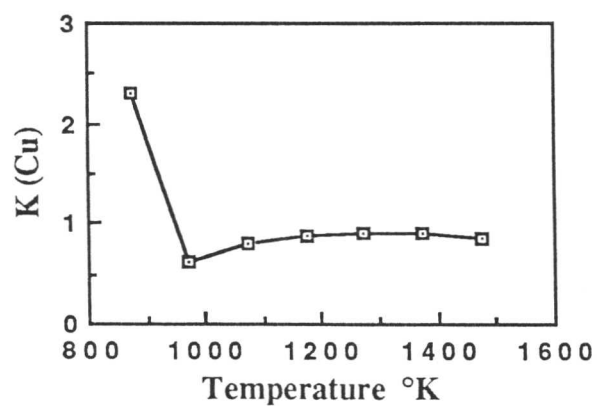


Fig. 7.23 cont.

Carbon and nitrogen coefficients were observed to increase for temperatures above 700°C leading to an increase in the difference of concentrations between γ and δ . The K values of nitrogen were relatively higher than those of carbon. From 700°C to 600°C, the partitioning of nitrogen increased rapidly. At these temperatures the concentration of carbon was noted to be higher in δ than in γ .

Iron and silicon were observed to exhibit the same K versus temperature behaviour. K(Fe) was found to increase rapidly from 0.92 at 600°C to ≈ 1.2 at 700°C, followed by a decrease with temperatures above 700°C towards unity. For silicon a rapid increase in K(Si) occurs from 0.2 at 600°C to 3.2 at 700°C, followed by a sharp decrease to around unity at 800°C, which continued with a slower rate with increasing temperature.

Wrought alloy SHP

K(Ni) as a function of temperature was observed to behave the same as that of SH Fig. 7.24. K(Cr) was found lower at 600°C than that of SH when compared. A constant K(Cr) was observed at 700 and 800°C. Above 800°C a linear increase in K(Cr) was observed. Similar to SH, a decrease in K(Mo) was observed from 600 to 700°C, which continued to decrease with slower rate down to 800°C. A gradual increase of K(Mo) was observed with further increase of temperature. K(Mn) behaviour was different than that of SH, a sharp increase from 0.2 at 600°C to 1.37 at 700°C was observed. With further increase in temperature K(Mn) was observed to decrease to reach slightly lower than unity. The carbon partition coefficient was observed to increase slowly from 0.4 at 600°C to about 0.8 at 800°C, when the carbon concentration was higher in δ than in γ , then increases linearly with temperature to reach a value of 2.8 at 1200°C. The nitrogen partition coefficient was found to be about ten times higher than that of carbon increasing rapidly from 3.7 at 600°C to ≈ 4.3 at 700°C, then more or less staying around this value with further increases in temperature.

K(Fe) was observed to be similar to that of SH with a shift in the peak to a higher temperature, *i.e.* 800 instead of 700°C. The silicon partition coefficient was also observed to shift its peak to 800 instead of the 700°C observed for SH, and the peak partition value was less than half that observed with SH. With further increases in temperature K(Si) was observed to decrease and reach a value of ≈ 0.75 at 1200°C.

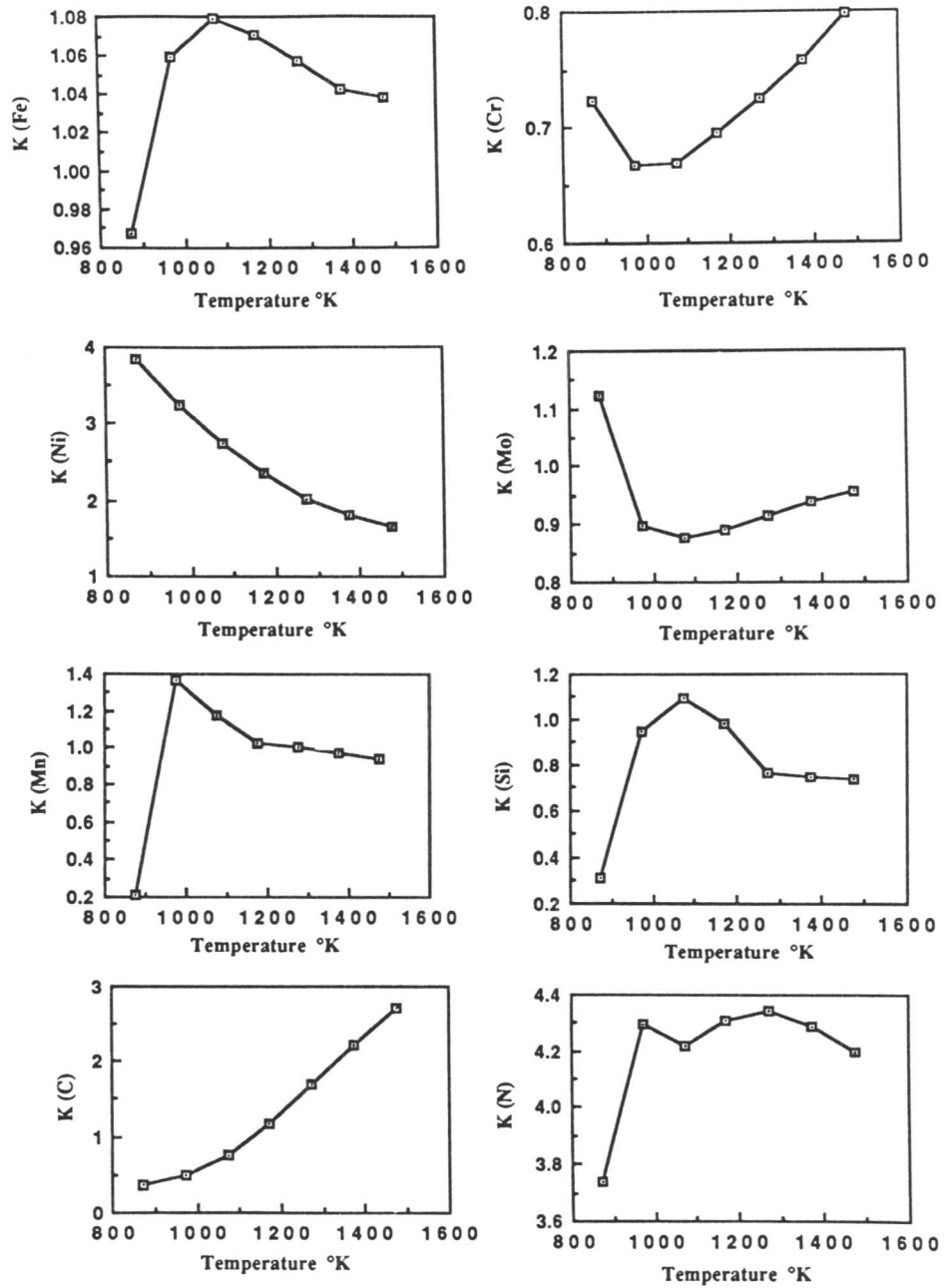


Fig. 7.24: The behaviour of the partition coefficient “K” defined as $C_{\gamma}(\text{wt}\%)/C_{\delta}(\text{wt}\%)$, calculated under two phase ($\delta + \gamma$) equilibrium conditions, as a function of temperature in wrought alloy SHP.

7.6 Calculated and Experimental Equilibrium Concentrations in δ and γ

A comparison between the calculated *and experimental substitutional elements concentrations in δ -ferrite and austenite for WR4 weld alloy is shown in Fig. 7.25. Iron and chromium experimental concentrations were observed to be in fair agreement with the calculated concentration. Experimentally measured Ni concentrations were found to be higher than those calculated in both austenite and δ -ferrite, particularly at the lower aging temperatures, but the general trend of nickel variation as a function of temperature was reproduced. It should be mentioned here that in fact the experimental concentration at 900°C ageing temperature is that of sigma phase and not δ -ferrite as it was mentioned earlier that at 900 and 800°C a duplex ($\gamma + \sigma$) structure was obtained.

In wrought alloy IC373 Fig. 7.26, disagreement was observed between the experimentally measured concentrations and the calculated ones, particularly at temperatures where sigma phase was observed to form. It was sometimes not easy to distinguish between the sigma phase and the δ -ferrite. It was observed that the scatter in the result was higher with IC373 than with IC381 (Fig. 7.27); this is possibly because of the higher chromium and molybdenum in the former, which are known to be sigma phase promoters. The preferred nucleation sites for σ phase are the δ/γ interfaces, and the mechanism by which it forms is still in dispute (see 2.7). It is believed on one hand that the severe partitioning of Cr and Mo is necessary for the formation of σ , while it is thought on the other hand that the precipitation of sigma is a rate controlled process, the evidence being the observation of δ with composition more or less the same as that of σ . The big scatter in the results of Mn and Si reflect the higher standard error obtained with their values. Molybdenum experimental measurements do not agree in most of the analysis carried out with the calculation. The segregation in molybdenum seems much higher than predicted by the equilibrium thermodynamic calculation. This could be a consequence of lower diffusion coefficient than the assumed in the calculations.

* Appendix 2

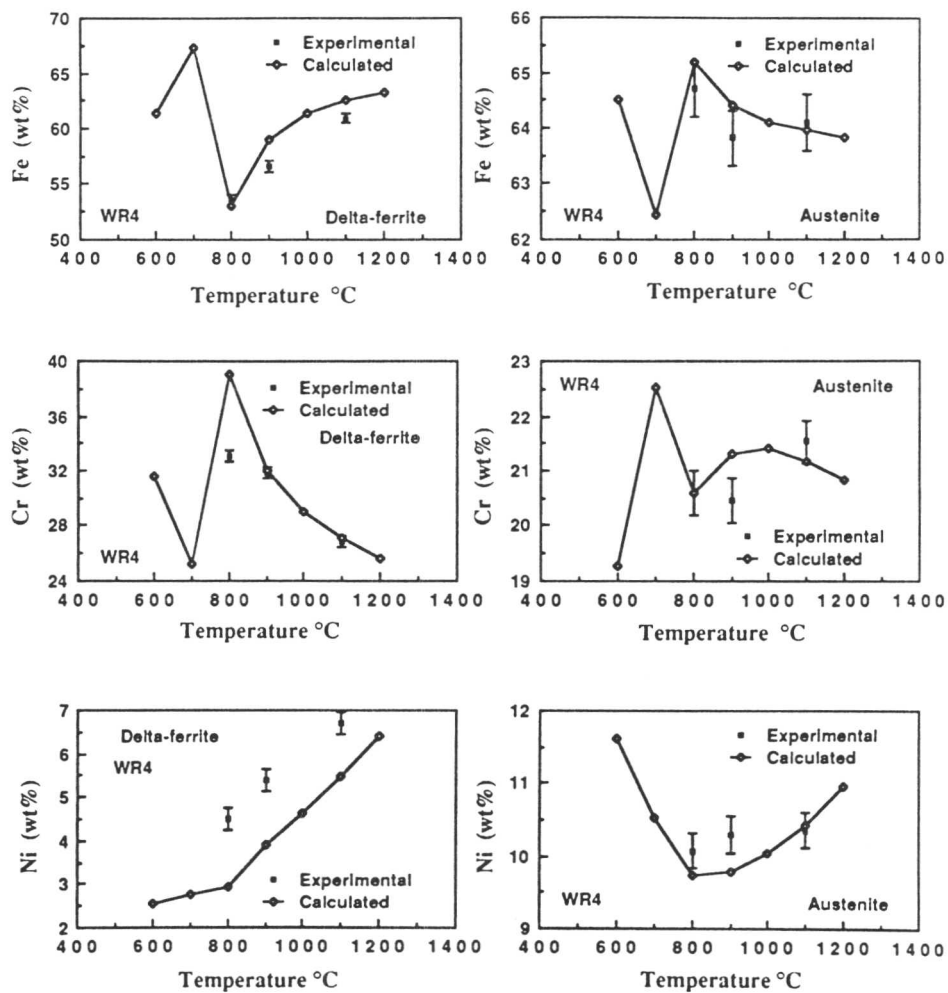


Fig. 7.25: Comparison between the calculated and experimentally measured (using EDX analysis on SEM) concentrations of substitutional solutes in δ and γ phases of weld alloy WR4 specimens aged for eight days. At 900°C the experimental concentration stated is that of σ .

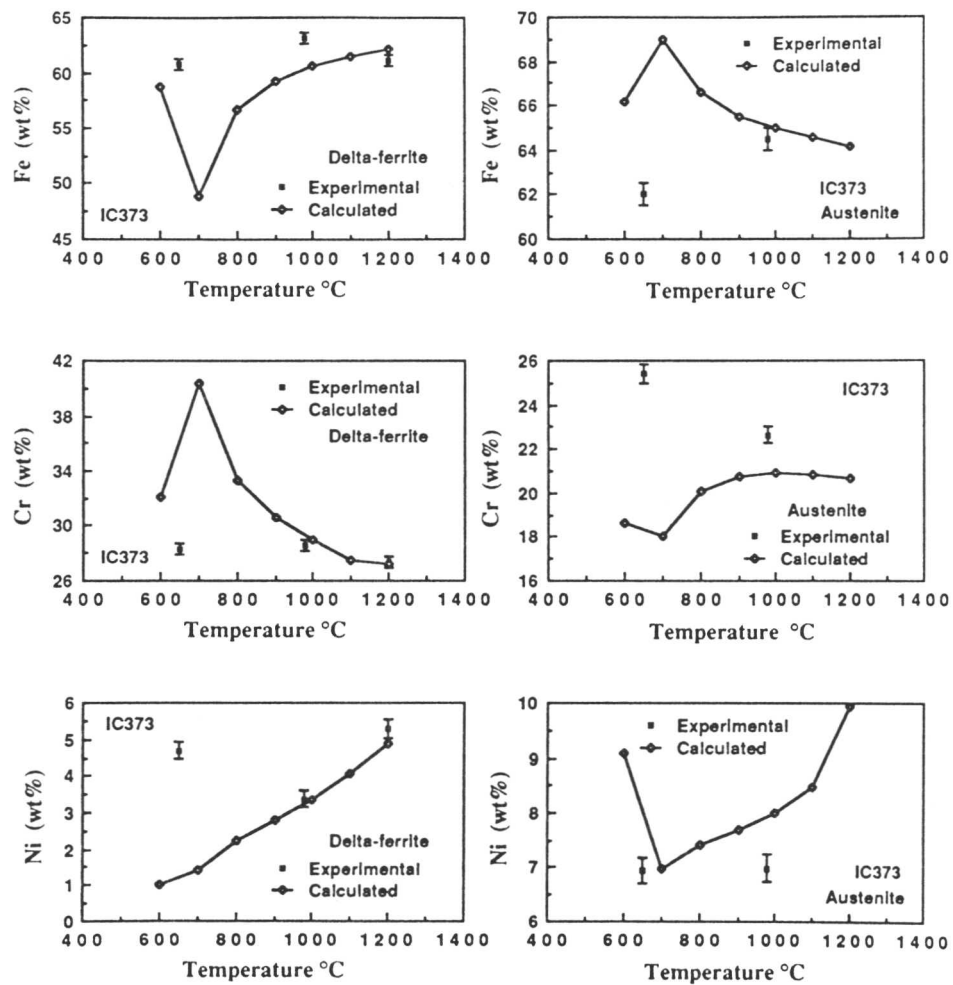


Fig. 7.26: Comparison between the calculated and experimentally measured (using EDX analysis on SEM) concentrations of substitutional solutes in δ and γ phases of wrought alloy IC373 specimens aged for 48 hours.

Continued overleaf.

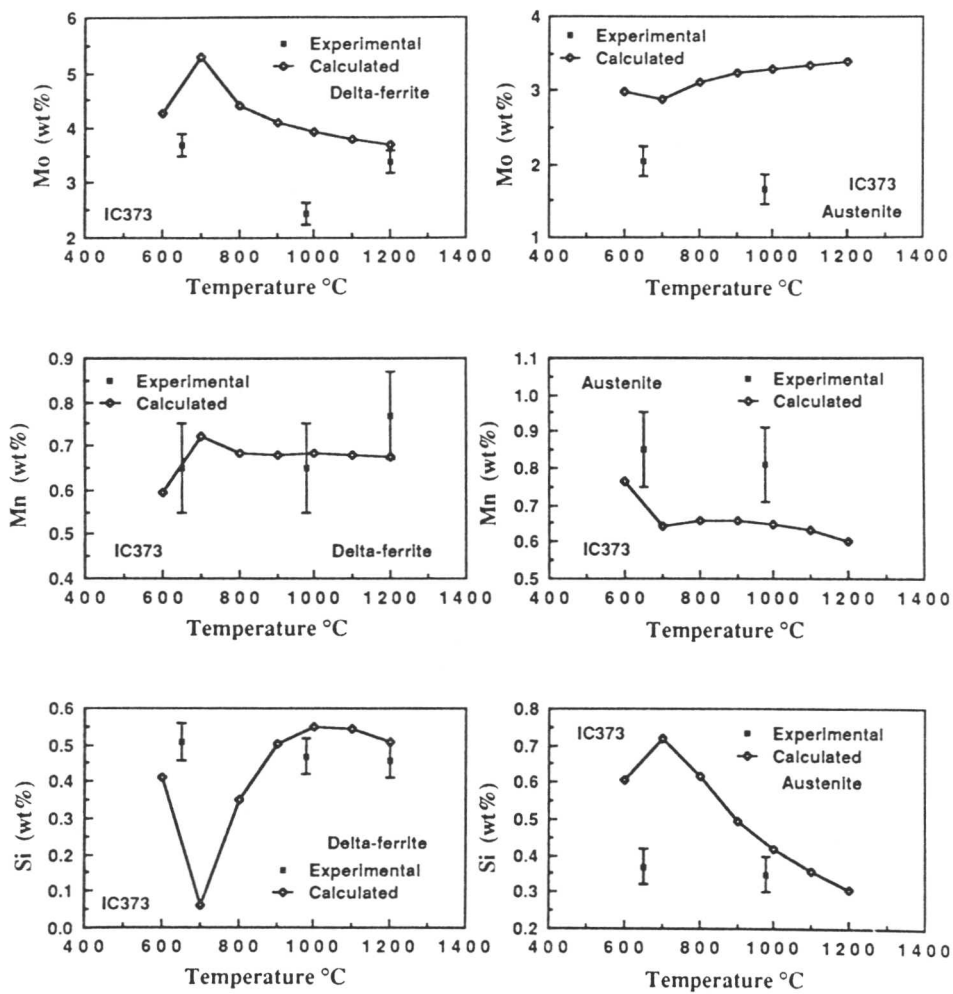


Fig. 7.26: cont.

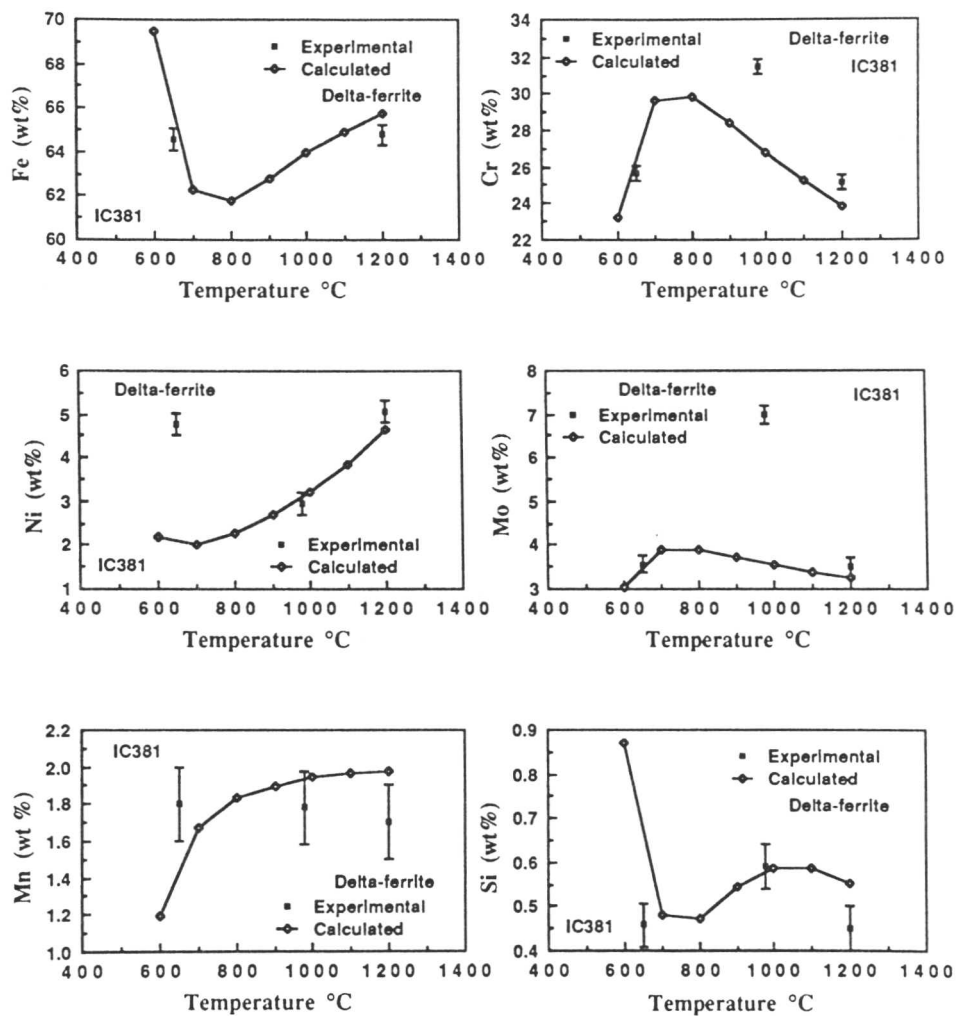


Fig. 7.27: Comparison between the calculated and experimentally measured (using EDX analysis on SEM) concentrations of substitutional solutes in $\delta + \gamma$ phases of wrought alloy IC381 specimens aged for 48 hours. At 980°C the experimental compositions stated are those of sigma phase.

(Continued Overleaf.)

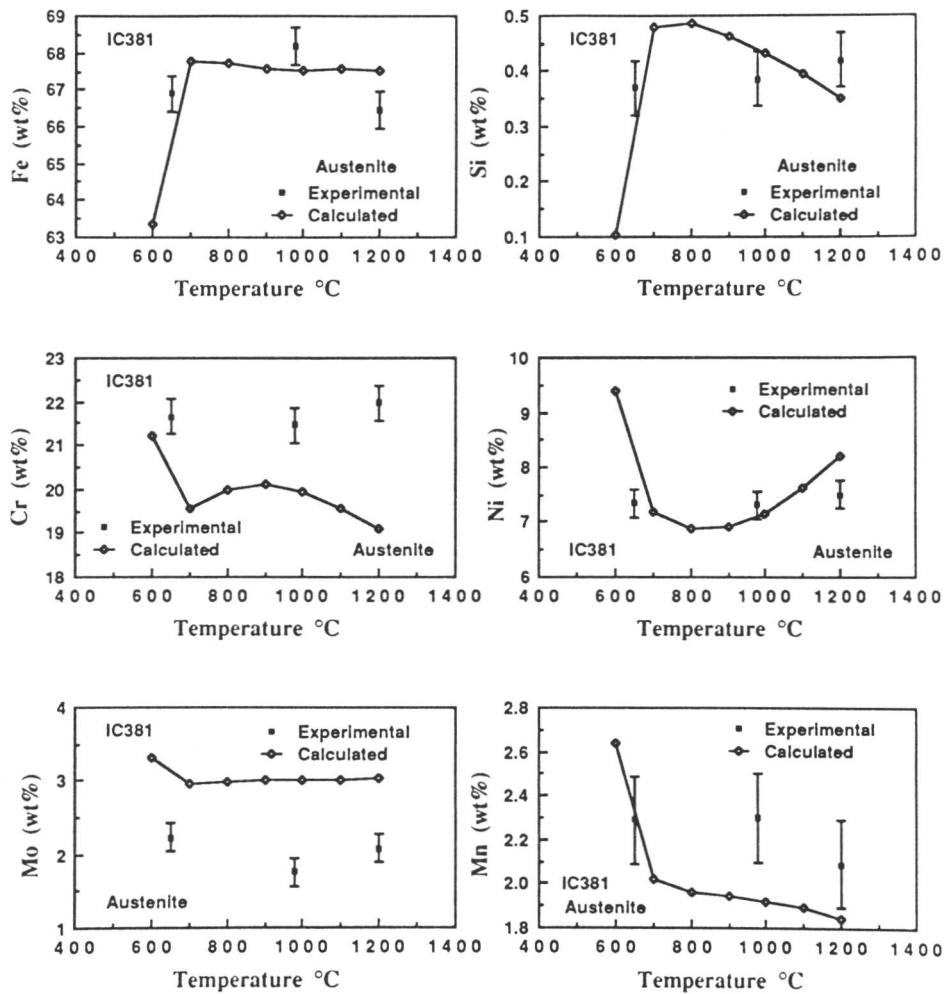


Fig. 7.27: cont.

7.7 Summary

In general the results obtained showed good agreement between the measured volume fractions of austenite and those expected from $(\delta + \gamma)$ equilibrium, for temperatures higher than the ones where sigma phase is formed. In the three phase regions, the agreement was good when the measured composition of the sigma phase was found near to that of the calculated δ -ferrite composition, like the case with WR4 and SH. It was also noticed that the higher the volume fraction of austenite the better the agreement.

The starting microstructure before the ageing treatment was observed to have an effect on the morphology of the product phases after the ageing treatment. With a deformed starting microstructure, ageing led to the formation of an equiaxed three phase microstructure by recrystallisation, while starting with a coarse columnar δ grain structure resulted in the formation of allotriomorphic layers of austenite, Widmanstätten austenite and acicular austenite by nucleation and growth processes. The analysis of the effect of the alloying elements on the basis of partitioning of alloying elements may not be adequate since the effect in fact is an overlapping of segregation and partitioning. In wrought alloys ICXXX and weld alloy WR4 the solidification induced segregation effect is obvious from banding in the microstructure, a feature which is retained at even temperatures as high as 1200°C. This makes it difficult to separate the effect of segregation from that of partitioning of alloying elements during the subsequent solid-state transformation.

The effect of the sigma phase in increasing the hardness was obvious in alloys IC373 and SH. It is concluded that the hardness of sigma phase increases with chromium percentage and decreases with higher austenite volume fraction. A law of mixture was found to apply approximately in estimating the hardness from the volume fractions of the individual phases and their respective microhardnesses.

The thermodynamic calculations confirm the austenitising effect of the interstitials and nickel, and the role of these elements in extending the $(\delta + \gamma)$ phase field to higher temperatures. They also confirm the ferritising effect of chromium and molybdenum.

Chapter 8

CONTINUOUS COOLING TRANSFORMATION

8.1 Introduction

Temperature-time isothermal transformation diagrams have been used widely in industry as a guide to heat treatment procedures. Nevertheless, in practice, the kinetic behaviour of an assembly at constant temperature is frequently of less importance than its behaviour during constant heating or cooling through a specified transformation range. In this chapter, the $\delta \rightarrow \gamma$ reaction is investigated under continuous cooling conditions using dilatometric measurements, since it is of more importance with respect to the conditions associated with weld metals. An attempt to establish the effect of δ -ferrite grain size on the non-isothermal $\delta \rightarrow \gamma$ reaction is also presented.

8.2 Continuous Cooling Transformation of Alloy SH

Homogenized[†] specimens with coarse δ grains were heated for 5 minutes at 1300°C to obtain a fully ferritic microstructure, and were then continuously cooled to 800°C at cooling rates (Q) ranging from 40 to 0.11°C s⁻¹, followed by rapid quenching with helium gas to ambient temperature. The transformation takes place at high temperature between 1200 and 800°C and the recommended cooling rate is less than 100°C s⁻¹ for weld metals (sec. 2.3.1). For $Q = 40$ to 1.27°C s⁻¹, the $\delta \rightarrow \gamma$ transformation was nearly completely suppressed, Fig. 8.1. Only a very thin discontinuous layer of austenite was observed on the δ/δ boundaries and very fine austenite particles were observed in the interior of the δ grains. This could be due to lack of sufficient nucleation sites since the specimens had a very coarse δ grain size of $\approx 600\mu\text{m}$.

The same continuous cooling treatment mentioned above carried out on deformed (swaged) specimens gave a remarkably higher volume fraction of austenite consistent with a hypothesis that transformation is accelerated on dislocations (Fig. 8.2). The microstructure of the continuously cooled deformed specimens was similar to that of isothermally transformed solution treated specimens. The Widmanstätten arrays of austenite near the grain boundaries increased in extent with slow cooling rate (0.11°C s⁻¹) in both the homogenized and deformed specimens, while the amount of intragranular austenite decreased.

[†] Solution treated at 1250°C for 72 hours.

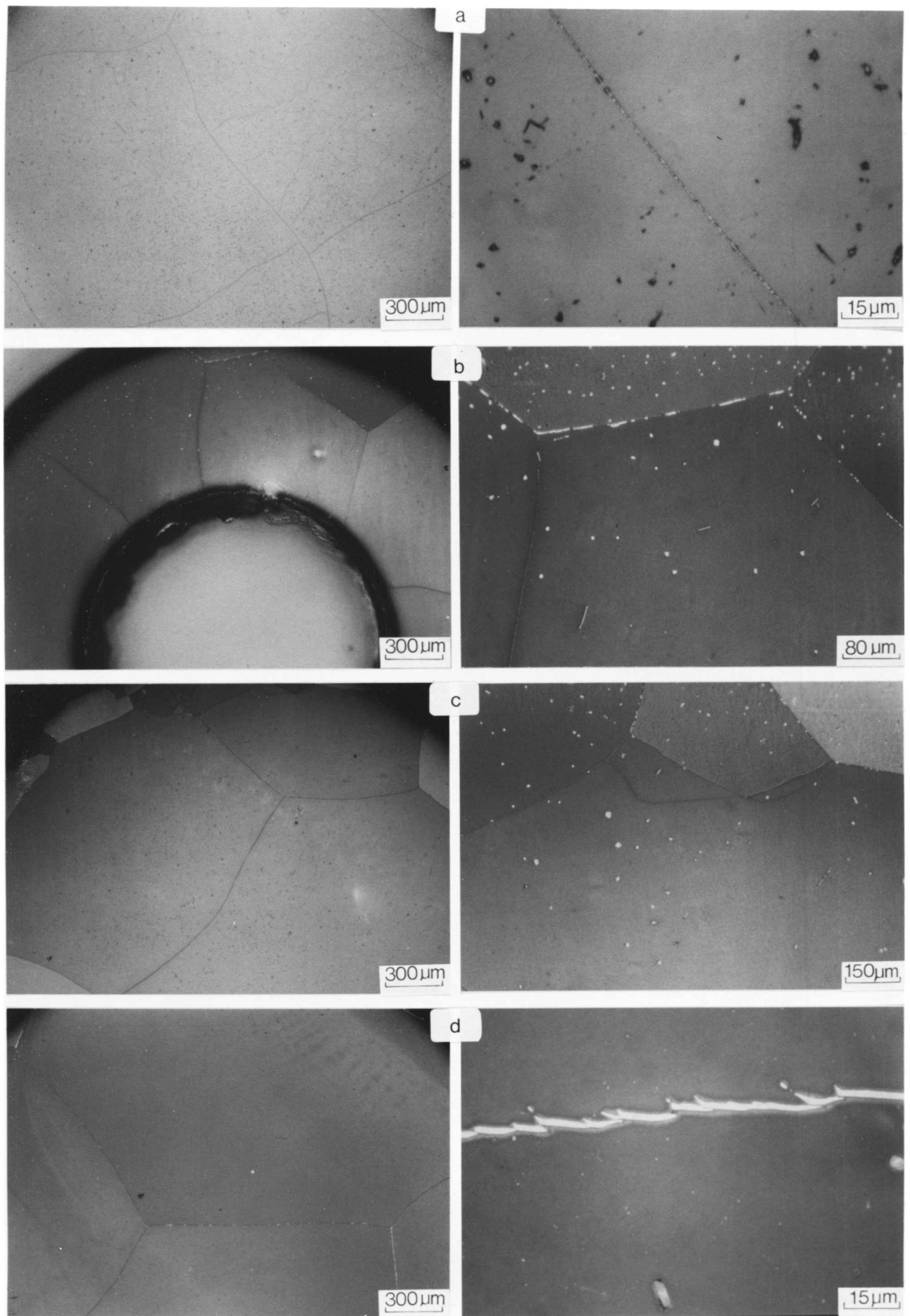


Fig. 8.1: A set of colour micrographs showing the microstructure of samples of coarse grained SH alloy after continuous cooling treatment at different cooling rates(Q): (a) $Q = 40^{\circ}\text{C s}^{-1}$, (b) $Q = 10^{\circ}\text{C s}^{-1}$, (c) $Q = 2.7^{\circ}\text{C s}^{-1}$, (d) $Q = 1.27^{\circ}\text{C s}^{-1}$. The etchant used is Beraha's colour etchant and the light etching phase is austenite.



Fig. 8.2: Microstructure of a deformed SH specimen after continuous cooling treatment ($Q = 0.11^{\circ}\text{C s}^{-1}$). The light etching phase is austenite.

Continuous Cooling Dilatometry

Consistent with the above results, the length/temperature profiles measured using high speed dilatometry (Fig. 8.3), show that there are no significant differences for cooling rates between 40 and $2.7^{\circ}\text{C s}^{-1}$. They also show that the transformation start temperature is higher for the low cooling rate ($0.1^{\circ}\text{C s}^{-1}$). The profile is more curved for the slowest cooling rate, in the high temperature range ($1300\text{-}1100^{\circ}$), than the profiles of the faster cooling rates when compared with a single δ phase profile. This indicates that the $\delta \rightarrow \gamma$ transformation commenced for the slower cooling rate at a higher temperature range. The change of profile is a consequence of different expansivities of the two phases involved δ and γ , and as mentioned earlier in chapter 6, these expansivities and particularly that of δ are temperature dependent. The interpretation of the profiles in terms of austenite volume fraction will be discussed later.

8.3 Continuous Cooling Transformation of Wrought Alloy R4P

Previously solution treated (1160°C for 62 hrs) specimens were heated for 5 mins at 1340°C to obtain fully ferritic microstructures and were then continuously cooled to ambient temperature at three different cooling rates Q of 40, 2.5 and $0.11^{\circ}\text{C s}^{-1}$, using the high speed dilatometer. For $Q = 40^{\circ}\text{C s}^{-1}$, the microstructure was found to consist of thin layers of allotriomorphic austenite and fine Widmanstätten austenite which grew from the γ allotriomorphs. Intragranular austenite formation was completely suppressed and the measured volume fraction of austenite at ambient temperature was 0.08, (Fig. 8.4 a). For $Q = 2.5^{\circ}\text{C s}^{-1}$, the transformation of δ started with the formation of thin layers of allotriomorphic austenite followed by the rapid formation of a network of Widmanstätten austenite from the allotriomorphs, and also no intragranular austenite was observed to form, Fig. 8.4 b. At the slower cooling rate of $0.11^{\circ}\text{C s}^{-1}$, the microstructure was found to consist of relatively thicker layers of allotriomorphic austenite and Widmanstätten austenite of irregular morphology. σ phase was also observed, associated mostly with δ -ferrite/allotriomorphic austenite boundaries and grown into the δ -ferrite (Fig. 8.4 c). The measured volume fractions of austenite after the continuous cooling treatments are shown in Table 8.1. As expected, there is a decrease in the measured volume fraction of austenite as the cooling rate from the ferritising temperature is increased.

The length temperature profiles obtained on the high speed dilatometer (Fig. 8.5) show a decrease in transformation start temperature with increasing cooling rate. At

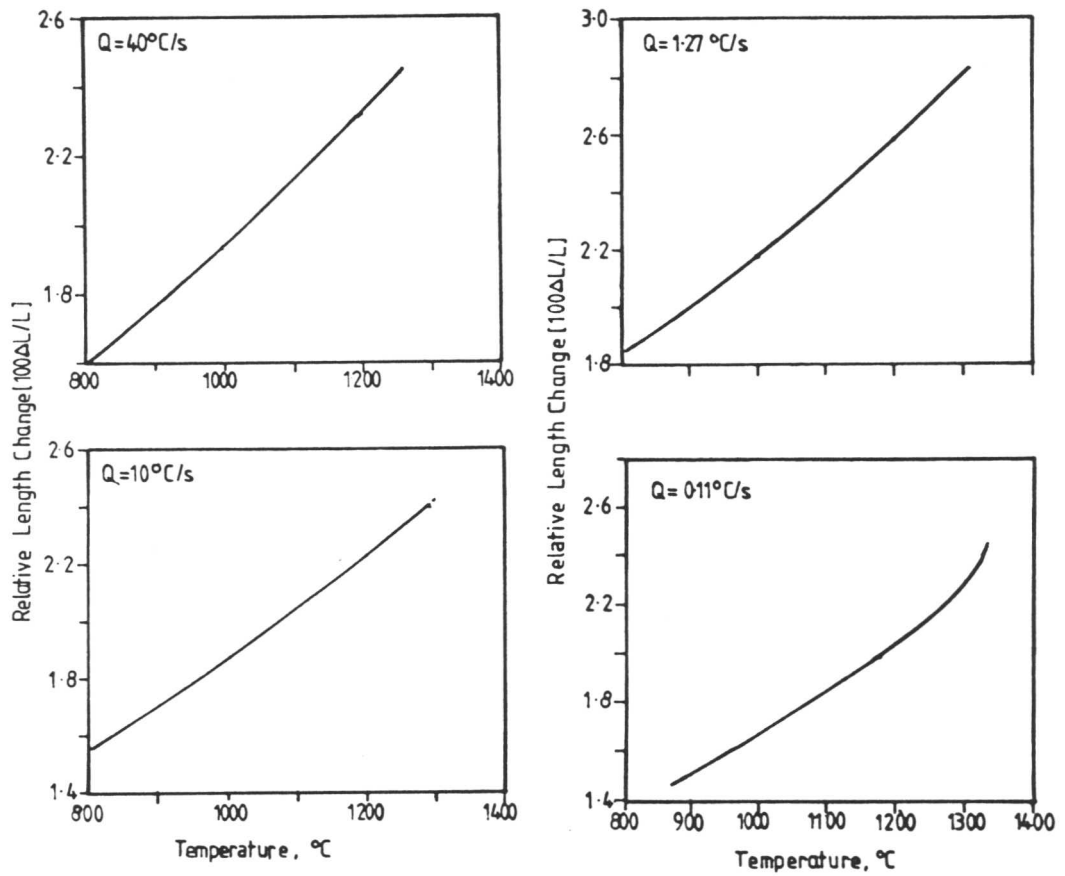


Fig. 8.3: Showing relative length change versus temperature profiles for continuous cooling transformation of SH specimens from T_{δ} at different cooling rate (Q), as obtained from dilatometric experiments.

($T_{\delta} = 1300^{\circ}\text{C}$, ferritisation time = 5 min.)

Table 8.1: Measured volume fractions of austenite in continuously cooled wrought alloys SH, R4P and welded alloy BW.

Specimen	$D^* \mu\text{m}$	$T_\delta(^{\circ}\text{C})$	$Q(^{\circ}\text{C s}^{-1})$	V_γ^{LI}
SH	600 ± 21	1300	40	< 0.03
SH	607 ± 19	1300	10	< 0.03
SH	588 ± 14	1300	2.5	< 0.03
SH	615 ± 19	1300	1.27	< 0.03
R4P	-	1340	40	0.08 ± 0.026
R4P	-	1340	2.5	0.37 ± 0.048
R4P	-	1340	0.11	0.55 ± 0.049
BW	-	1340	40	0.33 ± 0.04
BW	-	1340	5.4	0.69 ± 0.05
BW	-	1340	1.25	0.75 ± 0.06

Where D^* is the average grain size of δ -ferrite and V_γ^{LI} is the volume fraction of austenite. Both D^* and V_γ^{LI} were measured using the lineal intercept method.

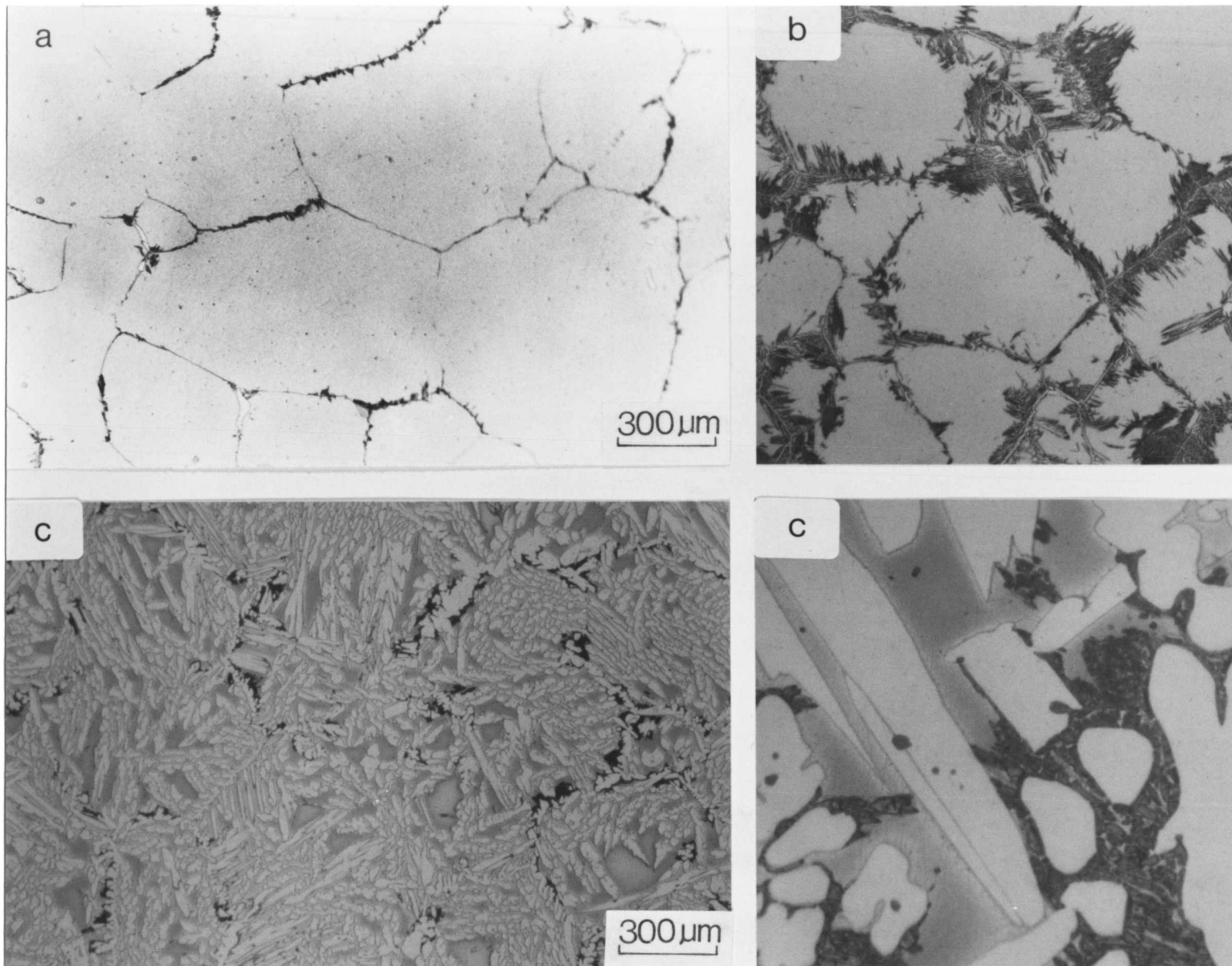


Fig. 8.4: A set of micrographs showing the microstructure of samples of alloy R4P after continuous cooling rate $Q =$: (a) $40^{\circ}\text{C s}^{-1}$, (b) $2.5^{\circ}\text{C s}^{-1}$, and (c) $0.11^{\circ}\text{C s}^{-1}$. The samples were electroetched in etching phase in (a) & (b) is austenite. In (c) the light etching phase is austenite and the dark b

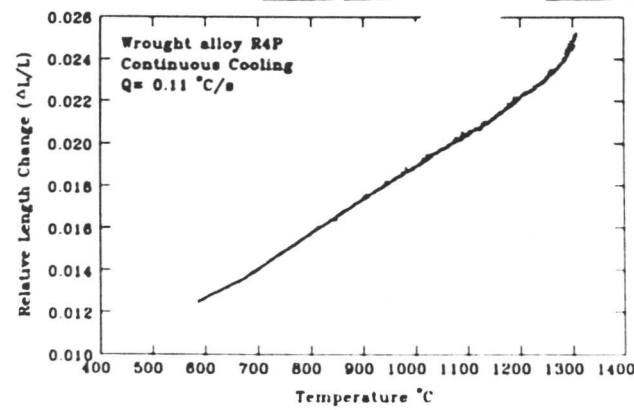
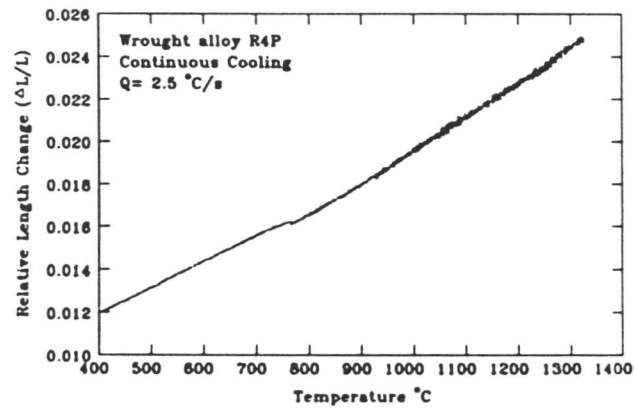
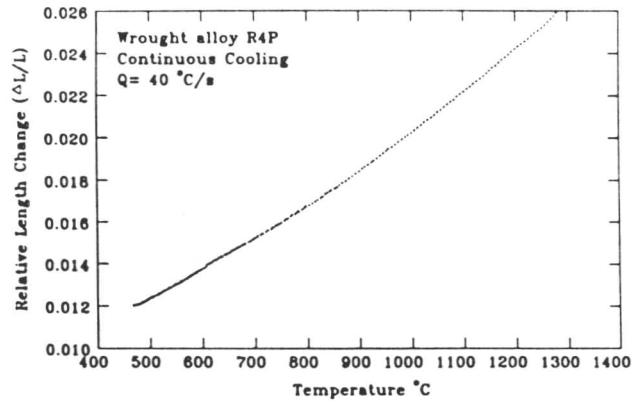


Fig. 8.5: Showing relative length versus temperature profiles for continuous cooling transformation of samples of alloy R4P at different cooling rate (Q). ($T_\delta = 1340^\circ\text{C}$, ferritisation time = 5 mins).

the slowest cooling rate, it is evident from the curvature of the profile that the transformation commenced at a higher temperature range compared with the faster cooling rates.

8.4 Continuous Cooling Transformation of Welded Alloy BW

Samples of alloy BW machined from the as-received welded joint were heated at 1340°C for 5 minutes in high speed dilatometer, and were then continuously cooled to ambient temperature at controlled cooling rates of 45, 5.2, and 1.36 °C s⁻¹. The microstructures of the samples are shown in Fig. 8.6. There are more or less continuous layers of austenite at the δ grain boundaries, together with austenite in a Widmanstätten like morphology. The interesting feature of the microstructure was the intragranular acicular austenite plates, which became the dominant morphology of austenite at the highest cooling rate $Q = 45^\circ\text{C s}^{-1}$. Sections of the acicular austenite revealed groupings of parallelepiped cross-sections with an overall shape of a chisel with one sharp edge Fig. 8.7. This may be explained by the tendency to lower the overall free energy by forming arrays in which any transformation strain is to some extent mutually accommodated.

With slow cooling rates, the acicular austenite grains were observed to be more irregular in shape as a result of hard impingement during growth. A comparison with the continuously cooled wrought alloy R4P, which has nearly the same concentrations of the major alloying elements, shows that the measured volume fractions of austenite (Table 8.1) are much higher in BW. The acicular austenite was completely suppressed in R4P while it was present in BW. This emphasises the role of inclusions in providing heterogeneous nucleation sites at the higher undercooling in the weld metal which has higher oxygen content.

The relative length versus temperature graphs are shown in Fig. 8.8. Again as observed with R4P and SH they show a decrease in transformation start temperature with increasing cooling rate from the ferritising temperature.

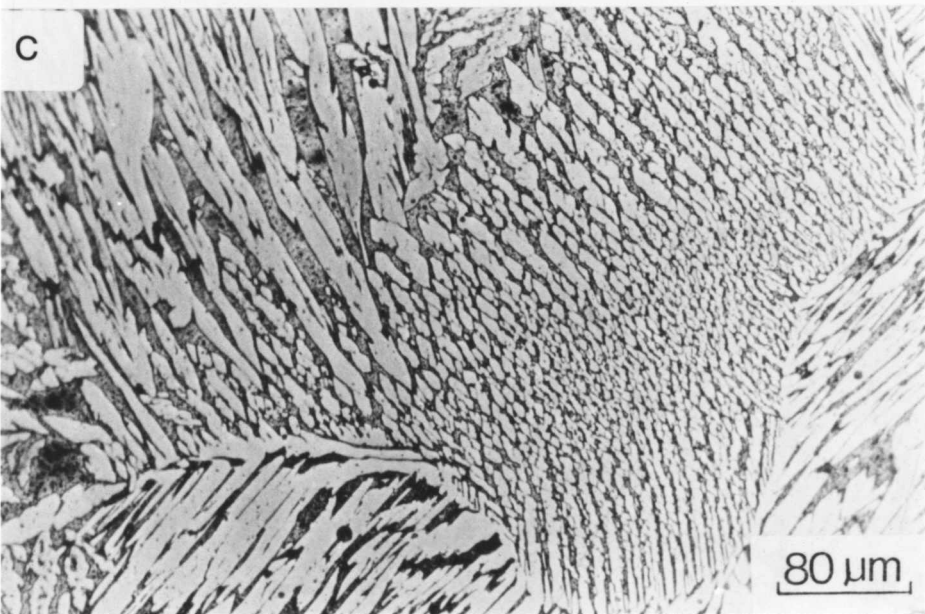
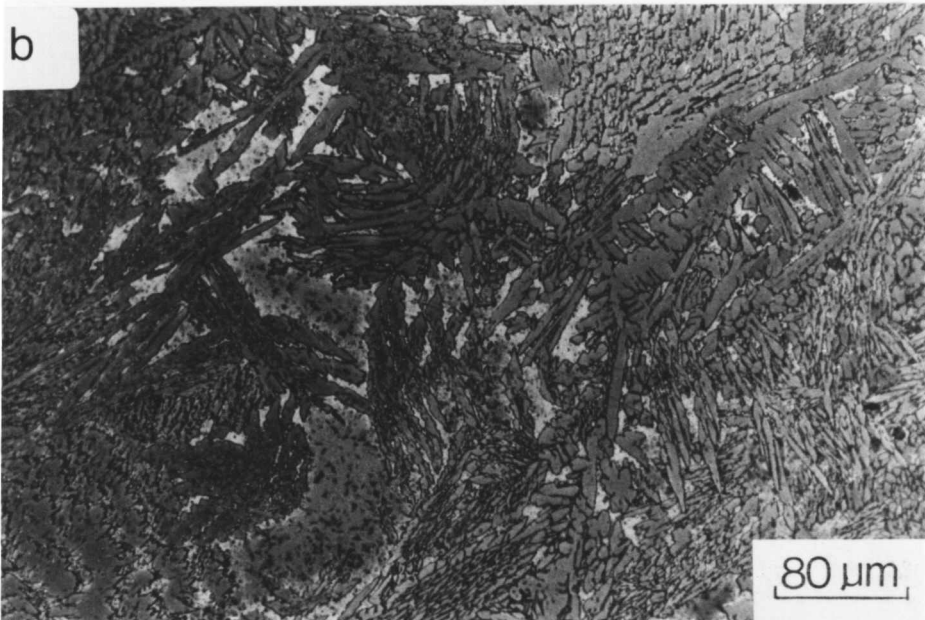
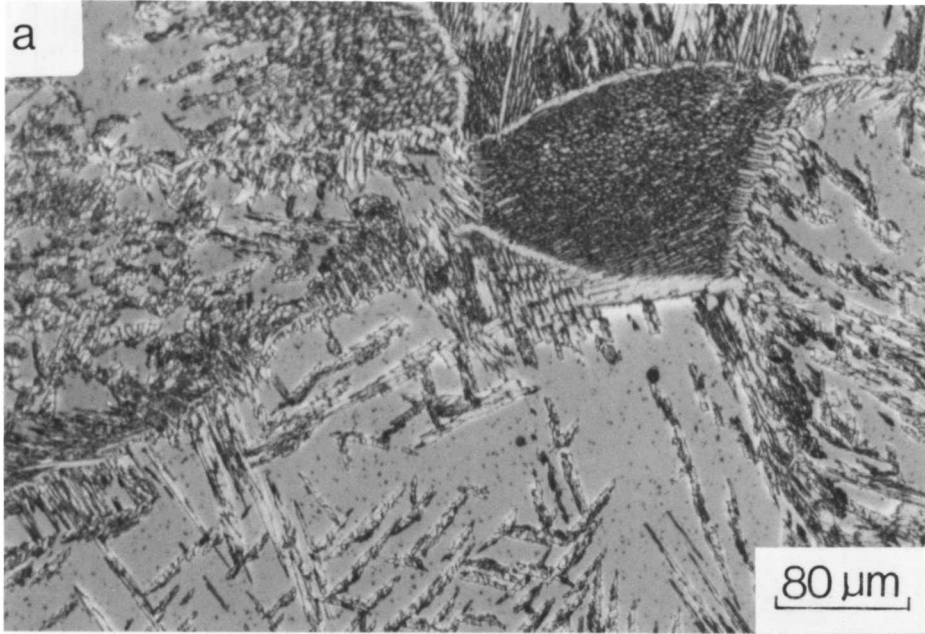


Fig. 8.6: Microstructure of samples of alloy BW after continuous cooling treatment:

- (a) $Q = 45^{\circ}\text{C s}^{-1}$
- (b) $Q = 5.2^{\circ}\text{C s}^{-1}$
- (d) $Q = 1.36^{\circ}\text{C s}^{-1}$

In (a) The yellowish coloured phase is δ . In (b) the dark etching phase is austenite and in (c) the austenite is the light etching phase. (Q = cooling rate).

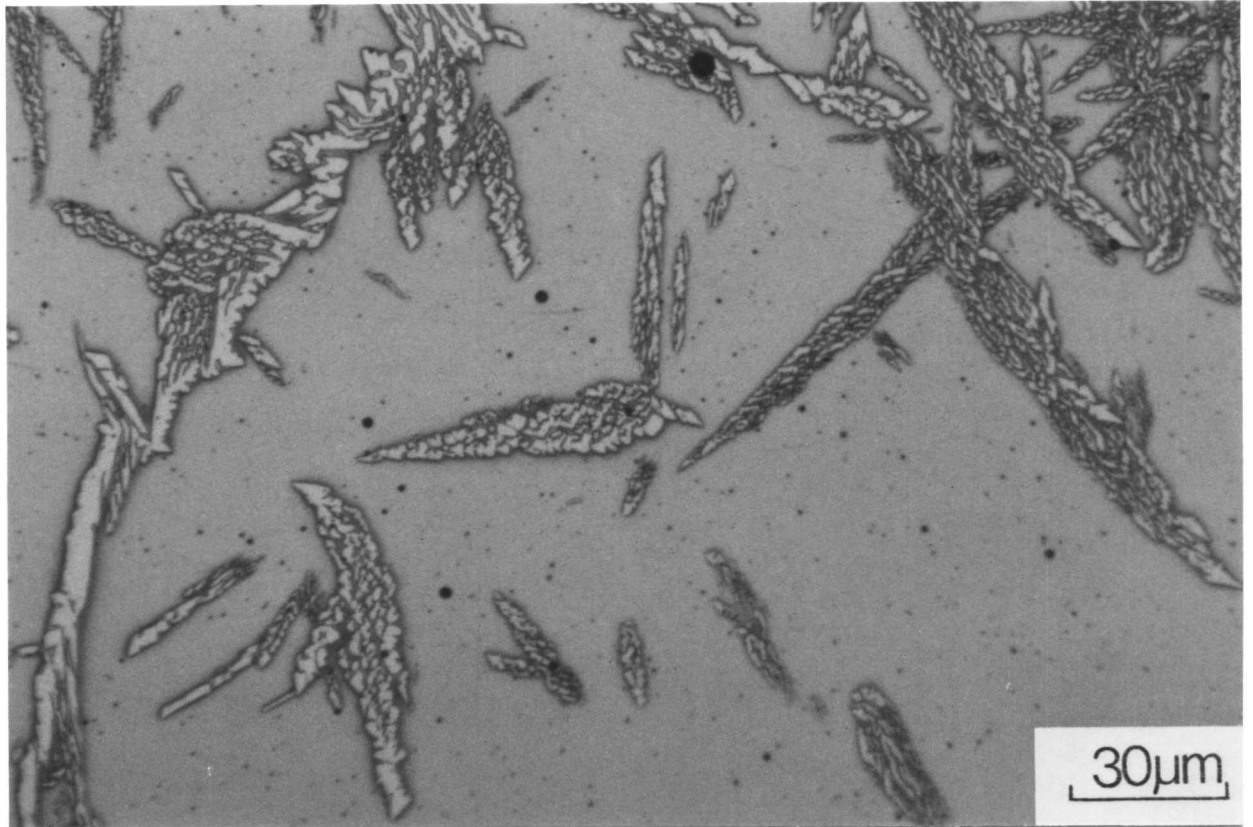


Fig. 8.7: Microstructure of a sample of alloy BW after continuous cooling transformation at a cooling rate of $45^{\circ}\text{C s}^{-1}$, showing the chisel shape of the intragranularly nucleated austenite.

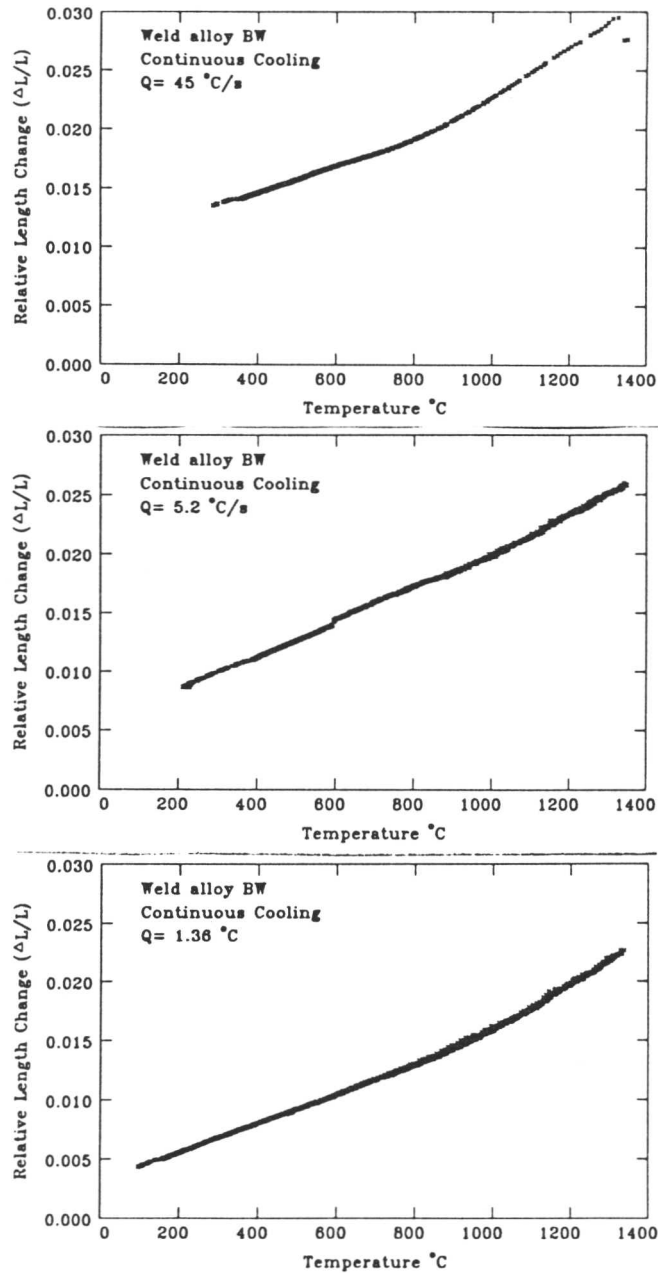


Fig. 8.8: Showing relative length versus temperature profiles for continuous cooling transformation of samples of alloy BW at different cooling rate Q , as obtained dilatometrically. ($T_{\delta} = 1340^{\circ}\text{C}$, ferritisation time = 5 min).

8.5 Interpretation of Continuous Cooling Dilatometry

Continuous cooling dilatometry was employed in an attempt to study the effect of cooling rate on the transformation behaviour of $\delta \rightarrow \gamma$ in wrought and weld alloys. The transformation start temperature was observed to decrease as the cooling rate increased. The analysis of the continuous cooling dilatometry data proved not to be easy. The complication arises from the non linear expansivities of the δ and γ phases as a function of temperature on the one hand, and from sample creep problems at the high ferritisation temperature involved on the other. However, an attempt was made, as shown in Fig 8.9, to calculate the volume fraction of austenite as a function of temperature by dividing the relative length versus temperature profiles obtained under continuous cooling conditions, into a series of isothermal steps. By subtracting the $(\delta + \gamma)$ curve from the single phase δ curve at each step, to obtain the overall relative length change due to the $\delta \rightarrow \gamma$ transformation at the step temperature, the volume fraction of austenite was calculated for the course of transformation during continuous cooling. The volume fraction of austenite was calculated from the overall relative change at each step by applying equation (6.1) derived earlier in chapter six.

The volume fraction of austenite versus temperature diagram for continuous cooling transformation in welded alloy W111 is shown in Fig. 8.10. The volume fractions of austenite calculated from the measured relative length changes, for the temperature range from 1300 to 800°C shows good agreement with the optically measured volume fractions (Table 8.2). This temperature range was considered as it is generally agreed (chapter 3) that the $\delta \rightarrow \gamma$ transformation occurs within this range during cooling. The graph also shows that the transformation start temperature decreases with increasing cooling rate, but the differences do not seem to be large probably because the formation of the allotropic austenite is very fast at the high temperatures.

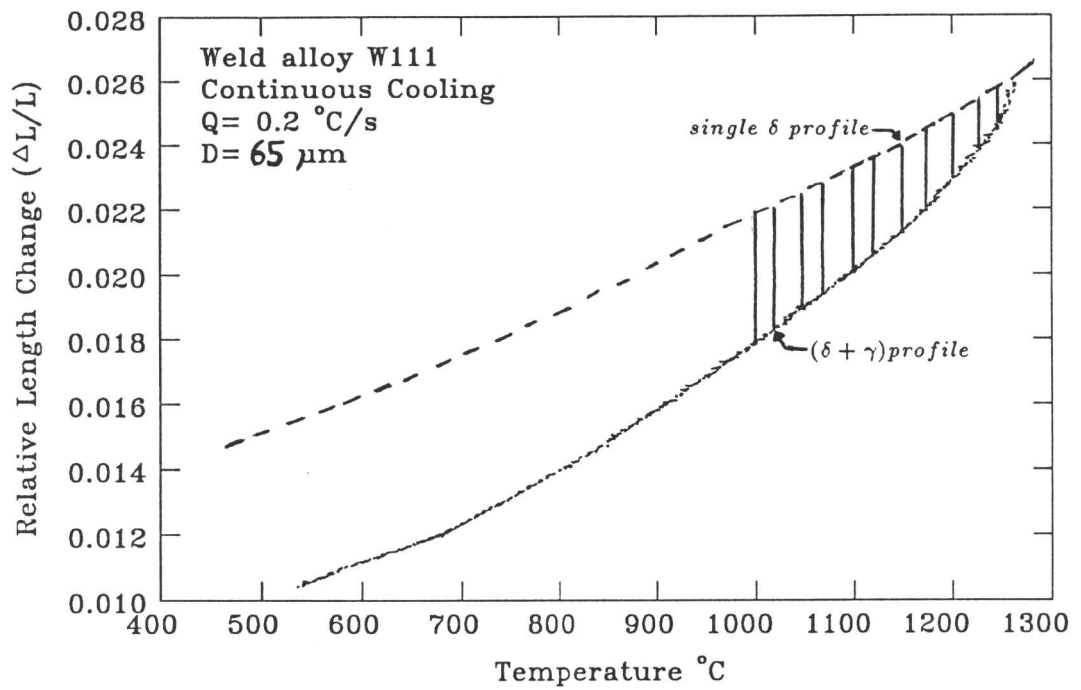


Fig. 8.9: Illustrating the method used to estimate the volume fraction of austenite from the measured relative length changes (dilatometric experiments) during continuous cooling transformation.

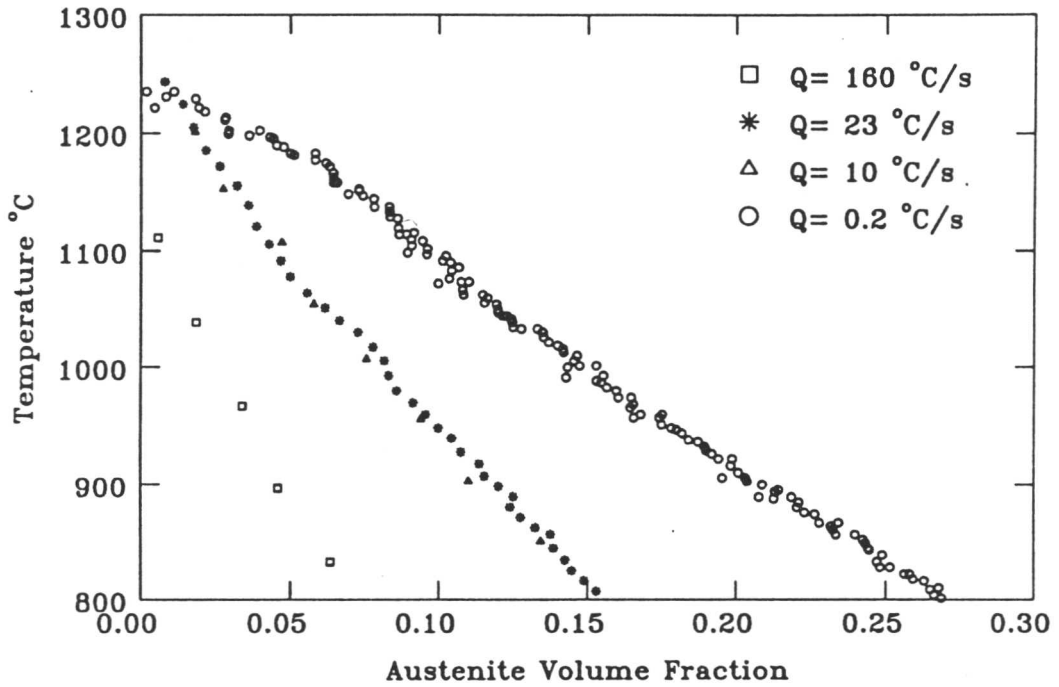


Fig. 8.10: Austenite volume fraction as a function of temperature for continuously cooled W111 samples, as a function of cooling rate. The austenite volume fractions were calculated from the measured relative length changes recorded during dilatometric experiments.

8.6 The Coupled Effects of the δ Grain Size and Cooling Rate

To study the effect of the δ -ferrite grain size on the $\delta \rightarrow \gamma$ reaction during continuous cooling experiments, at a variety of cooling rates, samples of alloys SH (wrought) and W111 (welded) were heated at $T_\delta = 1280^\circ\text{C}$ for 60 s, and 180 s, after which they were cooled to ambient temperature at different cooling rates. The volume fractions of austenite and the δ grain sizes were determined using image analysis on the "Seescan" equipment and from dilatometric measurements of the relative length changes. The details of the experimental data and the results are shown in Table 8.2 and Fig. 8.11.

Table 8.2: Experimental data and results of grain size and austenite volume fraction measurements for continuously cooled SH and W111 alloys:

Specimen	$T_\delta(^{\circ}\text{C})$	$t_{T_\delta}(\text{sec})$	$Q(^{\circ}\text{C s}^{-1})$	$D_\delta(\mu\text{m})$	V_γ^{SS}	V_γ^{DL}
W111-a	1280	60	10	65	0.12	0.12
W111-b	1280	60	23	68	0.14	0.13
W111-c	1280	60	0.2	65	0.24	0.24
W111-d	1280	60	160	59	0.11	0.09
SH-a	1280	60	0.2	350	0.23	0.21
SH-b	1280	60	2.36	340	0.15	0.12
SH-c	1280	60	156	356	0.04	0.05
W111-e	1280	180	0.2	104	0.24	—
W111-f	1280	180	2.6	109	0.16	0.15
W111-g	1280	180	120	98	0.1	.11
SH-d	1280	180	220	435	0.02	—
SH-e	1280	180	2.71	500	0.1	—
Sh-f	1280	180	0.216	450	0.2	—

SS = measured by Seescan image analysis method. DL = calculated from dilatometric measurements. — = not measured. The estimated error in the measured V_γ is ± 0.02 .

As expected the volume fraction of austenite was observed to decrease with increasing cooling rate. In the wrought alloy SH a combination of large δ grain size ($450\mu\text{m}$) and high cooling rate ($Q = 220^\circ\text{C s}^{-1}$) was sufficient to suppress the formation of the allotriomorphic and Widmanstätten austenite. Only very fine intragranular austenite particles were precipitated (Fig. 8.12 a). With a smaller δ grain size of $350\mu\text{m}$ and a cooling rate 165°C s^{-1} , thin more or less continuous layers of austenite allotriomorphs were observed to decorate the δ/δ grain boundaries (Fig 8.13 a). Widmanstätten austenite was not observed and the dominant morphology was intragranularly precipitated acicular austenite. For $Q = 2.6^\circ\text{C s}^{-1}$, the allotriomorphic austenite was observed to cover most of the δ grain boundaries. Side-plates of Widmanstätten austenite were also observed. The volume fraction of the Widmanstätten austenite was higher in the sample of smaller δ grain size when compared to the coarse grained sample, while for the acicular austenite the case was reversed (Figs. 8.12 b & 8.13 b). For $Q = 0.2^\circ\text{C s}^{-1}$, a higher volume fractions of austenite were observed for both grain sizes compared with the faster cooling rates. All three morphologies of austenite were observed, but the dominant morphology was found to be Widmanstätten austenite (Fig. 8.12 c and Fig. 8.13 c).

On the other hand, in the welded alloy W111, the δ grain size was not observed to have a large effect on the overall volume fraction of austenite measured after continuous cooling treatment and the volume fraction was less sensitive to the cooling rate when compared with the wrought alloy samples. Unlike the wrought alloy samples the allotriomorphic layers of austenite were observed to be continuous and thicker for all cooling rates and grain sizes studied. Very fine particles of acicular austenite were observed particularly with the high cooling rates. A set of transmission electron images (Fig. 8.14), reveal the formation of austenite on inclusions in the quenched sample of alloy W111. It is evident from Fig. 8.14, that all sizes of inclusion nucleate austenite, but the inclusions with smaller size seem to be more efficient. This could be a consequence of the inclusions chemistry. The allotriomorphic layers were observed to thicken with decreasing cooling rate, while the volume fraction of acicular austenite was found to decrease with the slower cooling rate (Figs. 8.15 & 8.16).

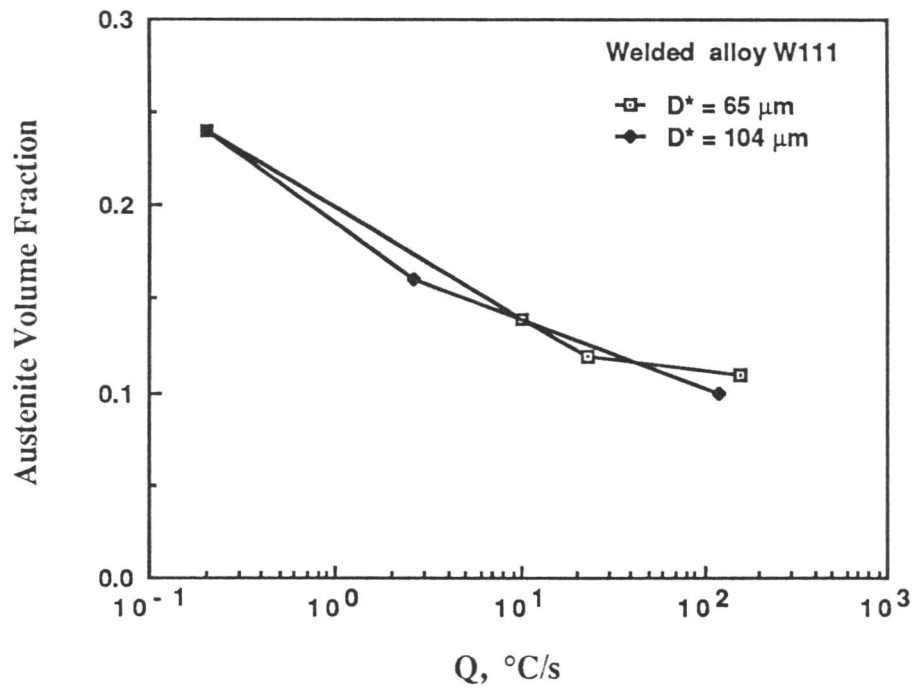
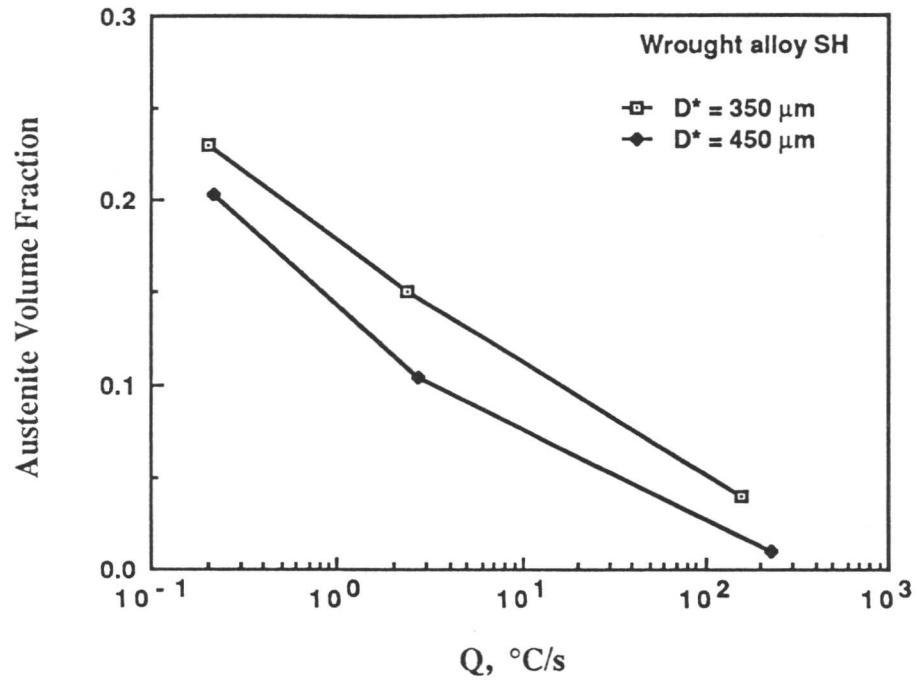


Fig. 8.11: The measured volume fraction of austenite as a function of cooling rate and δ -ferrite grain size.

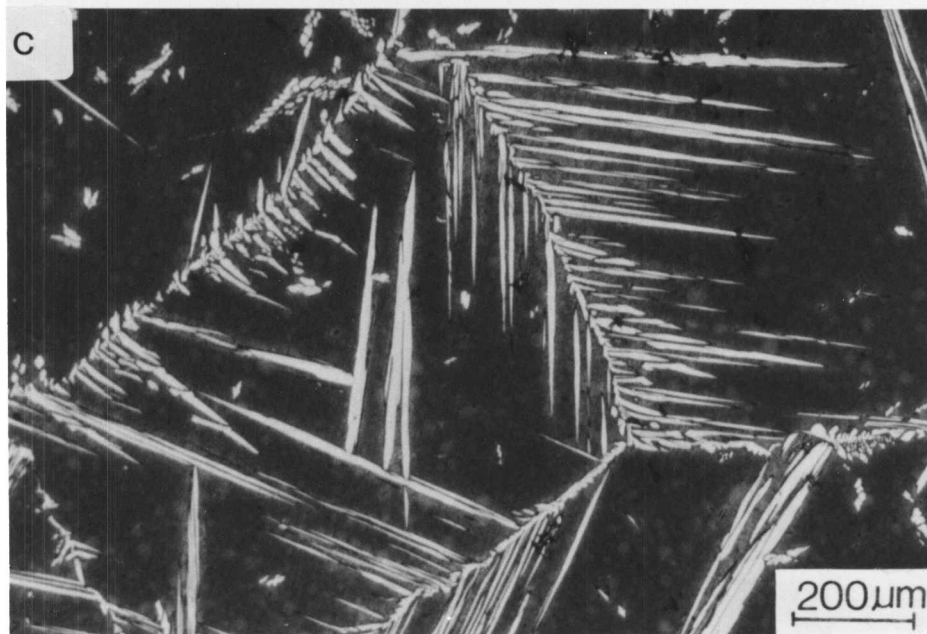
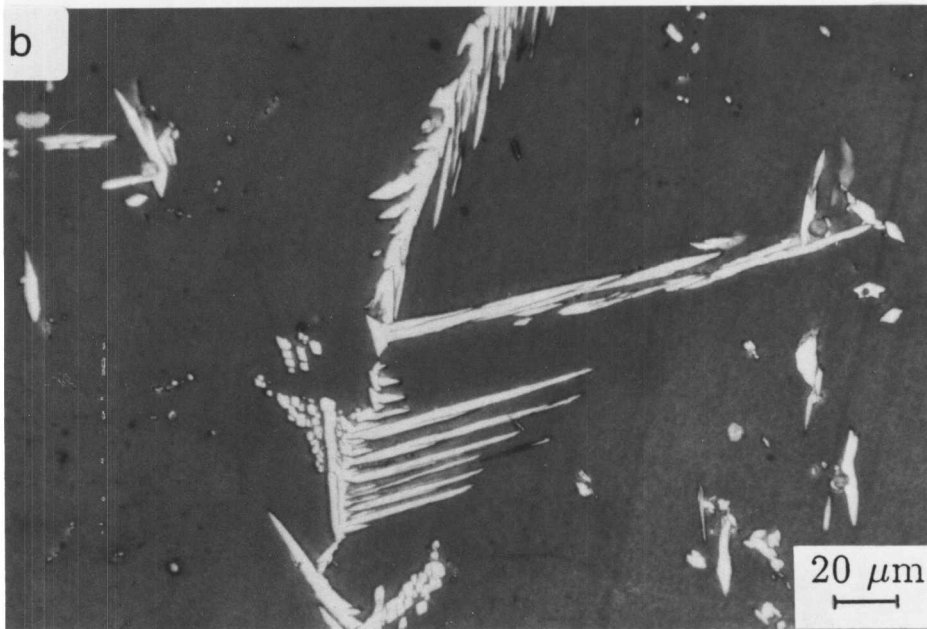
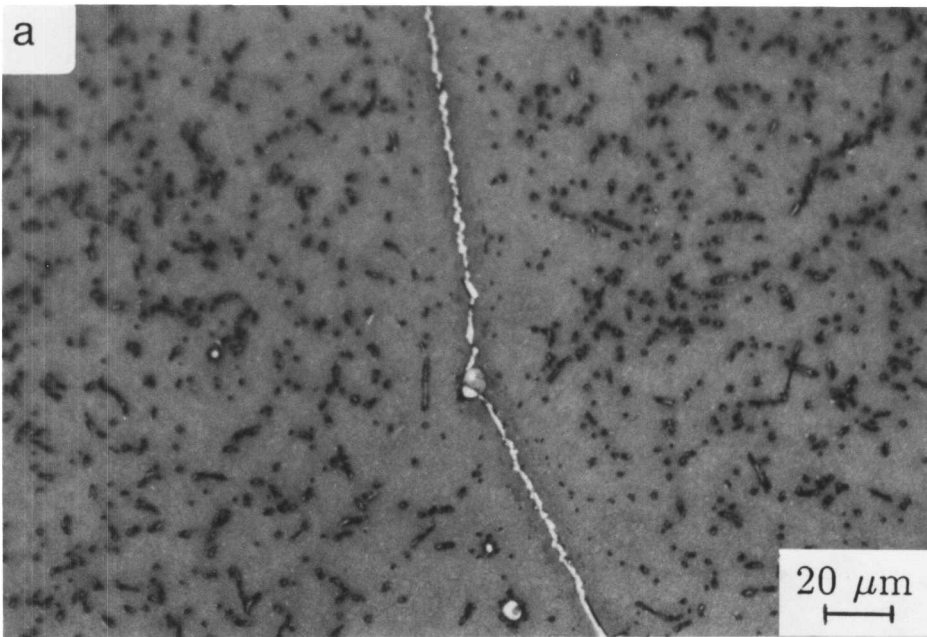


Fig. 8.12: A set of colour micrographs showing the microstructure of samples of alloy SH (average δ grain size of $450\mu\text{m}$), after continuous cooling treatment:

(a) $Q = 220^\circ\text{C s}^{-1}$

(b) $Q = 2.7^\circ\text{C s}^{-1}$

(d) $Q = 0.2^\circ\text{C s}^{-1}$

The etchant used is Beraha's colour etchant.

The light etching phase is austenite.

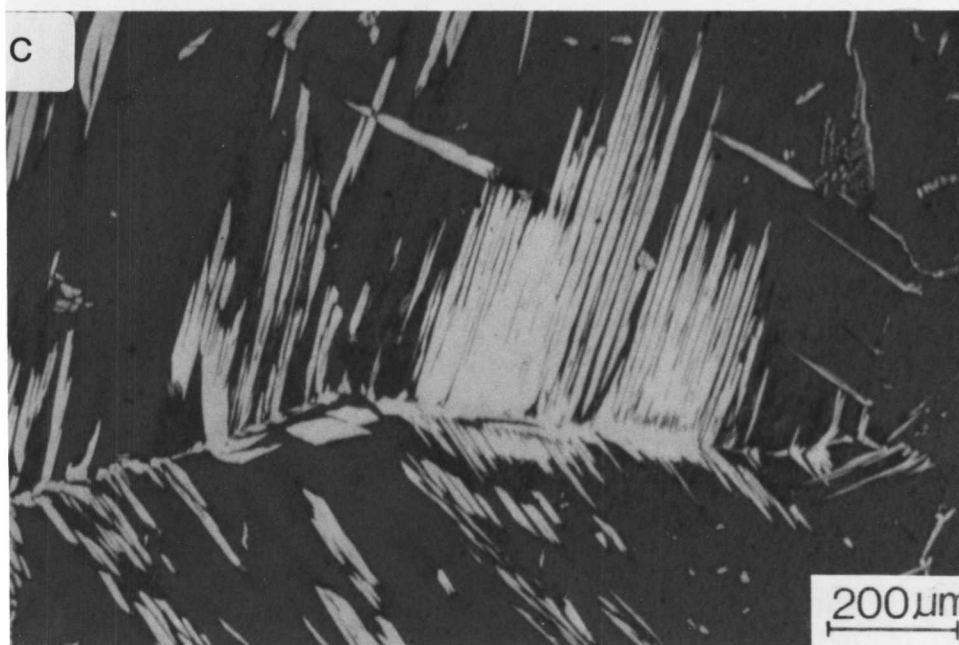
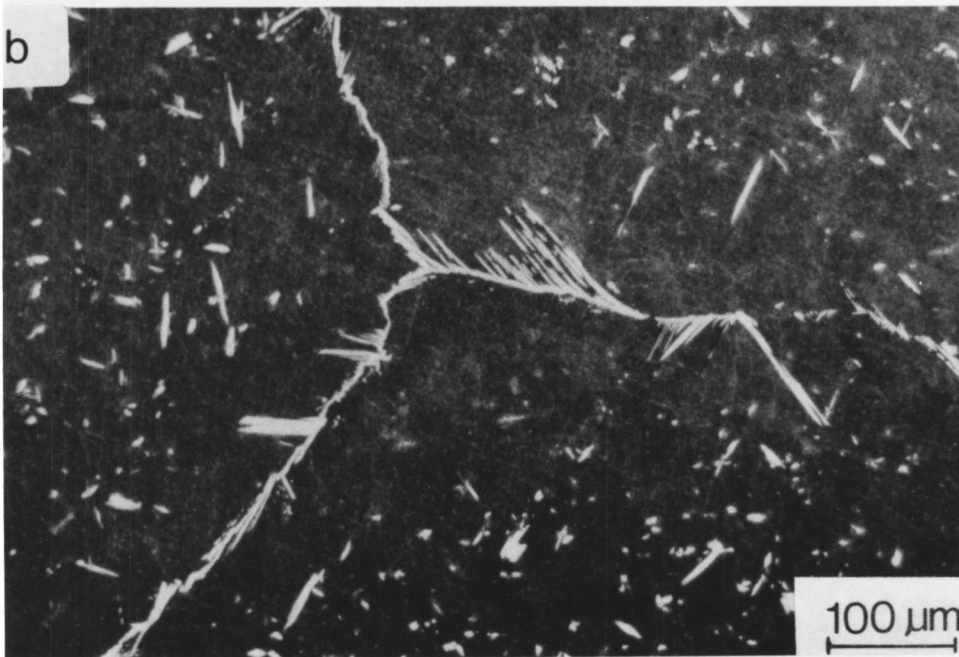
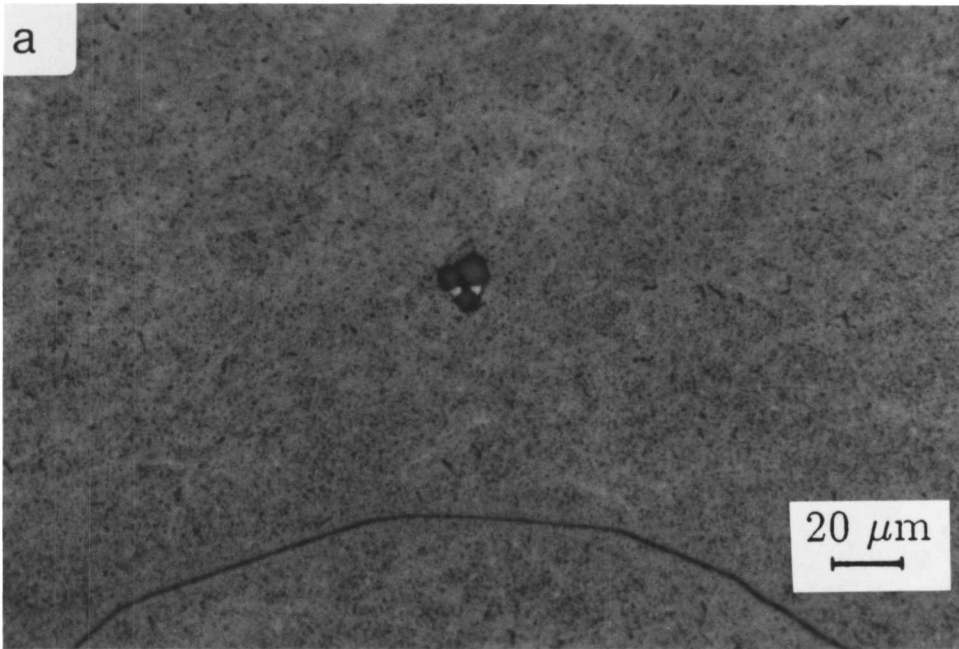


Fig. 8.13: A set of colour micrographs showing the microstructure of samples of alloy SH (average δ grain size of $350\mu\text{m}$), after continuous cooling treatment:

(a) $Q = 160^\circ\text{C s}^{-1}$

(b) $Q = 2.4^\circ\text{C s}^{-1}$

(d) $Q = 0.2^\circ\text{C s}^{-1}$

The etchant used is Beraha's colour etchant.

The light etching phase is austenite.

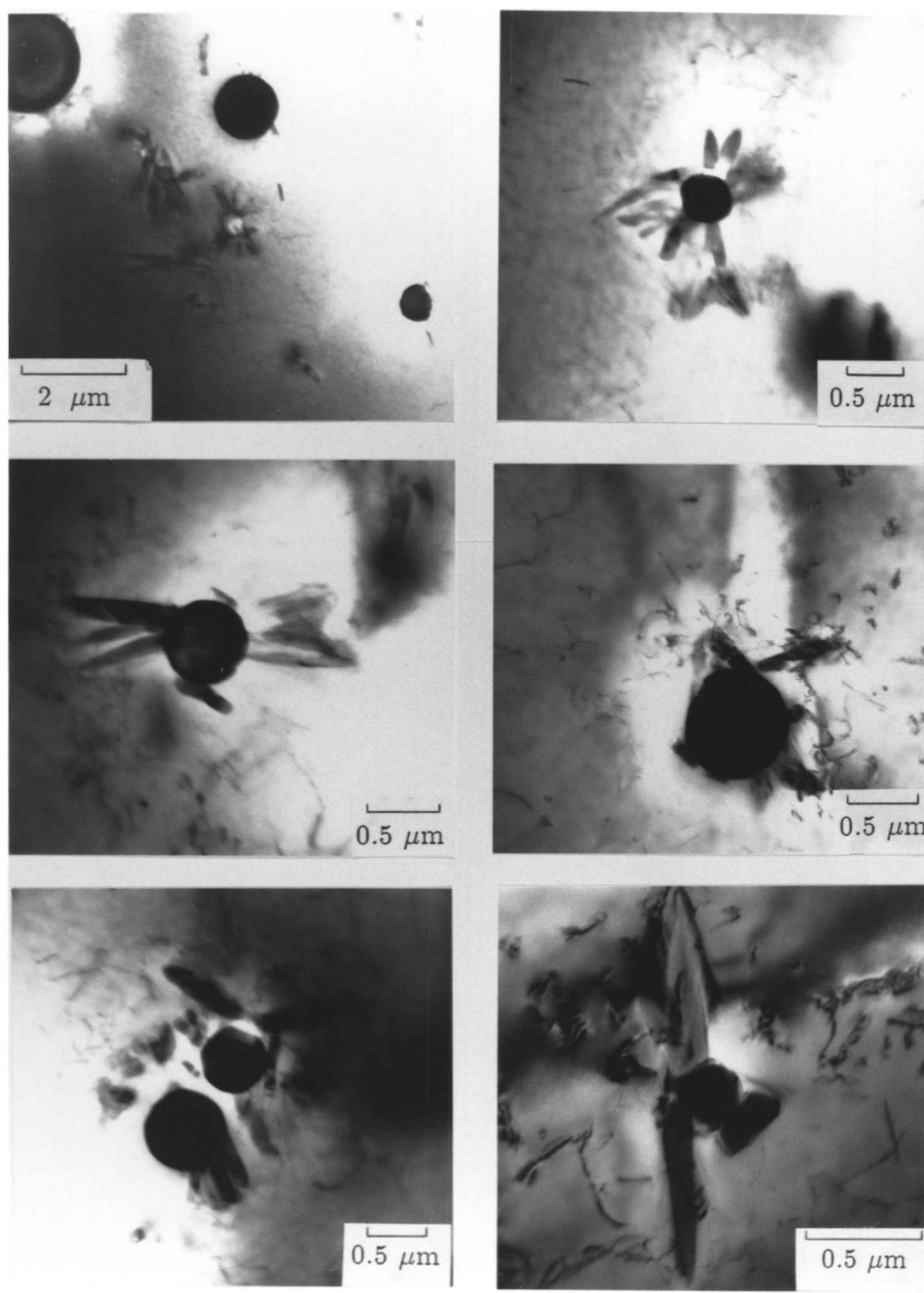


Fig. 8.14: TEM bright field images of austenite nucleated on inclusions.

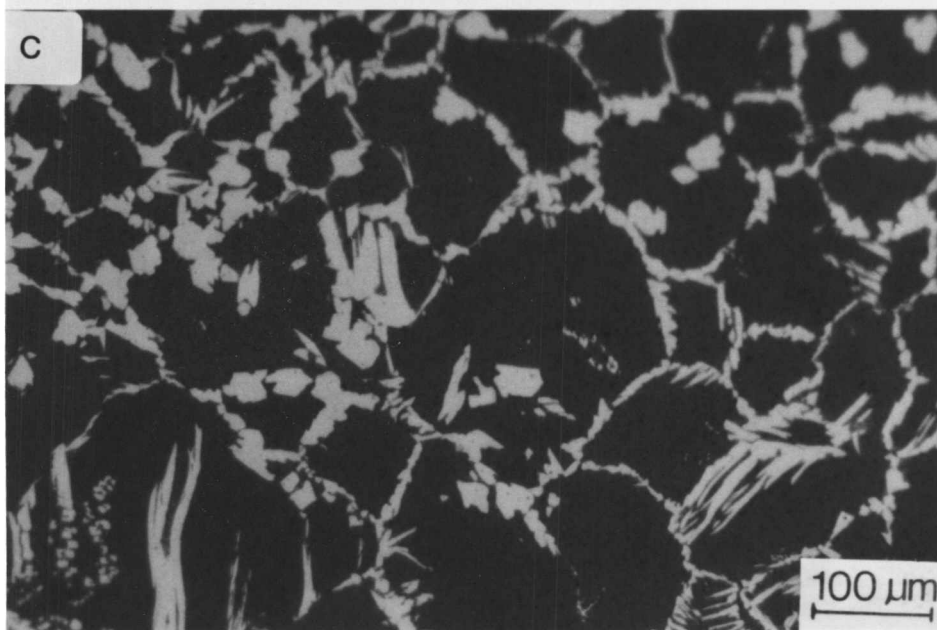
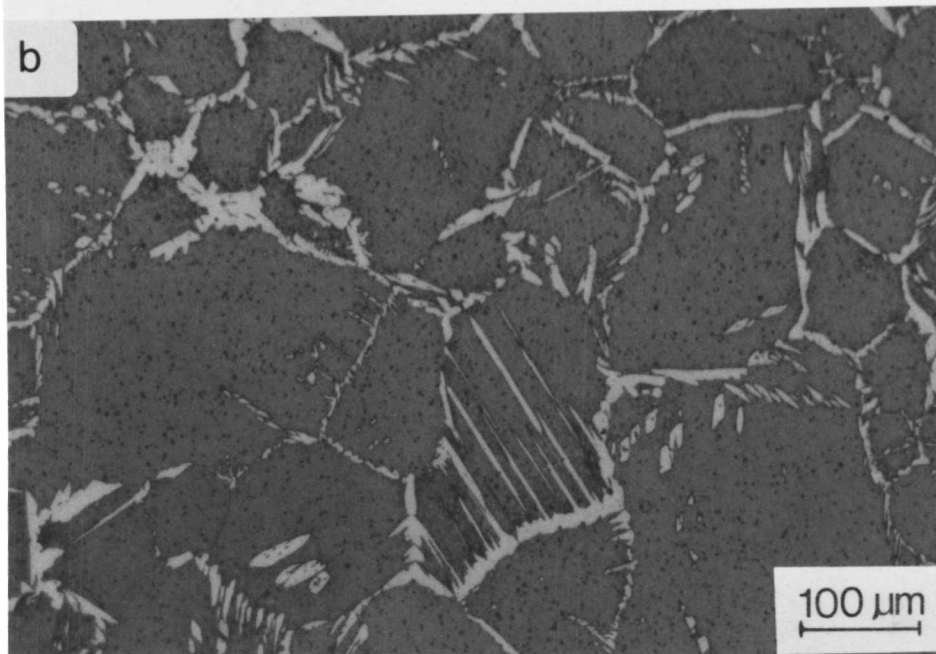
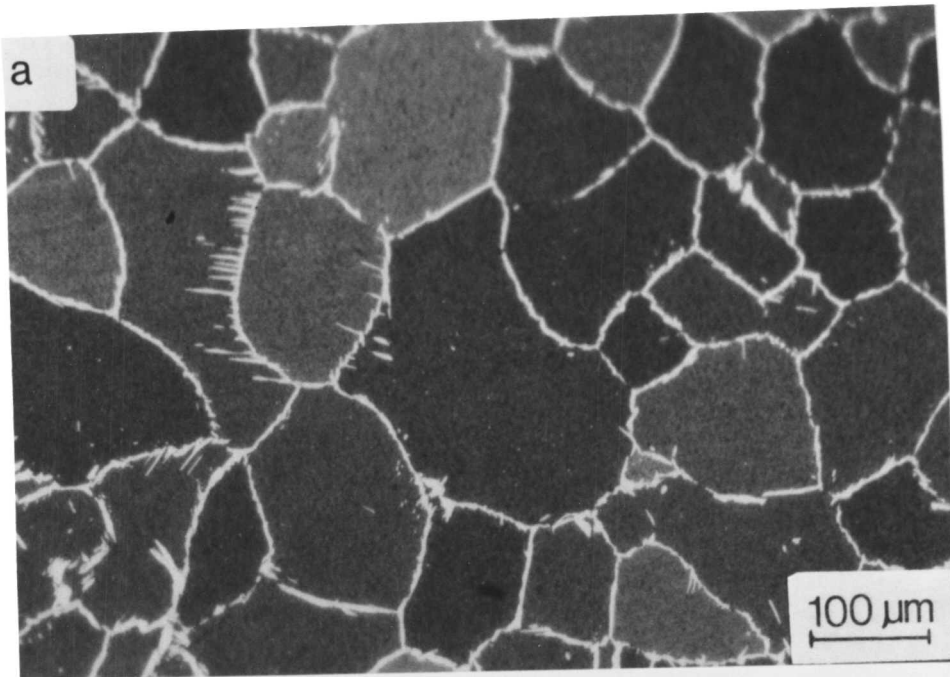


Fig. 8.15: A set of colour micrographs showing the microstructure of samples of alloy W111 (average δ grain size of $104\mu\text{m}$), after continuous cooling treatment:

(a) $Q = 120^\circ\text{C s}^{-1}$

(b) $Q = 2.6^\circ\text{C s}^{-1}$

(d) $Q = 0.2^\circ\text{C s}^{-1}$

The etchant used is Berraha's colour etchant.

The light etching phase is austenite.

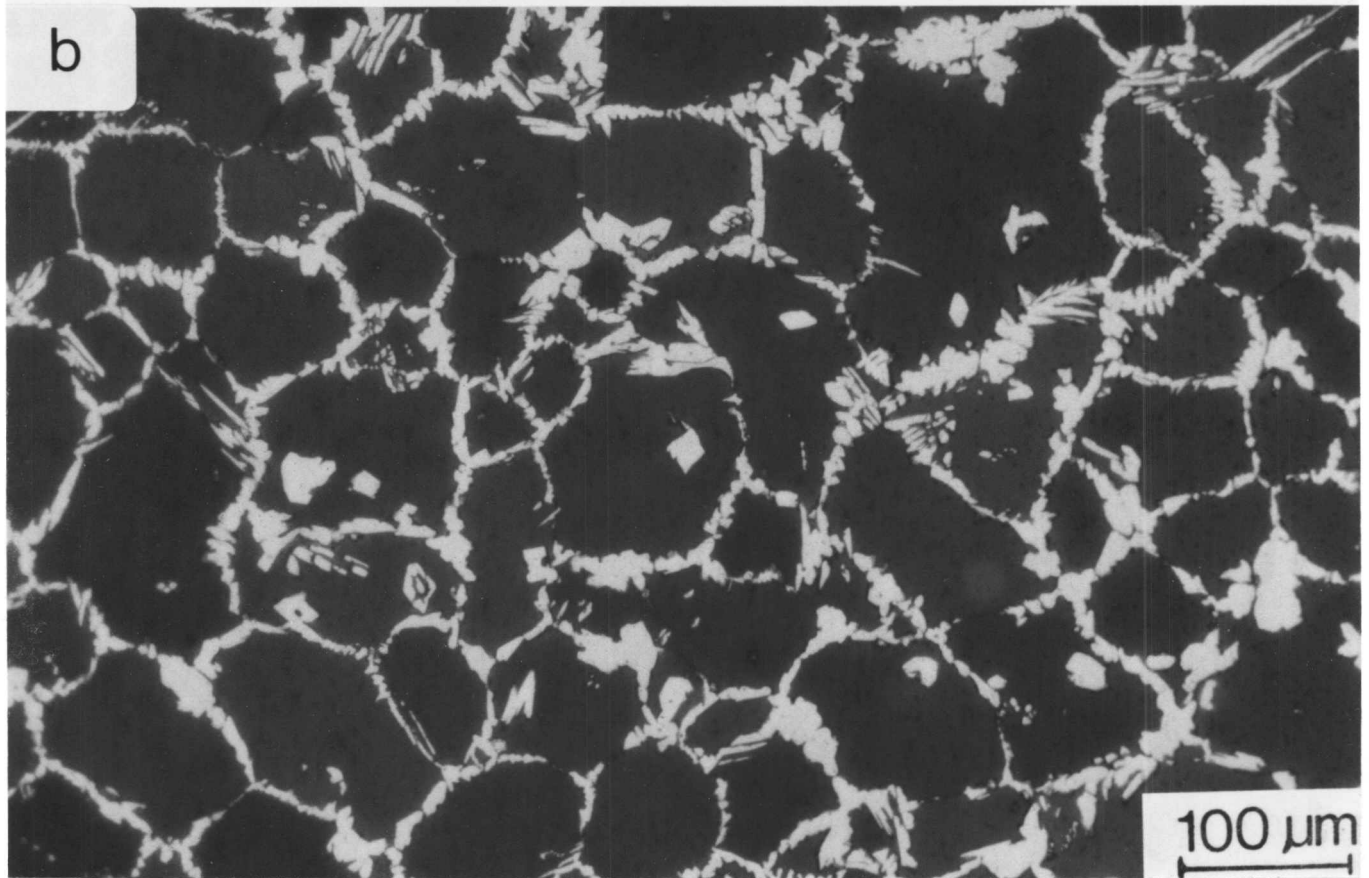
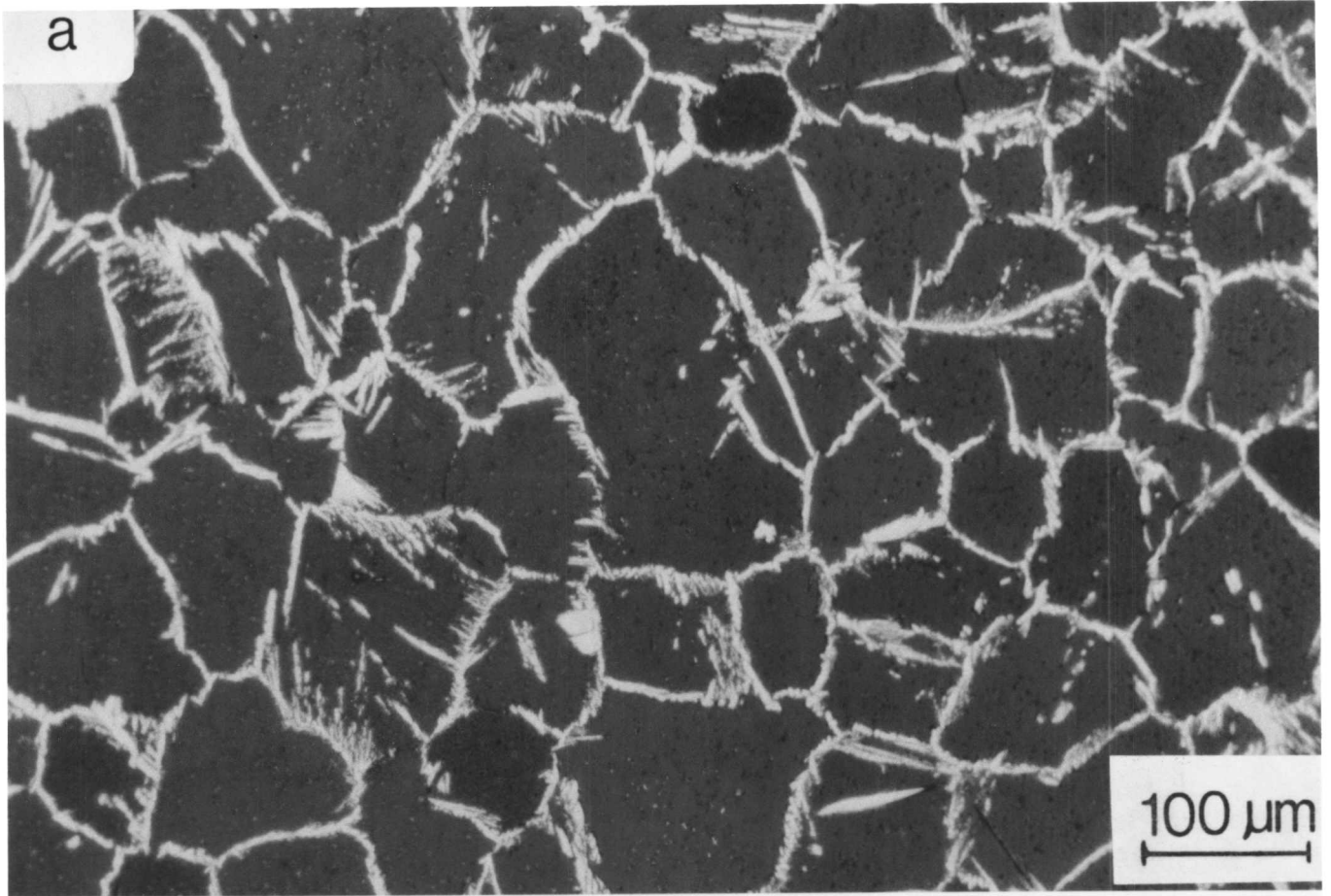


Fig. 8.16: Optical micrographs showing the microstructure of samples of alloy W111 (average δ grain size of $65\ \mu\text{m}$), after continuous cooling treatment: (a) $Q = 160^{\circ}\text{C s}^{-1}$, (b) $Q = 23^{\circ}\text{C s}^{-1}$. The etchant used is Beraha's colour etchant, and the light etching phase is austenite.

In summary, the fine δ grain sizes (65 and $104\mu\text{m}$) in samples of welded alloy W111, provided a larger density of boundary nucleation sites, which led to the formation of continuous layers and higher volume fractions of allotriomorphic austenite. Higher oxygen contents in the welded alloy increased the availability of intragranular sites of inclusions to form the acicular austenite particularly for high cooling rate. For slower cooling rates, a greater degree of thickening of the austenite allotriomorphs was found to occur consistent with the larger time available for transformation.

The smaller grain size of the welded samples is believed to be, as mentioned in chapter 6, a consequence of the pinning effect of inclusions and the effect of higher nitrogen and carbon contents in delaying the ferritisation process during heating.

The experiments in the wrought alloy SH samples, are in effect simulations of the heat affected zone conditions in real welded joints. The lack of extensive pinning effects and because of higher temperatures involved, particularly in the grain growth region, a coarse δ grain structure was obtained leading to a drastic effect on the amount of austenite that grows during cooling to the ambient temperature.

It can be concluded that due to the small surface area of δ boundaries per unit volume of sample, these sites tend to be saturated at the early stages of the $\delta \rightarrow \gamma$ solid state transformation, and because of the lack of intragranular sites, the $\delta \rightarrow \gamma$ may be completely suppressed. The conditions necessary for this are typical of electron beam welds (Fig. 8.17). The effect of inclusions would be profound in such cases, in providing extra nucleation sites for nucleating austenite. This suggests that oxide dispersions in duplex stainless steels may be useful in solving the problem of austenite depletion in the heat affected zone regions of the welded samples.

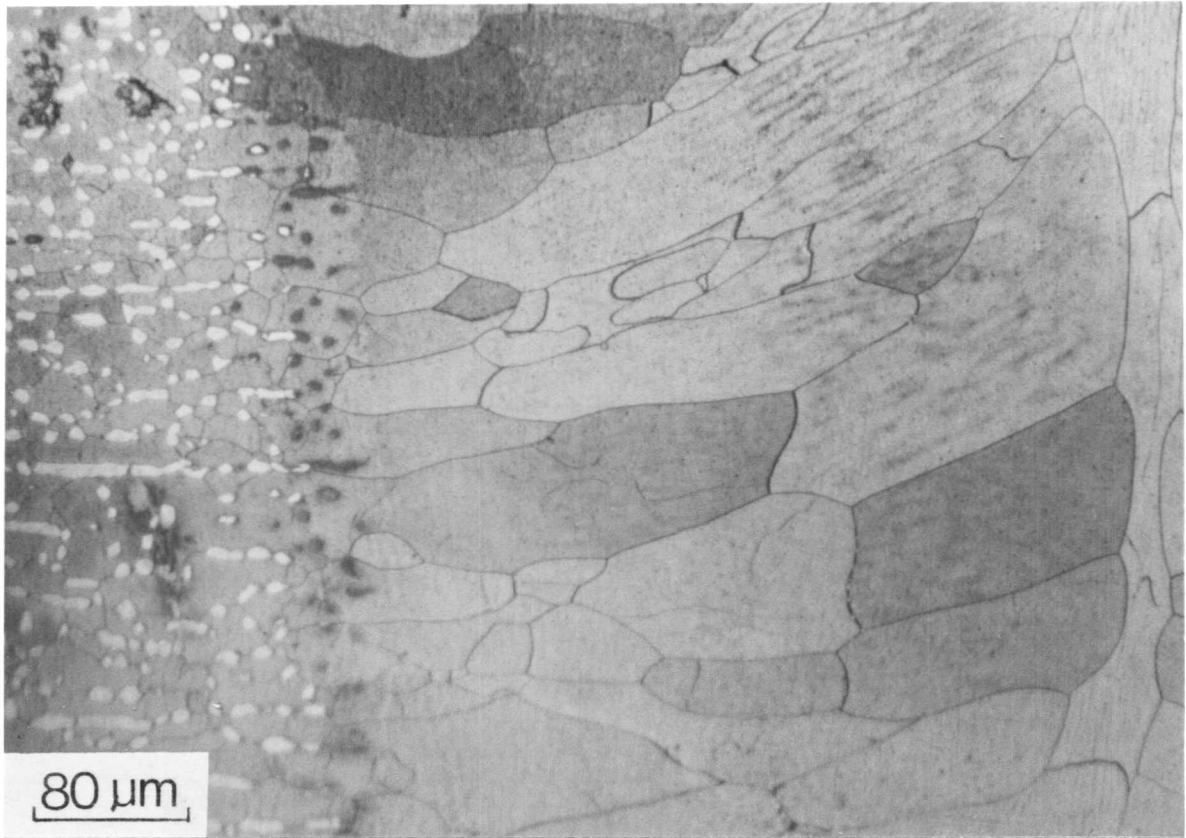


Fig. 8.17: Microstructure of electron beam weld metal demonstrating the effect of high undercoolings in suppressing the $\delta \rightarrow \gamma$ transformation.

8.7 Conclusions

- (a) The dilatometric approach is found to be useful in establishing the data necessary to clarify continuous cooling transformation. The high ferritisation temperatures involved do cause some difficulties but they are surmountable. The correlation between the dilatometric measurements of austenite volume fraction obtained after continuous cooling treatments, with the optical determinations is found to be satisfactory.
- (b) Both optical and dilatometric results suggest a decrease in the $\delta \rightarrow \gamma$ transformation start temperature with increasing cooling rate. This suppression of the transformation to lower temperatures is consistent with the nature of a "C" curve on a time-temperature-transformation diagram.
- (c) Consistent with the above observation the austenite volume fraction after continuous cooling treatment decreases with increasing cooling rate. A cooling rate higher than about $200^{\circ}\text{C s}^{-1}$ is found to suppress the austenite formation completely, whereas a very slow cooling rate of $0.11^{\circ}\text{C s}^{-1}$ leads to the precipitation of sigma phase, for the alloys studied in the present work.
- (d) The coupled effect of δ grain size and cooling rate on suppressing the $\delta \rightarrow \gamma$ solid state transformation is more profound in wrought alloys compared with welded alloys. The grain growth of δ -ferrite is much faster in the wrought alloy samples due to lack of grain boundary pinning by inclusions, and due to the lack of the effect of higher interstitial concentrations in retarding the ferritisation process. On the other hand, the high inclusion content in welded alloys restricts the coarsening of the δ -ferrite grains, and also provides an increased density for the heterogeneous nucleation of austenite. During cooling, the exhaustion of the limited grain boundary nucleation sites in coarse grained wrought alloys associated with high degrees of undercoolings, promotes the intragranular nucleation of austenite, demonstrating the importance of the inclusions in mitigating the depletion in the heat affected zones in weld metals.

Chapter 9

CONCLUSIONS AND FURTHER RESEARCH

9.1 Introduction

The aim of the work presented in this thesis was to investigate the development of microstructures of wrought and welded duplex stainless steel, and to provide data necessary for the prediction of microstructure. The estimation of microstructure is as yet empirical and costly. A model for prediction based on phase transformation theory should yield better results and reduce the cost of alloy design in the long run. Quantification and characterisation of the $\delta \rightarrow \gamma$ transformation in wrought and welded alloys was approached using dilatometry. This technique was verified experimentally and the results were interpreted theoretically. The technique has its problems because of the high temperatures involved, but these difficulties were found not to be insurmountable. This chapter will summarise the essential results and include suggestions for further research.

9.2 Conclusions

- (a) The dilatometric technique is found to be powerful in the sense that it enables the quantitative estimation of the volume fraction of austenite during isothermal or anisothermal heat treatment and hence enables the kinetics of the $\delta \rightarrow \gamma$ transformation to be characterised in great detail.
- (b) The $\delta \rightarrow \gamma$ transformation kinetics are found to be rapid when compared with the typical cooling conditions encountered in welding. The reaction was found in some cases to reach completion in a matter of few seconds. The overall transformation kinetics follow a classical "C" curve behaviour in the high temperature range, consistent with a nucleation and growth phenomenon. The reaction in some cases appears to occur in two separate stages related to the presence of two distinctive morphologies of intragranularly nucleated austenite.
- (c) A comparative study of the overall transformation kinetics of weld metals and wrought metals demonstrated that because of the presence of a relatively high oxygen concentration in the former alloys they were insensitive to the parent

δ -ferrite grain size. This was found to be due to the effect of nonmetallic inclusions in providing effective heterogeneous sites for the formation of austenite so that the δ boundaries play a diminished role in the over all austenite nucleation rate for welded alloys. The inclusions also serve to restrict the δ grain growth. By contrast, the wrought steels with lower oxygen content were found to be much more sensitive to the δ grain size, which in turn was found to coarsen rapidly during ferritisation heat treatment.

- (d) An experimental investigation of the development of the microstructure in duplex stainless weld metal revealed the importance of the ferritic solidification mode. Since some δ -ferrite is always retained to ambient temperature in duplex stainless steels, the columnar grains of δ -ferrite are able to extend over many layers of multi-run weld. Metallography also showed the importance of nonmetallic inclusions (the volume fraction of which is related to the oxygen concentration) in providing heterogeneous nucleation sites in the weld deposits. Microanalytical results revealed negligible differences in the substitutional solute contents of the austenite and the δ -ferrite, indicating that in the weld metals, the nonequilibrium development of microstructure is the rule rather than an exception.
- (e) The cooling rate seems essential in determining the overall volume fraction of austenite under continuous cooling conditions. However, the wrought alloys, with their lower inclusion populations are necessarily found to be more sensitive to cooling rate effects.
- (f) The $\delta \rightarrow \gamma$ transformation is in all cases found to be a nucleation and growth process. The morphologies of austenite developed as a consequence of the decomposition of δ -ferrite in all alloys resemble those of ferrite formed from the austenite in low-alloy steels. Although such morphological similarities exist, the mechanisms do not seem to be alike. Acicular and Widmanstätten ferrite are known to form by a displacive mechanism in low-alloy steels, but their austenite counterparts in duplex stainless steel show compositional differences with respect to substitutional solutes when compared with δ -ferrite. Tentative surface relief data associated with their formation, were not proved to be consistent with an invariant-plane strain. All these results suggest a reconstructive mechanism of transformation. The fact that austenite rods were observed to cross the δ grain boundaries is also consistent with a reconstructive growth mechanism.

- (g) During ageing heat treatments, a coarse δ grain size was observed to have the effect of promoting the formation of fine intragranular nucleated acicular austenite at the expense of other morphologies.
- (h) In wrought steels with low interstitials content, the Widmanstätten morphology was found to predominate in the microstructure for cooling rates between 40 to $0.1^{\circ}\text{C s}^{-1}$.
- (i) The precipitation of σ phase in duplex stainless steel weld metals can be rapid, in some alloys precipitating within 15 minutes at 900°C . Its preferred nucleation sites were found to be the δ/γ boundaries, possibly due to the existence of chromium/molybdenum rich regions in the vicinity, created by partitioning during the $\delta \rightarrow \gamma$ reaction.
- (j) Thermodynamic calculations on the basis of two phase equilibrium (δ and γ) were compared with some experimental observations, and the measurements revealed good agreement at temperatures where the equilibrium microstructure consisted of just δ and γ . In the three phase region $\delta + \gamma + \sigma$, good correlation was also observed fortuitously, when the composition of σ was close to that expected for the δ -ferrite. The thermodynamic calculations also confirm the austenitising effect of the interstitials and nickel, and the role of these elements in extending the ($\delta + \gamma$) phase field to higher temperatures.

9.3 Further Research

The project has so far verified the dilatometric technique as a powerful approach to characterize and quantify the $\delta \rightarrow \gamma$ transformation in duplex stainless steels, and provided data which are important for the prediction of microstructure. Further investigation is needed to incorporate the effect of precipitation reactions in any model for microstructural development. It is also necessary to relate quantitatively, the microstructure to the mechanical and corrosion properties. This project suggests that the development of oxide dispersed (wrought) duplex stainless steels may help in solving the problem of grain coarsening and lack of austenite in the heat affected zones. This approach needs to be verified experimentally as it may prove to be detrimental to mechanical and corrosion properties.

APPENDIX 1: CALCULATION OF AUSTENITE VOLUME FRCITION FROM THE
MEASURED RELATIVE LENGTH CHANGE

```
1 FTVSCLR PROGRAM=%H% DATA=.DUPLEX:DATA1
2 C Copyright N.I.A. Haddad, H.K.D.H. Bhadeshia 1987
3 C Program for calculating the volume fraction of austenite from  $\delta$ -ferrite
4 C (NOTE: take care in specifying correctly the magnitude of length change)
5 C 0.0057 100.0
6 C 0.0053 120.0
7 C A1, G1 are the  $\delta$ -ferrite, and austenite lattice parameters
8 C Transformation assumed to be composition invariant
9 C T = Centigrade (all temps in this unit) L - RELATIVE LENGTH CHANGE
10 C TYPICAL DATA SET.
11 C RELATIVE LENGTH CHANGE, CENTIGRADE
12 C DILATOMETRIC ANALYSIS PROGRAM 26 May 1987
13 C THE LATTICE PARAMETER OF THE AUSTENITE IS TAKEN FROM
    LEDBETTER AND AUSTIN WORK
14     IMPLICIT REAL*8(A-H,K-Z),INTEGER(I,J)
15     WRITE(6,5)
16 23  READ(6,*,END=22) L,T
17     CALL DELTA(T,A1)
18     CALL GAMMA(T,G1)
19 C
20     VOL = 6.0D+00*L*A1**3/(G1**3-2.0D+00*A1**3)
21     WRITE(6,2)A1,G1,VOL,L,T
22     GOTO 23
23 22  STOP
24 2   FORMAT(3F10.4,F10.5,F10.0)
25 5   FORMAT(' PROGRAM',//.' DLP  GLP',
26     &' VOLUME  LENGTH TEMPERATURE')
27     END
28
29     SUBROUTINE DELTA(CTEMP,DT)
```

```

30     DOUBLE PRECISION DT,CTEMP,T
31     T = CTEMP-20.0D+00
32 C   (REMOVES AMBIENT TEMPERATURE)
33     DT = 2.8797D+00 + (0.8839D-05*T + 0.5D+00*60.9698D-10
34     &*T*T - (1.0D+00/3.0D+00)*327.52308D-15*T*T*T)*2.8797D+00
35 C 2.8797 ANGSTROMS IS THE LATTICE PARAMETER AT AMBIENT TEM-
    PERATURE
36     RETURN
37     END
38
39     SUBROUTINE GAMMA (CTEMP,GT)
40     DOUBLE PRECISION GT,T,CTEMP
41     T=CTEMP-20.0D+00
42     GT = 3.590*(1.0D+00 + 1.507829D-05*T + 0.5D+00*1.04.45473D-10
43     &*T*T - (1.0D+00/3.0D+00)*420.515D-14*T*T*T)
44 C 3.587 ANGSTROMS IS THE LATTICE PARAMETER AT AMBIENT TEM-
    PERATURE
45     RETURN
46     END
47 %

```

APPENDIX 2

Table A.1: The calculated partition coefficient “K”, defined as C_γ/C_δ where C_γ is the concentration (wt.%) of the element in austenite and C_δ is the concentration (wt.%) of the element in δ -ferrite, as varied with temperature.

Wrought alloy SH

$K = \frac{C_\gamma}{C_\delta}$	Temperature K						
	873	973	1073	1173	1273	1373	1473
K(C)	0.88	0.27	0.80	1.4	2.01	2.56	3.09
K(N)	8.88	1.21	3.16	4.22	4.71	4.98	5.42
K(Fe)	0.93	1.19	1.1	1.06	1.04	1.03	1.01
K(Cr)	0.87	0.52	0.65	0.72	0.77	0.82	0.89
K(Ni)	3.68	3.15	2.6	2.24	1.96	1.74	1.53
K(Mo)	1.13	0.71	0.8	0.85	0.88	0.89	0.85
K(Mn)	2.00	1.1	1.07	1.02	0.97	0.91	0.81
K(Si)	0.17	3.17	1.17	0.84	0.69	0.6	0.49
K(Cu)	2.31	0.63	0.81	0.87	0.9	0.9	0.86

Table A.2: The calculated partition coefficient “K”, defined as C_γ/C_δ where C_γ is the concentration (wt.%) of the element in austenite and C_δ is the concentration (wt.%) of the element in δ -ferrite, as varied with temperature.

Wrought alloy SHP

$K = \frac{C_\gamma}{C_\delta}$	Temperature K						
	873	973	1073	1173	1273	1373	1473
K(C)	0.37	0.49	0.76	1.18	1.7	2.23	2.73
K(N)	3.74	4.29	4.22	4.31	4.34	4.29	4.2
K(Fe)	0.97	1.06	1.08	1.07	1.06	1.04	1.04
K(Cr)	0.72	0.67	0.67	0.7	0.73	0.76	0.8
K(Ni)	3.84	3.23	2.76	2.35	2.02	1.82	1.65
K(Mo)	1.12	0.88	0.88	0.89	0.92	0.94	0.96
K(Mn)	0.21	1.36	1.17	1.03	1.00	0.97	0.94
K(Si)	0.32	0.95	1.09	0.98	0.77	0.75	0.74

Table A.3: The calculated partition coefficient “K”, defined as C_γ/C_δ where C_γ is the concentration (wt.%) of the element in austenite and C_δ is the concentration (wt.%) of the element in δ -ferrite, as varied with temperature.

Welded alloy WR2

$K = \frac{C_\gamma}{C_\delta}$	Temperature K					
	873	973	1073	1173	1273	1373
K(C)	0.3	1.2	0.56	1.32	2.07	2.66
K(N)	2.18	7.09	1.38	3.05	3.87	4.07
K(Fe)	1.06	0.99	1.22	1.09	1.04	1.02
K(Cr)	0.64	0.82	0.56	0.7	0.77	0.81
K(Ni)	4.13	3.36	3.19	2.42	2.09	1.85
K(Mo)	0.84	0.91	0.75	0.82	0.87	0.89
K(Mn)	1.44	1.32	0.91	0.93	0.92	0.9
K(Si)	0.86	0.37	2.38	0.84	0.63	0.56
K(Cu)	1.09	1.29	0.58	0.79	0.89	0.92

Table A.4: Equilibrium compositions of δ -ferrite and austenite as calculated using the “Thermocalc” system (wt.%).

Wrought alloy SH

Element	Phase	Temperature K						
		873	973	1073	1173	1273	1373	1473
C	δ	0.0309	0.0489	0.0331	0.0259	0.0232	0.0243	0.0296
C	γ	0.0272	0.0132	0.0265	0.0362	0.0465	0.0623	0.0915
N	δ	0.0215	0.0568	0.0313	0.0276	0.0303	0.0394	0.0613
N	γ	0.191	0.0686	0.099	0.1164	0.1426	0.1963	0.3319
Fe	δ	68.07	60.66	63.87	65.14	65.99	66.56	66.82
Fe	γ	63.00	72.33	70.18	69.37	68.86	68.32	67.32
Cr	δ	26.31	34.22	30.45	28.69	27.32	26.2	25.52
Cr	γ	23.00	17.72	19.88	20.69	21.08	21.52	22.77
Ni	δ	2.90	2.25	2.75	3.21	3.75	4.32	4.78
Ni	γ	10.66	7.08	7.13	7.19	7.35	7.50	7.32
Mo	δ	1.36	1.66	1.54	1.49	1.45	1.41	1.40
Mo	γ	1.53	1.17	1.24	1.27	1.27	1.26	1.19
Mn	δ	0.67	0.79	0.80	0.82	0.84	0.84	0.83
Mn	γ	1.34	0.87	0.86	0.84	0.81	0.76	0.68
Si	δ	0.58	0.21	0.43	0.49	0.51	0.49	0.46
Si	γ	0.1	0.7	0.5	0.41	0.35	0.3	0.22
Cu	δ	0.07	0.11	0.1	0.1	0.09	0.09	0.09
Cu	γ	0.16	0.07	0.08	0.08	0.08	0.08	0.08

Table A.5: Equilibrium compositions of δ -ferrite and austenite as calculated using the “Thermocalc” system (wt.%)

Wrought alloy SHP

Element	Phase	Temperature K						
		873	973	1073	1173	1273	1373	1473
C	δ	0.011	0.0121	0.011	0.0094	0.0085	0.0091	0.01
C	γ	0.0041	0.0059	0.0084	0.0111	0.0145	0.0204	0.0273
N	δ	0.0114	0.0076	0.007	0.0074	0.0088	0.0128	0.016
N	γ	0.0427	0.0324	0.0297	0.0317	0.0381	0.0547	0.0672
Fe	δ	67.7	66.05	65.32	65.7	66.43	67.15	67.37
Fe	γ	65.48	69.95	70.5	70.42	70.25	70.00	70.00
Cr	δ	26.71	28.88	29.47	28.73	27.48	26.12	25.69
Cr	γ	19.32	19.31	19.77	20.00	19.97	19.83	20.54
Ni	δ	3.28	2.64	2.74	3.13	3.69	4.37	4.64
Ni	γ	12.59	8.53	7.54	7.38	7.56	7.90	7.68
Mo	δ	2.27	2.40	2.43	2.40	2.36	2.32	2.31
Mo	γ	2.55	2.15	2.13	2.14	2.16	2.18	2.21
Mn	δ	0.009	0.009	0.009	0.01	0.01	0.01	0.01
Mn	γ	0.018	0.012	0.011	0.01	0.01	0.01	0.01
Si	δ	0.011	0.01	0.01	0.01	0.01	0.01	0.01
Si	γ	0.004	0.01	0.011	0.01	0.009	0.008	0.007

Table A.6: Equilibrium compositions of δ -ferrite and austenite as calculated using the “Thermocalc” system (wt.%).

Welded alloy WR2

Element	Phase	Temperature K					
		873	973	1073	1173	1273	1373
C	δ	0.0426	0.0171	0.0334	0.0156	0.0106	0.0091
C	γ	0.0127	0.0205	0.0186	0.0206	0.022	0.0242
N	δ	0.0783	0.024	0.1099	0.0527	0.0441	0.0461
N	γ	0.1704	0.1704	0.152	0.1607	0.1704	0.1876
Fe	δ	61.43	65.14	53.78	59.87	62.2	63.33
Fe	γ	65.35	64.26	65.51	64.99	64.86	64.81
Cr	δ	31.18	26.94	37.82	31.00	28.09	26.33
Cr	γ	20.05	22.00	21.18	21.66	21.61	21.37
Ni	δ	2.32	2.6	2.62	3.47	4.12	4.84
Ni	γ	9.57	8.74	8.34	8.38	8.6	8.95
Mo	δ	3.28	3.12	3.7	3.41	3.23	3.11
Mo	γ	2.74	2.83	2.78	2.8	2.8	2.78
Mn	δ	1.14	1.2	1.65	1.62	1.62	1.64
Mn	γ	1.64	1.58	1.51	1.51	1.5	1.47
Si	δ	0.48	0.92	0.19	0.5	0.62	0.63
Si	γ	0.41	0.34	0.46	0.42	0.39	0.35
Cu	δ	0.056	0.048	0.096	0.073	0.066	0.064
Cu	γ	0.061	0.062	0.056	0.058	0.059	0.059

Table A.7: Equilibrium compositions of δ -ferrite and austenite as calculated using the “Thermocalc” system (wt.%).

Wrought alloy R2P

Element	Phase	Temperature K						
		873	973	1073	1173	1273	1373	1473
C	δ	0.0237	0.0447	0.0271	0.0177	0.0136	0.0124	0.0135
C	γ	0.0156	0.0108	0.0171	0.0212	0.0257	0.0293	0.0382
Fe	δ	66.41	54.41	58.23	60.52	61.94	62.92	63.57
Fe	γ	60.91	67.43	66.27	65.66	65.34	65.12	64.85
Cr	δ	26.14	37.43	33.15	30.32	28.26	26.51	24.93
Cr	γ	20.11	18.19	19.34	19.83	19.86	19.59	19.15
Ni	δ	2.81	2.32	3.04	3.71	4.44	5.29	6.29
Ni	γ	13.14	9.42	9.36	9.45	9.73	10.2	10.88
Mo	δ	3.19	4.39	4.00	3.77	3.62	3.52	3.47
Mo	γ	3.87	3.17	3.29	3.36	3.41	3.47	3.57
Mn	δ	0.87	1.29	1.29	1.3	1.32	1.33	1.34
Mn	γ	1.86	1.33	1.33	1.33	1.32	1.3	1.28
Si	δ	0.56	0.11	0.26	0.36	0.40	0.41	0.39
Si	γ	0.1	0.44	0.39	0.35	0.31	0.29	0.25

Table A.8: Equilibrium compositions of δ -ferrite and austenite as calculated using the “Thermocalc” system (wt.%).

Wrought alloy R2PP

Element	Phase	Temperature K						
		873	973	1073	1173	1273	1373	1473
C	δ	0.0107	0.0142	0.0097	0.0062	0.0043	0.0035	0.0032
C	γ	0.0026	0.0038	0.0052	0.006	0.0065	0.0071	0.0083
N	δ	0.0091	0.0107	0.008	0.0063	0.0055	0.0054	0.006
N	γ	0.0184	0.0155	0.0159	0.0162	0.017	0.0184	0.0214
Fe	δ	64.66	58.13	58.39	59.64	60.99	62.23	63.27
Fe	γ	64.16	66.00	65.6	65.36	65.28	65.29	65.26
Cr	δ	29.45	36.05	35.3	33.45	31.42	29.38	27.37
Cr	γ	19.48	20.41	21.25	21.6	21.55	21.2	20.61
Ni	δ	3.2	2.7	3.22	3.91	4.67	5.54	6.55
Ni	γ	13.36	10.79	10.32	10.2	10.31	10.64	11.2
Mo	δ	2.65	3.08	3.05	2.97	2.89	2.83	2.78
Mo	γ	2.96	2.77	2.79	2.8	2.81	2.83	2.88
Mn	δ	0.007	0.009	0.009	0.01	0.01	0.01	0.01
Mn	γ	0.012	0.01	0.01	0.01	0.01	0.01	0.01
Si	δ	0.015	0.006	0.007	0.01	0.01	0.012	0.012
Si	γ	0.007	0.011	0.011	0.01	0.01	0.009	0.008

Table A.9: Equilibrium compositions of δ -ferrite and austenite as calculated using the “Thermocalc” system (wt.%).

Welded alloy WR4

Element	Phase	Temperature K						
		873	973	1073	1173	1273	1373	1473
C	δ	0.0413	0.0127	0.036	0.0172	0.0116	0.0098	0.0098
C	γ	0.0104	0.0221	0.0175	0.0206	0.0225	0.025	0.0292
N	δ	0.0636	0.0107	0.0786	0.0362	0.0286	0.0286	0.0325
N	γ	0.0854	0.098	0.0786	0.0872	0.0934	0.1029	0.1202
Fe	δ	61.23	67.23	52.91	59.03	61.36	62.46	63.11
Fe	γ	64.43	62.35	65.11	64.32	64.04	63.9	63.72
Cr	δ	31.59	25.21	38.99	32.02	28.99	27.14	25.64
Cr	γ	19.25	22.5	20.56	21.29	21.36	21.14	20.81
Ni	δ	2.56	2.78	2.92	3.89	4.63	5.46	6.4
Ni	γ	11.61	10.51	9.73	9.78	10.02	10.41	10.95
Mo	δ	3.16	2.77	3.66	3.33	3.16	3.06	3.00
Mo	γ	2.9	3.04	2.87	2.91	2.93	2.94	2.96
Mn	δ	0.81	0.76	1.19	1.14	1.15	1.16	1.17
Mn	γ	1.25	1.21	1.1	1.1	1.1	1.09	1.06
Si	δ	0.55	1.22	0.2	0.52	0.65	0.67	0.63
Si	γ	0.45	0.27	0.53	0.47	0.43	0.39	0.35
Cu	δ	0.009	0.006	0.015	0.012	0.011	0.01	0.01
Cu	γ	0.011	0.011	0.009	0.01	0.01	0.01	0.01

Table A.10: Equilibrium compositions of δ -ferrite and austenite as calculated using the “Thermocalc” system (wt.%).

Wrought alloy R4P

Element	Phase	Temperature K						
		873	973	1073	1173	1273	1373	1473
C	δ	0.0194	0.0444	0.0256	0.0168	0.0133	0.0124	0.0142
C	γ	0.0209	0.0104	0.0175	0.0218	0.0255	0.0367	0.0409
Fe	δ	69.04	56.46	60.72	62.79	63.99	64.81	65.35
Fe	γ	60.40	69.18	67.81	67.17	66.87	66.66	66.39
Cr	δ	24.1	36.11	31.4	28.81	26.98	25.41	23.96
Cr	γ	20.85	17.55	18.86	19.38	19.4	19.12	18.68
Ni	δ	2.84	2.42	3.09	3.68	4.36	5.17	6.15
Ni	γ	13.48	8.94	8.94	9.05	9.33	9.81	10.49
Mo	δ	2.62	3.8	3.41	3.21	3.09	3.02	2.98
Mo	γ	3.57	2.67	2.81	2.88	2.93	2.98	3.07
Mn	δ	0.65	1.00	0.98	1.00	1.02	1.03	1.04
Mn	γ	1.60	1.04	1.05	1.05	1.04	1.03	1.00
Si	δ	0.73	0.16	0.38	0.51	0.55	0.54	0.51
Si	γ	0.08	0.59	0.51	0.5	0.41	0.37	0.33

Table A.11: Equilibrium compositions of δ -ferrite and austenite as calculated using the “Thermocalc” system (wt.%).

Wrought alloy IC373

Element	Phase	Temperature K						
		873	973	1073	1173	1273	1373	1473
C	δ	0.0234	0.029	0.0183	0.0136	0.0116	0.0115	0.0137
C	γ	0.005	0.0079	0.0123	0.0166	0.0207	0.0264	0.0375
N	δ	0.1101	0.1244	0.0893	0.0819	0.0876	0.1035	0.1349
N	γ	0.1935	0.16	0.1954	0.2211	0.2491	0.2916	0.3681
Fe	δ	58.73	48.78	56.67	59.13	60.46	61.37	61.97
Fe	γ	66.09	68.84	66.43	65.34	64.78	64.35	63.9
Cr	δ	32.03	40.32	33.22	30.61	28.91	27.49	22.22
Cr	γ	18.55	18.57	20.00	20.68	20.86	20.79	20.61
Ni	δ	1.8	1.43	2.23	2.78	3.38	4.07	4.87
Ni	γ	9.06	6.97	7.42	7.67	7.98	8.43	9.9
Mo	δ	4.27	5.28	4.41	4.1	3.92	3.79	3.7
Mo	γ	2.97	2.87	3.1	3.22	3.28	3.33	3.37
Mn	δ	0.59	0.72	0.68	0.68	0.69	0.68	0.67
Mn	γ	0.76	0.64	0.66	0.66	0.65	0.63	0.6
Si	δ	0.41	0.06	0.35	0.50	0.55	0.54	0.51
Si	γ	0.61	0.72	0.62	0.5	0.42	0.36	0.31
Cu	δ	1.96	3.19	2.26	2.03	1.93	1.87	1.84
Cu	γ	1.67	1.14	1.48	1.61	1.67	1.7	1.71
Co	δ	0.07	0.06	0.07	0.07	0.07	0.08	0.08
Co	γ	0.09	0.091	0.09	0.091	0.091	0.091	0.09

Table A.12: Equilibrium compositions of δ -ferrite and austenite as calculated using the “Thermocalc” system (wt.%).

Wrought alloy IC378

Element	Phase	Temperature K						
		873	973	1073	1173	1273	1373	1473
C	δ	0.0223	0.0313	0.0263	0.019	0.0151	0.0139	0.0154
C	γ	0.0304	0.0238	0.0259	0.0282	0.031	0.036	0.0461
N	δ	0.025	0.0368	0.0439	0.0458	0.0509	0.0617	0.082
N	γ	0.2804	0.184	0.1685	0.171	0.1825	0.2063	0.2524
Fe	δ	70.27	65.05	63.3	63.97	65.00	65.98	66.79
Fe	γ	63.87	68.31	68.52	68.43	68.45	68.5	68.45
Cr	δ	22.66	27.37	28.74	27.73	26.31	24.83	23.4
Cr	γ	20.76	19.5	19.83	19.93	19.72	19.31	18.79
Ni	δ	2.26	2.01	2.19	2.56	3.04	3.64	4.38
Ni	γ	9.39	6.94	6.44	6.43	6.63	7.02	7.61
Mo	δ	2.93	3.56	3.67	3.53	3.38	3.26	2.12
Mo	γ	3.15	2.81	2.85	2.87	2.87	2.86	2.86
Mn	δ	0.88	1.13	1.28	1.34	1.39	1.41	1.41
Mn	γ	1.98	1.48	1.41	1.39	1.38	1.36	1.32
Si	δ	0.65	0.48	0.41	0.44	0.47	0.47	0.45
Si	γ	0.08	0.35	0.39	0.37	0.35	0.32	0.29
Cu	δ	0.1	0.17	0.2	0.2	0.19	0.19	0.18
Cu	γ	0.28	0.18	0.18	0.18	0.18	0.18	0.18
Co	δ	0.2	0.16	0.15	0.16	0.16	0.17	0.18
Co	γ	0.18	0.2	0.2	0.2	0.2	0.21	0.21

Table A.13: Equilibrium compositions of δ -ferrite and austenite as calculated using the “Thermocalc” system (wt.%).

Wrought alloy IC381

Element	Phase	Temperature K						
		873	973	1073	1173	1273	1373	1473
C	δ	0.0206	0.0352	0.0262	0.0183	0.0145	0.0134	0.0148
C	γ	0.0292	0.0214	0.0247	0.0272	0.0301	0.035	0.0448
N	δ	0.0252	0.0518	0.0529	0.0518	0.0558	0.066	0.0857
N	γ	0.2551	0.1739	0.1672	0.1719	0.1841	0.2075	0.2514
Fe	δ	69.41	62.23	61.58	62.69	63.85	64.86	65.66
Fe	γ	63.12	67.63	67.53	67.38	67.37	67.38	67.3
Cr	δ	23.16	29.52	29.78	28.29	26.69	25.16	23.71
Cr	γ	21.08	19.47	19.93	20.05	19.86	19.47	18.97
Ni	δ	2.17	1.99	1.16	2.68	3.20	3.84	4.62
Ni	γ	9.314	7.15	6.80	6.83	7.07	7.49	8.1
Mo	δ	3.04	3.88	3.88	3.7	3.52	3.37	3.25
Mo	γ	3.29	2.92	2.97	3.00	3.00	3.00	3.01
Mn	δ	1.19	1.67	1.82	1.89	1.94	1.97	1.97
Mn	γ	2.63	2.01	1.95	1.93	1.91	1.88	1.83
Si	δ	0.87	0.48	0.47	0.54	0.58	0.58	0.55
Si	γ	0.11	0.48	0.48	0.46	0.43	0.39	0.35
Cu	δ	0.038	0.075	0.08	0.077	0.074	0.072	0.071
Cu	γ	0.101	0.068	0.067	0.068	0.068	0.068	0.069
Co	δ	0.08	0.065	0.064	0.065	0.068	0.072	0.076
Co	γ	0.08	0.085	0.085	0.085	0.086	0.087	0.088

Table A.14: Equilibrium compositions of δ -ferrite and austenite as calculated using the “Thermocalc” system (wt.%).

Wrought alloy MELT3

Element	Phase	Temperature K						
		873	973	1073	1173	1273	1373	1473
C	δ	0.0051	0.0054	0.0051	0.0044	0.004	0.0045	0.005
C	γ	0.0031	0.0041	0.0049	0.006	0.0074	0.0105	0.0137
N	δ	0.0031	0.0014	0.0013	0.0014	0.0018	0.003	0.004
N	γ	0.0189	0.0104	0.0079	0.0079	0.0094	0.0144	0.0177
Fe	δ	71.85	71.01	69.88	69.92	70.57	71.36	71.6
Fe	γ	67.68	73.08	74.07	74.16	74.18	74.15	74.24
Cr	δ	23.46	25.17	26.39	26.1	25.02	23.62	23.15
Cr	γ	18.18	18.07	18.5	18.65	18.47	18.06	18.11
Ni	δ	3.54	2.63	2.5	2.76	3.22	3.84	4.08
Ni	γ	12.78	7.74	6.35	6.09	6.25	6.67	6.51
Mo	δ	1.15	1.19	1.22	1.22	1.19	1.17	1.16
Mo	γ	1.34	1.09	1.07	1.08	1.08	1.09	1.11

Table A.15: Equilibrium compositions of δ -ferrite and austenite as calculated using the “Thermocalc” system (wt.%).

Wrought alloy MELT4

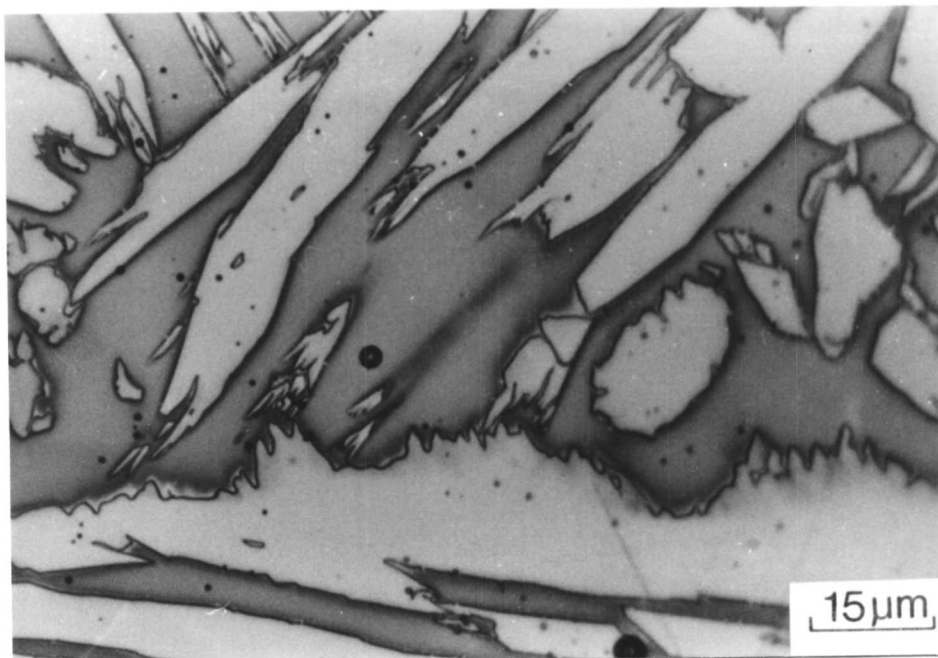
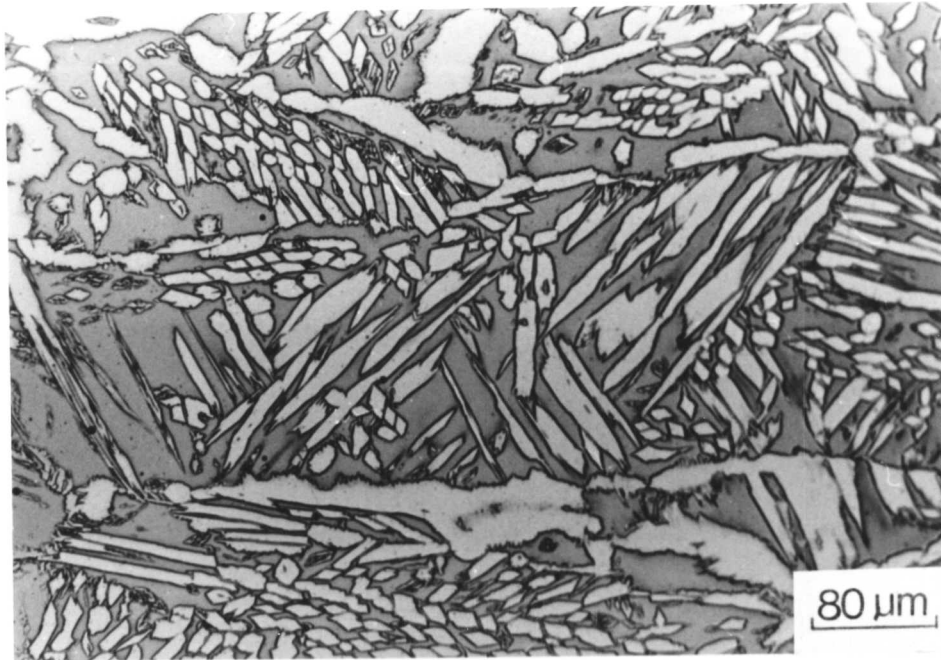
Element	Phase	Temperature K						
		873	973	1073	1173	1273	1373	1473
C	δ	0.0055	0.008	0.0062	0.0044	0.0033	0.0027	0.0024
C	γ	0.0067	0.006	0.006	0.006	0.006	0.006	0.0065
N	δ	0.0009	0.0007	0.0009	0.001	0.001	0.0011	0.0013
N	γ	0.0105	0.0053	0.0052	0.0052	0.0052	0.0052	0.0057
Fe	δ	76.85	71.7	70.58	70.75	71.21	71.25	72.07
Fe	γ	70.68	74.05	73.95	73.95	73.95	73.95	73.95
Cr	δ	19.72	25.57	26.28	25.63	24.9	24.24	22.77
Cr	γ	16.62	18.16	18.34	18.34	18.34	18.34	18.34
Ni	δ	3.7	2.73	3.13	3.62	4.08	4.51	5.15
Ni	γ	12.68	7.82	7.7	7.7	7.7	7.7	7.7

Table A.16: Equilibrium compositions of δ -ferrite and austenite as calculated using the “Thermocalc” system (wt.%).

Wrought alloy MELT5

Element	Phase	Temperature K						
		873	973	1073	1173	1273	1373	1473
C	δ	0.0095	0.0086	0.0083	0.0067	0.0055	0.0051	0.006
C	γ	0.0129	0.0112	0.0105	0.0106	0.0113	0.013	0.0174
N	δ	0.0023	0.001	0.0011	0.0013	0.0016	0.0021	0.0033
N	γ	0.0325	0.0123	0.0086	0.0081	0.0085	0.01	0.0137
Fe	δ	75.73	74.63	72.2	71.66	72.2	73.14	74.08
Fe	γ	68.98	74.73	75.33	75.26	75.38	75.62	75.8
Cr	δ	18.64	20.53	22.97	23.33	22.51	21.18	19.66
Cr	γ	16.56	16.37	17.11	17.37	17.14	16.59	15.85
Ni	δ	3.27	2.29	2.08	2.28	2.64	3.14	3.81
Ni	γ	11.83	6.64	5.26	5.04	5.15	5.49	6.05
Mo	δ	3.34	2.54	2.74	2.73	2.64	2.54	2.44
Mo	γ	2.58	2.24	2.29	2.31	2.31	2.28	2.27

APPENDIX 3



The microstructure of air cooled partially ferritised sample of alloy BW illustrating the tendency to form Widmanstätten austenite.